A Computational Study of Spherical Diffusion Flames in Microgravity with Gas Radiation

by

Songtao Tang

A dissertation submitted in partial fulfillment
of the requirements for the degree of
Doctor of Philosophy
(Mechanical Engineering)
in The University of Michigan
2008

Doctoral Committee:

Associate Professor Hong G. Im, Co-Chair
Professor Arvind Atreya, Co-Chair
Professor James F. Driscoll
Professor Margaret S. Wooldridge

Dedication

To my wife Lin Zhang and our son Joseph Tang

Acknowledgements

I would like to thank my co-advisors, Professor Hong Im and Professor Arvind Atreya, for their guidance and support throughout my doctoral work. They have provided both insightful directions and emotional support, and their trust on me has been very crucial for my achievement. My thanks are also due to Professors James Driscoll and Margaret Wooldridge, for their valuable advice and participation in my dissertation committee.

I am very grateful to Melissa Chernovsky for her unique experimental data and constructive suggestions during our discussions. I also greatly appreciate Ramanan Sankaran, Chunsang Yoo, and Jingjing Li who have offered me great help especially when I started my research. Other students in my research group have always been readily helpful, and their support has made my research life so enjoyable and fruitful, and I also owe special thanks to Gaurav Bansal whose insights have always been very helpful in our discussions.

This research was supported by NASA under the contract number of NNC04AA10A, and the Department of Mechanical Engineering at the University of Michigan also provided financial support for my Ph.D. study, both of which are greatly acknowledged.

Table of Contents

List of Figures

List of Tables

Glossary

Symbols	Quantities	Units
A	*Area*	cm^2
A	Dimensional band absorption	cm^{-1}
A^*	Dimensionless band absorption	–
C_p	Specific heat at constant pressure	kJ/kg/K
D	Diffusion coefficient	m^2/s
G	Incident radiation	W/cm^2
I	Radiation intensity	W/cm^2
l	Column length	cm
L_m	Mean beam length	cm
$\dot{m}$	Mass flow rate	kg/s
N	Number of ordinate	–
p	Hydrodynamic pressure	atm
p_0	Thermodynamic pressure	atm
P	Pressure	atm
P_e	Equivalent pressure	atm
q	Radiation heat flux	W/cm^2
$\mathbf{q}$	Radiation heat flux vector	W/cm^2
Q	Volumetric heat transfer rate	W/cm^3
r	Radius	cm
s	Path length	cm
$\hat{\mathbf{s}}$	Unit direction vector	–
t	Time	sec

T	Temperature	K
u	Velocity	cm/s
v	Ordinary diffusion velocity	cm/s
V	Diffusion velocity	cm/s
V_c	Correction velocity	cm/s
w	Thermal diffusion velocity	cm/s
W	Molecular weight	g/mol
x	Mole fraction	–
X	Mole fraction	–
X	Gas-density-column-length product	g/m^2
Y	Mass fraction	–

Greeks

α	Integrated band intensity	$cm^{-1}/g/m^{-2}$
α	Geometrical coefficient	–
α_p	Planck mean absorption coefficient	$m^{-1}atm^{-1}$
β	Line-width to spacing parameter	–
γ	Collisional half-width	cm^{-1}
δ	Characteristic length	cm
δ	Equivalent line spacing	cm^{-1}
η	Wavenumber	cm^{-1}
η	Adjusted line-width to spacing parameter	–
θ	Polar angle	–
Θ	Thermal diffusion ratio	–
κ	Absorption coefficient	$cm^{-1}atm^{-1}$
μ	Direction cosine	–
μ	Dynamic viscosity	kg/m/sec
ν	Frequency	Hz

ρ	Density	kg/m^3
σ	Damping coefficient	–
τ	Characteristic time scale	sec
τ	Transmissivity	–
τ	Stress tensor	sec^{-1}
τ_H	Optical depth	–
ϕ	Zenith angle	–
ω	Bandwidth parameter	cm^{-1}
ω	Ordinate weight	–
Ω	Solid angle	sr

Superscripts

0	Node center

Subscripts

b	Blackbody
F	Fuel side
i	Angular discretization index
j	Special discretization index
k	Species index
O	Oxidizer side
w	Wall
η	Spectral
∞	Infinity

Abstract

A Computational Study of Spherical Diffusion Flames in Microgravity with Gas Radiation

by

Songtao Tang

Co-Chairs: Hong G. Im and Arvind Atreya

The ultimate goal of this research is to extend the current understanding of the characteristics of spherical diffusion flames in microgravity. In particular, one of the key objectives is to assess the effects of gas radiation as a means to promote flame extinction. To investigate these phenomena, a one-dimensional computational model was developed to simulate the evolution of a spherical diffusion flame with consideration of detailed chemistry and transport properties. Various levels of radiation models were implemented and the results were compared with experimental measurements of flame radius and temperature profiles. It was shown that the statistical narrow band model (SNB) combined with the discrete ordinate method (DOM) reproduced the experimental results with highest accuracy, and this combination of the radiation models were adopted in the subsequent parametric studies.

The parametric studies explored the relative effectiveness of fuel- and oxidizer-side dilution on the flame radius and temperature behavior, with nitrogen, CO_2, and helium as diluents. In the spherical configuration considered in this study, the oxidizer-side dilution has a stronger effect on flame transient behavior than the fuel-side dilution, thereby suggesting a more effective means to induce flame extinction by dilution.

Study on various oxidizer-side dilution cases shows that CO_2 has a larger suppression effect than helium or nitrogen with the same dilution level. CO_2 dilution has multiple effects on flame behavior including radiation, thermodynamic, diffusion, and chemical effects. Quantitative analysis shows that the radiation effect is the primary factor accounting for flame temperature drop by approximately 60%, as compared to the thermal/diffusion (30%), and chemical effect (10%).

Considering the dominance of the radiative heat loss on flame extinction, a unified extinction criterion that applies to a wide range of parametric conditions was sought. The compiled computational results indicated that a critical flame temperature of 1130 K at extinction appears to be valid for most of the conditions under study. Therefore, it is concluded that extinction of spherical diffusion flame is primarily dictated by the local condition in the flame zone rather than by the volumetric radiative heat transfer in the surrounding gases.

Chapter 1 Introduction

For more than a century, Michael Faraday's lectures on "The Chemical History of a Candle" has kindled great interest in both younger generations and scientists. Since then, people have developed a much better understanding of the fundamental processes relevant to candle flames. However, there still remain many areas and issues that need further investigation. In recent years, boosted by the space exploration mission, study of combustion under microgravity conditions has extended our understanding of combustion science by providing gravity-free means to unravel important physical and chemical processes.

In this work, microgravity diffusion flame behavior, especially the extinction behavior, is extensively investigated. In particular, the role of various diluent gases on diffusion flame extinction is investigated in terms of their thermal, chemical, and radiative heat transfer effects.

1.1. Significance of Microgravity Combustion Research

As an important branch of combustion research, microgravity combustion is of great importance, both in academic research and in practical application. NASA is one of the leading institutes that have been actively supporting microgravity combustion science (http://microgravity.grc.nasa.gov/combustion/) during the past decades.

Microgravity combustion research has contributed significantly to a better understanding of fundamental combustion characteristics. In Earth's gravity, the presence of gravity influences the characteristics of diffusion flames in a number of ways. First, the buoyancy-induced flow field interacts with chemical reaction, thereby introducing asymmetry and more complex combustion behavior. Second, buoyancy also triggers instability in the flow which may eventually lead to the onset of turbulence. Furthermore, buoyancy modifies the transport processes which affect the transport of thermal energy,

reactants, and products. This effect is the strongest in the highest temperature regions of flames where most chemical reactions occur. On the contrary, microgravity condition eliminates all the difficulties and provides a configuration that is more symmetric and laminar. In microgravity the absence of buoyancy-induced flows significantly increases the residence time of gaseous products that are accumulated in the reaction zone, which provides an idealized environment to unravel many key sub-processes that can explain the highly complex combustion phenomena such as extinction/ignition and pollutant formation. In addition, heat loss due to soot radiation is increased and flame is much easier to quench, which helps to observe and investigate flame extinction both experimentally and computationally. A systematic understanding of flame characteristics in microgravity conditions can subsequently be extended to understand and predict combustion behavior in a more complex system.

Besides fundamental scientific significance, the investigation of microgravity flame behavior and extinction mechanisms is also important for fire safety applications. Various substances serve as extinguishing agents for a number of different reasons. For example, halogenated species are known to work as an inhibitor by scavenging radical pool. For space application, however, carrying an additional chemical agent may not be a desirable option. As an alternative, the ambient gases inside the spacecraft can be made such that any accidental creation of flames cannot sustain due to enhanced heat losses. This can be achieved by using different types of diluent gases in the ambient air. Thermal suppression of flames may result from the increased specific heat (thereby lowering the flame temperature), or from the increased conductive or radiative heat loss. To this end, it is important to understand which mode of thermal suppression is most effective in order to determine the appropriate choice of diluent gases.

In the next section, previous studies on various aspects of microgravity combustion phenomena will be reviewed and summarized.

1.2. Review of Microgravity Combustion Research

Since microgravity combustion has revealed many distinct fundamental aspects of combustion, extensive studies have been conducted on various issues through experiments, analysis, and numerical simulation. Microgravity conditions can be created

in a variety of facilities such as drop tower, sound rocket, parabolic flight aircraft, space shuttle, and space station. Different facilities have different quality and duration of microgravity conditions. Thus far, the drop tower has been the most commonly adopted facility for experimental research.

Similar as Earth's gravity combustion systems, most microgravity combustion systems fall into two categories, premixed and non-premixed (diffusion) combustion, when condensed phases are not involved. Since diffusion flames account for the majority of practical combustion systems, extensive research has been conducted, including the flame extinction behavior which will be the focus of this dissertation. Most of the previous studies in diffusion flames adopted one of three canonical configurations: gas-jet flames, counterflow flames, and spherical diffusion flames. While the jet and counterflow configurations have been extensively used in the study of stretch-induced flame extinction, the spherical diffusion flame has served as an alternative model problem in which flame extinction occurs at low-stretch conditions, thereby allowing a systematic investigation on the role of various heat losses on flame extinction.

During the past decade, Atreya and coworkers (Atreya *et al.*1994, 1995, 1998, 2001, Chernovsky *et al.* 2007) have extensively studied the effect of radiative heat loss on spherical microgravity diffusion flames both experimentally and analytically. Their experiments were undertaken in the 2.2-second drop tower in NASA Glenn Research Center, considering various fuels such as methane, ethylene, and acetylene in order to represent a wide range of fuels with various sooting tendency. In their experiments, flame radius, temperature, radiation intensity, and soot information were monitored, and their unique distributed temperature measurement at multiple locations discovered, for the first time, the radial temperature distribution for spherical diffusion flames.

One of the key issues in the experimental studies by Atreya and coworkers was the effect of dilution. To investigate this issue, different diluents were added to fuel and/or oxidizer side and the experimental observations were analyzed. A similar investigation was also conducted by Katta (2004, 2006), in which CO_2 and CF_3H were considered in cup-burner flames and concluded that oxidizer-side dilution has a stronger impact on flame behavior than fuel-side dilution. Lock and coworkers (2008) studied the suppression of methane-air partially premixed flames in both normal and microgravity

with different dilution options, and found that dilution on the deficient side is more effective. Throughout these studies, however, due partly to the difficulties in the experimental implementation for a wide range of dilution level, the observed results were not consistent among one another. Therefore, further investigation is needed in order to provide a conclusive answer to this issue. This can be done more effectively through computational model which can explore a wide range of mixture conditions more easily. Moreover, while one of the important issues of the experimental investigation was to understand the flame extinction characteristics, for all the cases considered no extinction was observed due to the limited duration (2.2 s) of the experimental measurement. A high-fidelity computational model allows reproduction of the transient flame behavior for much longer time, thereby serving as a useful tool to investigate the extinction characteristics.

Several other researchers have recently investigated spherical diffusion flame characteristics in the same 2.2-second drop tower facility. Tse *et al.* (2001) performed experiments on burner-generated spherical diffusion flames with H_2/CH_4/inert mixtures issued into atmosphere air, and they also set up a numerical model based on a modified Sandia Premixed code incorporating narrow band radiation model. For all the dilution cases in their study, no flame extinction was observed in experiments due to time limitation but their numerical model predicted extinction with a detailed radiation model. However, they did not consider different choices of diluent gases or various levels of dilution as a means to promote extinction.

Sunderland and coworkers (Sunderland *et al.* 2005, Santa *et al.* 2007) investigated spherical diffusion flames in microgravity. To achieve flame extinction within 2.2 seconds, they adopted an inverse configuration in which oxygen was issued into highly diluted ethylene. They also analyzed the flame extinction behavior with a similar computational model as that used by Tse *et al.* (2001). One of the significant findings in their study was that when flame extinction occurs the ratio of the radiation heat loss to heat release rate reaches a critical value of 0.7. Although different levels of dilution were investigated, only nitrogen was introduced as the diluent, such that it remains to be seen if the critical ratio of 0.7 can be generalized when other diluent gases (such as CO_2) with different thermodynamic and radiative properties are considered.

An important approach to control flame behavior and to assist in flame suppression is to change reactant concentrations by adding diluents. For example, a popular approach to extinguish a diffusion flame is to add extinguishing agent in the air which suppresses flame either by chemical inhibition or by enhanced conductive/radiative heat losses. Halons are effective fire extinction agents due to their chemical and thermal effects on flames, and as a result they have been applied widely. However, the adverse effect of chlorines on stratospheric ozone has led to strict regulations in the production and application of Halons since 1994 according to the Montreal Protocol. In addition, typical ventilation systems on spacecrafts can not easily remove the extinction agents from the environment after their application, making it difficult to adopt halons in long-duration space missions. Consequently, various inert gases have been considered as an alternative to replace Halons.

Among various candidates for flame suppressant gases, CO_2 has been widely studied considering its large heat capacity and radiative properties. However, CO_2 also has an issue of its biological impact on human respiratory system. Consequently, helium was also considered as a viable alternative in favor of its large heat conductivity. Although in the context of premixed combustion, Qiao and coworkers (2005) studied the suppression effects of different diluents on laminar premixed $H_2/O_2/N_2$ flames both experimentally and numerically, and reported that the suppression effect becomes stronger, in terms of the burning velocity, in the order of helium, argon, nitrogen, and CO_2. On the other hand, Son *et al.* (2006) compared CO_2 and helium as fire extinguishing agents for flames spared over thermally thick fuel beds in microgravity, and concluded that helium is actually preferred to CO_2 in microgravity applications due to the enhanced conductive heat loss. These two contrasting results suggest that more work needs to be done in order to completely understand the various roles of different diluent gases in affecting the flame suppression behavior.

In addition to the comparison among various diluent gases, the role of CO_2 on promoting flame extinction is not clearly understood. Liu and coworkers (2001) studied the chemical and thermodynamic effects of CO_2 as an additive in an ethylene counterflow flame by a contrived numerical experiment to isolate various effects of CO_2. They showed that the predominant effect of the CO_2 dilution in soot and NOx reduction was

the lower flame temperature resulting from the higher heat capacity of CO_2. Similarly, Park and coworkers (2003) analyzed the effects of CO_2 on the flame structure in H_2-O_2 counterflow diffusion flames, reporting that the reduction of flame temperature is due to both thermal and chemical effects. In a similar study of counterflow flames, Lee and co-workers (2001) concluded that both thermal and radiation effects of CO_2 addition play an important role in flame weakening.

Since radiation has been considered one of the important effects in microgravity combustion, development and implementation of a reliable radiative heat transfer model is essential in reliable computational studies. The radiation models are categorized based on level of resolution in the spectral and spatial domains. In terms of the spectral resolution, the simplest approach is to use the gray-gas approximation which assumes that all the radiative properties are independent of wave number and are only functions of temperature and partial pressure. As an improvement in introducing spectral resolution, various models exist such as, in the order of complexity, the exponential wide band model (EWBM) (Lallemant and Weber 1996), spectral line-based weighted-sum-of-gray-gases model (SLW) (Denison and Webb 1993, 1995), correlated-K method (CK) (Goody and West *et al*. 1989), and statistical narrow-band model (SNB) (Soufiani and Taine 1997). To provide accurate spatial information of the radiation intensity, the radiative transfer equations (RTE) must be solved in the spherical coordinate system. As for the associated spatial resolution, the simplest approach is to assume that all the gases are optically thin, such that the radiative heat loss terms are determined locally (Barlow *et al*. 2001). For better accuracy in a system with participating media, a number of ways to solve the RTE system exist, including the discrete ordinate method (DOM) (Fiveland 1987, Truelove 1987, Liu *et al*. 2002), the discrete transfer method (DTM) (Lockwood and Shah 1981), and the Monte Carlo model (Siegel and Howell 1992). Various radiation models have been applied and compared for reacting flow simulations (Liu *et al*. 2004, Coelho 2004). Among the various radiation models available, there is no quantitative assessment of relative accuracy for a specific choice of physical problems. In this study, we attempt to provide such information in the context of low stretch spherical diffusion flames in microgravity.

When gas phase radiation across a domain is considered, emission and absorption are two major factors. The radiation emitted from one location travels in the domain and is gradually reabsorbed/attenuated before it leaves the calculation domain, and reabsorption thus becomes important in some cases. Ju and coworkers (1998) investigated the effects of adding CO_2 in flames spared over thermally thick fuel beds in microgravity and found that the reabsorption increases burning velocity and extends flammability limits considerably. Son and coworkers (2006) studied flames spared over thermally thick fuel beds in microgravity and pointed out that the reabsorption of CO_2 reduces the suppression effects of it compared with helium. Strong reabsorption is also expected to happen in our flame configuration especially when CO_2 is used as diluents, so the reabsorption effect on spherical diffusion flame extinction will be evaluated in this study.

1.3. Objectives

The ultimate goal of this project is to extend the current understanding of the characteristics of spherical diffusion flames in microgravity. The spherical diffusion flame configuration in microgravity has played a unique role by allowing well-defined flame structure under low stretch conditions in the absence of the buoyancy effect. Some of the key issues investigated in the present study include the effects of dilution and associated radiative heat losses on the flame behavior such as growth rate, temperature, and extinction. Previous studies as reviewed in Section 1.2 have raised a number of questions that require further investigation, as summarized in the following.

Previous experimental work (Chernovsky 2007) considered dilution on either fuel or oxidizer side in order to understand their relative effectiveness on flame extinction. Since the cases considered were limited, there is a need to extend this study to consider a wider range of parametric conditions. Therefore, extensive computational studies for a wider range of parametric conditions will be conducted in order to provide more conclusive answers to this issue.

Different diluents have been investigated for their relative effectiveness in flame extinction. Although CO_2 has been regarded as an effective extinguishing agent, recent researches suggested that helium can be more favorable especially in microgravity conditions. In this study, we will attempt to compare CO_2 and helium as suppression

agent through an in-depth investigation of various physical mechanisms responsible for flame suppression. For each diluent, how suppression effect depends on the amount of dilution will also be assessed.

It is well understood that the effects of radiative heat loss can become a dominant factor for flame quenching at low stretch conditions. Therefore, for accurate description of the extinction behavior of spherical diffusion flames in microgravity, more advanced radiative models need to be considered. However, so far no quantitative assessment has been provided as to the appropriate level of complexity in the radiation model to be used in microgravity flame studies. The present study will attempt to compare the results with various radiation models against experimental measurements of temporally and spatially resolved flame radius and temperature history.

Although CO_2 has been considered in many previous studies as a diluent gas, the main physical mechanism responsible for flame weakening and extinction is not clearly understood. Some studies reported that it is due to the thermodynamic (specific heat) effect; others attributed the key mechanism to radiative heat loss. In this study, we will attempt to quantitatively evaluate the relative importance of various effects, such as thermal, transport, chemical, and radiation, in enhancing flame extinction.

As a related issue concerning flame extinction, Sunderland and coworkers (Sunderland *et al.* 2005, Santa *et al.* 2007) have suggested that there may be a general criterion for the spherical flame extinction. In their study, however, the parametric conditions considered were fairly limited, making it difficult to generalize the concept for a wider range of conditions. In this study, we will assess various extinction criteria for a greater number of conditions as an attempt to identify a unified criterion for microgravity diffusion flame extinction.

1.4. Outline of Subsequent Chapters

The contents of the following chapters are summarized as follows.

In Chapter 2, the mathematical formulation is constructed for a spherical diffusion flame model, with consideration of detailed species transport and chemical reactions.

In Chapter 3, different radiation models for radiation properties and radiative transfer equation solvers are discussed, and the simulation results with different radiation models

are compared with experimental data in terms of flame radius growth rate and temperature history. An appropriate radiation model for subsequent studies is identified considering both accuracy and computational efficiency.

In Chapter 4, the numerical simulation results are compared with experimental results under various conditions of fuel/oxidizer composition. Flame ignition method and a number of topics relevant to radiation modeling are also discussed.

In Chapter 5, results from the fuel-side and oxidizer-side dilution cases are compared in terms of their relative impact on the flame radius and temperature behavior. This will help us identify preferred means to induce flame extinction by dilution.

In Chapter 6, extensive parametric analysis is conducted for detailed description of the flame characteristics. In particular, the effect of diluent species type (nitrogen, CO_2, and helium) and the amount of dilution on flame radius and temperature are discussed. Discussion on critical heat loss and critical temperature for extinction further provides a means to characterize the onset of flame extinction. Various effects, including chemical, thermal, diffusion, and radiation effects will be quantitatively analyzed and their relative importance in flame extinction is assessed. The flame extinction and ignition behavior with different diluents is subsequently investigated. Considering that no steady spherical diffusion flame has been observed in previous experimental studies, an attempt is made to assess the existence of steady spherical flame by conducting computational simulations for a long period of time.

In Chapter 7, the key scientific findings of the present study are summarized and possible future research subjects are discussed.

Chapter 2 Model Description

This NASA-funded project is comprised of both experimental exploration and numerical modelling approach. Although this dissertation is focused on the modelling part, it is helpful to introduce the experimental counterpart before describing the computational model.

2.1. Introduction to the Experiments

All experiments were carried out in the 2.2-second drop tower at the NASA Glenn Research Center. The experimental drop-rig consisted of a sealed test chamber, a spherical porous burner of radius 0.8 cm, a hot wire igniter, thermocouples, video cameras, *etc*. In the experiments, fuel is provided through the feeding duct at the controlled flow rate and comes out of the porous burner evenly. Ignition is accomplished by an electric igniter positioned in the vicinity of the burner. Test starts when the experimental chamber begins its free fall, resulting in a microgravity environment inside it. About 0.01 second after the start, the igniter heating wire is switched on and at the same time fuel starts flowing. The fuel-air mixture formed near the igniter wire is ignited. The flame quickly surrounds the spherical burner and the heating wire is retracted automatically. The ignited flame propagates freely in microgravity condition until the chamber hit the ground in about 2.2 seconds which concludes the experiment. During the experiments, a video camera is used to capture the pictures of the flame at a sampling frequency of 30Hz. The flame radius was determined from these pictures. Eight thermocouples were installed inside the chamber to monitor the temperature at different positions from the burner surface and to obtain a temperature distribution along radial coordinate. The thermocouple sampling frequency was 50Hz and multi-step post-processing approach was developed to derive final adjusted from original thermocouple voltage output. In these experiments photo-detectors were also used to measure flame

radiation in wavelengths sensitive to H_2O, CO_2, and hydrocarbons. Radiation data were sampled at the frequency of 200Hz, and the measurement was carried out at the position of 11.4 cm from the burner center.

Although different fuel species were used in preliminary tests, only ethylene was chosen as the fuel for all formal experiments partly because its chemical reaction mechanism is well characterized. Different diluents were used in the experiments on fuel and/or oxidizer side, including N_2, CO_2, and helium. In the experiments, fuel was provided at a constant volume flow rate of 6 ml/s, and the ambient temperature of both fuel and oxidizer was kept at 300K.

2.2. Introduction to Modeling Approach

In this section, the conservation equations to describe one-dimensional spherical diffusion flames are formulated and the associated numerical method is discussed.

2.2.1. Governing Equations

Assuming spherically symmetry, the conservation equations for mass, radial momentum, energy, and species in a spherical coordinate system, (r,θ,ϕ), are reduced to a one-dimensional form given by (Kuo, 2005):

$$\frac{\partial \rho}{\partial t}+\frac{1}{r^2}\frac{\partial}{\partial r}\left(\rho u r^2\right)=0, \tag{2.1}$$

$$\rho\left(\frac{\partial u}{\partial t}+u\frac{\partial u}{\partial r}\right)=-\frac{\partial p}{\partial r}+\frac{1}{r^2}\frac{\partial}{\partial r}\left(r^2\tau_{rr}\right)-\frac{\tau_{\theta\theta}+\tau_{\phi\phi}}{r}, \tag{2.2}$$

$$\begin{aligned}&\overline{C_p}\rho\left(\frac{\partial T}{\partial t}+u\frac{\partial T}{\partial r}\right)-\left(\frac{\partial p}{\partial t}+u\frac{\partial p}{\partial r}\right)\\&=\frac{1}{r^2}\frac{\partial}{\partial r}\left(\lambda r^2\frac{\partial T}{\partial r}\right)-\sum_{k=1}^{K}\left(\dot{\omega}_k\Delta h^{\circ}_{f,k}W_k\right)-\rho\sum_{k=1}^{K}\left(C_{p,k}\left(YV\right)_k\right)\frac{\partial T}{\partial r}-\nabla\cdot\mathbf{q}_R\end{aligned}, \tag{2.3}$$

$$\rho\left(\frac{\partial Y_k}{\partial t}+u\frac{\partial Y_k}{\partial r}\right)+\frac{1}{r^2}\frac{\partial}{\partial r}\left(r^2\rho\left(YV\right)_k\right)=\dot{\omega}_k W_k \qquad \left(k=1,2,...,K\right), \tag{2.4}$$

and the above equations are closed by the following ideal gas equation of state:

$$\rho=P\overline{W}/RT, \tag{2.5}$$

In actual calculations, we only solve for $p, u, T, Y_k (k = 1,2,..., K)$ as dependent variables and density ρ is determined by Equation (2.5) when necessary. Since ρ does not constitute a solution variable, the first term in the mass conservation Equation (2.1) is rewritten in terms of the actual solution variables as:

$$\frac{\partial \rho}{\partial t} = \frac{\rho}{P}\frac{\partial P}{\partial t} - \frac{\rho}{T}\frac{\partial T}{\partial t} - \rho \overline{W} \sum_k \left(\frac{1}{W_k} \frac{\partial Y_k}{\partial t} \right). \tag{2.6}$$

Note that the total pressure *P* is not a solution variable because it can be decomposed into the thermodynamic (p_0) and hydrodynamic (p) components by an asymptotic expansion in *Ma*.

$$P = p_0(t) + p(t, r) + o(Ma^2). \tag{2.7}$$

where p_0 is assumed constant at 1 atm while *Ma* is negligible because velocity is much smaller than the speed of sound in the incompressible system, as a result the total pressure is solely determined by the hydrodynamic pressure.

Since the continuity equation is first order and is only neutrally stable, an artificial damping term is introduced to maintain numerical stability. Thus, a numerical damping term of the form $\sigma \frac{(\Delta r)}{u_0} \left(\frac{\partial^2 p}{\partial r^2} \right)$ is added, where u_0 is a reference velocity and σ is a coefficient which is kept sufficiently small in order to ensure that the solution is not affected by numerical diffusion. From our experience, $\sigma \approx 10^{-3}$ appears to be acceptable without noticeably affecting the final solution (Sankaran and Im, 2002). Consequently, the final form of mass conservation equation is given by:

$$\rho \left(\frac{1}{P}\frac{\partial P}{\partial t} - \frac{1}{T}\frac{\partial T}{\partial t} - \overline{W} \sum_k \left(\frac{1}{W_k} \frac{\partial Y_k}{\partial t} \right) \right) + \frac{1}{r^2}\frac{\partial}{\partial r}\left(\rho u r^2 \right) - \frac{\sigma \Delta r}{2u_0}\frac{\partial^2 P}{\partial r^2} = 0. \tag{2.8}$$

In the momentum conservation equation, the viscous stress tensor terms for Newtonian fluids are given as:

$$\tau_{rr} = \mu \left(2\frac{\partial u}{\partial r} - \frac{2}{3}\frac{1}{r^2}\frac{\partial}{\partial r}\left(r^2 u \right) \right), \tag{2.9}$$

$$\tau_{\theta\theta} = \tau_{\phi\phi} = \mu \left(2\frac{u}{r} - \frac{2}{3}\frac{1}{r^2}\frac{\partial}{\partial r}\left(r^2 u \right) \right), \tag{2.10}$$

such that Equation (2.2) is rewritten as:

$$\rho\left(\frac{\partial u}{\partial t}+u\frac{\partial u}{\partial r}\right)=-\frac{\partial p}{\partial r}+\frac{4}{3}\left(\frac{\partial u}{\partial r}-\frac{u}{r}\right)\frac{\partial \mu}{\partial r}+\frac{4}{3}\mu\left(\frac{\partial^2 u}{\partial r^2}+\frac{2}{r}\frac{\partial u}{\partial r}-\frac{2u}{r^2}\right). \tag{2.11}$$

The energy conservation Equation (2.3) can be simplified further. For subsonic flows, the pressure gradient terms are negligible as long as the thermodynamic pressure does not vary significantly. Therefore, Equation (2.3) is simplified to the following form:

$$\begin{aligned}&\overline{C_p}\rho\left(\frac{\partial T}{\partial t}+u\frac{\partial T}{\partial r}\right)\\&=\frac{1}{r^2}\frac{\partial}{\partial r}\left(\lambda r^2\frac{\partial T}{\partial r}\right)-\sum_{k=1}^{K}\left(\dot{\omega}_k\Delta h^{\circ}_{f,k}W_k\right)-\rho\sum_{k=1}^{K}\left(C_{p,k}\left(YV\right)_k\right)\frac{\partial T}{\partial r}-\nabla\cdot\mathbf{q}_R\end{aligned}. \tag{2.12}$$

The diffusion velocity of each species, V_k, is composed of three parts:

$$V_k=v_k+w_k+V_c. \tag{2.13}$$

In the above, v_k is the ordinary diffusion velocity and is given using the Curtiss-Hirschfelder approximation (Parker, J. G., 1959) by

$$v_k=-D_{km}\frac{1}{X_k}\frac{dX_k}{dr}, \tag{2.14}$$

where X_k is the mole fraction, and the mixture-averaged diffusion coefficient D_{km} is given explicitly in terms of the binary diffusion coefficients $\hat{D}_{kj}$:

$$D_{km}=\frac{1-Y_k}{\sum_{j\neq k}^{K}\left(X_j/\hat{D}_{kj}\right)}. \tag{2.15}$$

The thermal diffusion velocity, w_k, is considered only for light species, such as H and H_2. The trace, light-component limit is employed in determining w_k, such that

$$w_k=-\frac{D_{km}\Theta_k}{X_k}\frac{1}{T}\frac{dT}{dr}, \tag{2.16}$$

where Θ_k is the thermal diffusion ratio. The negative sign of Θ_k makes the lower molecular weight species diffuse from low to high temperature regions.

The correction velocity V_c, which is independent of species but a function of the coordinate r, is included to ensure that the mass fractions sum to unity (or equivalently

$\sum_{k=1}^{K} Y_k V_k = 0$). This formulation of the correction velocity is recommended by Coffee and Heimerl (1981).

In summary, equations (2.4), (2.8), (2.11), and (2.12), are numerically solved to obtain solution variables $p, u, T, Y_k (k = 1,2,..., K)$.

2.2.2. Numerical Method

The conservation equations are solved by a finite difference method. A second order central differencing is used for the diffusive terms. Convective terms use upwind differencing, and the pressure gradient term in the momentum equation uses downwind differencing. Although the first order upwind scheme introduces numerical diffusion, sufficient grid resolution was made to ensure the solution accuracy. The upwind treatment avoids unwanted oscillations of the solution variables especially on a coarse mesh.

Fig. 2.1 shows the flow chart of the algorithm of the program. The upper part of the modules are the standard CHEMKIN (Kee *et al*. 1980, 1990) programs, and the three large blocks, the steady, unsteady, and radiation modules, are the new development from the present study. Prior to running the main programs of either the steady or the unsteady solvers, several data files need to be created. The detailed chemical reaction mechanism ("chem.inp") and the corresponding thermodynamic data ("therm.dat") are pre-processed by the CHEMKIN interpreter (Kee *et al*. 1980, 1990) to generate the chemistry database ("chem..asc"). Simultaneously, the associated transport property data ("tran.dat") are processed by the TRANSPORT program (Kee *et al*. 1983) to produce the general transport database ("tran.asc"). These two data files are linked to the main programs to provide all the necessary information of chemical reaction, thermodynamic, and transport properties for the multicomponent system.

The main program has two separate application modules: steady and unsteady solvers. For the steady solutions, Twopnt (Grcar 1992) is used to find the steady solution by the Newton iteration technique. For unsteady problems, DASPK (Petzold 1983) is used to integrate the system of differential-algebraic equations (DAE). The initial conditions for the unsteady problem can be generated by a prescribed solution field or a

converged steady solution obtained from the steady solver. Transient calculations can also be restarted from a previously obtained transient solution field.

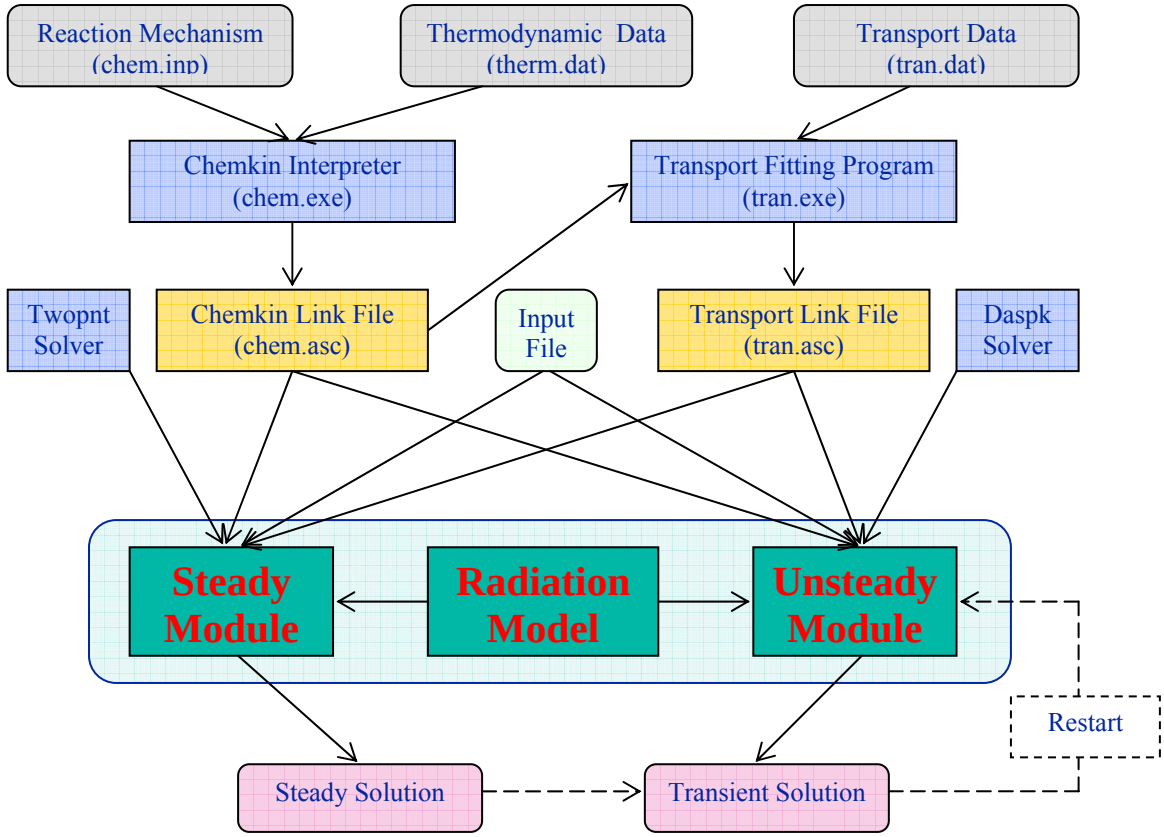

Figure 2.1: Schematic of the numerical program modules.

2.2.3. Spatial Discretization

The model can solve both steady and unsteady problems. For steady problems, the calculation domain is usually confined in a narrow region near the burner surface where initial uniform meshes are given. Through the iteration process, additional grid points are added when necessary, such that a fixed zonal grid refinement is completed based on the final steady solution.

Establishing grid structure for unsteady calculations requires additional consideration. Upon ignition, the initial spherical flames are formed near the burner surface, and the flame size subsequently grows in the radial direction. Therefore, a large computational domain is needed in order to simulate the transient behavior for a long period of time. After extensive test simulations, we adopted the domain size of 56 cm which was found

to be sufficiently large to reproduce the 2.2-second drop tower experiments (Atreya *et al*. 2001, Chernovsky *et al.* 2007) without the solutions being affected by the imposed outflow boundary conditions.

For transient calculation, the grid system is prescribed and not updated. Although adaptive mesh refinement (AMR) (Winkler *et al*. 1985, Li *et al*. 1998, Hyman *et al*. 2003, White 1982, Sanz-Serna *et al*. 1986, Blom *et al*. 1988) may provide elegant and efficient way to capture the moving flame zone, we found that a fixed zonal mesh refinement is adequate for the present study since the flame does not extend out significantly during the computation time which typically runs a few seconds. In the zonal mesh refinement approach, depending on how initial conditions are provided (see Section 2.5 for details) two different schemes are applied to ensure sufficient spatial resolution within the flame region. If the calculation starts from prescribed initial profiles, a uniform mesh is first applied through the entire domain and the region near the burner surface is refined with much denser grid structure. However, if a converged steady solution within a confined region is used as the initial condition, a hybrid grid structure is adopted in which the grid structure in the steady solution is kept near the burner surface and the additional outer domain is discretized with a separate zonal refinement. In both cases, grid convergence tests were conducted to ensure the solution accuracy. A typical grid size for fully manual meshes ranges from 0.005 cm to 1 cm throughout the domain, with a maximum grid extension ratio between the neighboring points not exceeding 2.

2.2.4. Boundary Conditions

Implementation of correct boundary conditions is critical in achieving accurate solutions. Considering the underlying physical characteristics of the model, the following boundary conditions are applied:

- Inlet boundary (burner surface)

  For continuity equation: $\dot{m} = \rho u A$, (2.17)

  For momentum equation: $dp/dr = 0$, (2.18)

  For energy equation: $T = T_F$, (2.19)

  For species equation: $Y_{kF} = Y_k + \rho Y_k V_k A/\dot{m} \qquad (k = 1,2,...,K)$, (2.20)

- Outflow boundary (outer domain boundary),

For continuity equation:

$$\dot{m} = \rho u A, \text{ for steady calculations} \quad (2.21)$$

$$d\dot{m}/dr = d(\rho r^2 u)/dr = 0, \text{ for transient calculations} \quad (2.22)$$

For momentum equation: $p = p_0$, (2.23)

For energy equation: $T = T_0$, (2.24)

For species equation: $Y_k = Y_{kO} (k = 1,2,...,K)$. (2.25)

In the above, p_0 is ambient pressure, T_0 is ambient temperature, and Y_{kF} and Y_{kO} are species concentrations on fuel and oxidizer sides, respectively $(k = 1,2,...,K)$. The fixed-value outflow boundary conditions were found to be reasonable as long as the domain size is sufficiently large so that the flame does not approach the boundary during the simulation.

In experiment the upstream volume flow rate was always 6 ml/s, which accordingly determines the mass flow rate for each case with the given fuel composition; therefore, constant mass flow rate $\dot{m}$ was assumed in simulation. When a computational case was performed as a comparison with experimental data, the mass flow rate $\dot{m}$ was always calculated from the experimental volume flow rate 6 ml/s; otherwise when a parametric study was performed, the mass flow rate $\dot{m}$ could be calculated from a different volume flow rate.

2.2.5. Initial Conditions

For the steady calculation, an initial guess for the solution variable profiles is always needed. For this purpose, we first choose an estimated flame location, and impose a Gaussian profile of temperature, hyperbolic tangent profile of species mass fraction, and velocity profile that satisfies continuity equation. For the mass fraction profiles, fuel and oxygen are appropriately overlaid near the peak temperature location. If the initial guess is chosen reasonably well, the Newton-Raphson iteration process converges to the correct steady solution.

One of the significant challenges in reproducing the experimental results by the computational model was to establish appropriate initial conditions. In the experiment (Atreya *et al*. 2001, Chernovsky *et al.* 2007), a flame was initiated by a wire igniter

placed approximately 2 mm from the burner surface. Exact replication of such conditions in simulations is difficult because the detailed parametric conditions generated by the igniter are not known.

To best represent the experimental situation, a number of alternative initial conditions were attempted. First, an external heat source in a Gaussian distribution was imposed in the initial profile in order to mimic the heat release from the wire igniter, a uniform temperature profile was imposed, and species mass fraction profiles were also given as in the steady calculation. Second, an explicit temperature profile was imposed in a form similar to the steady flame solution but somewhat narrower in thickness. Finally, a steady diffusion flame solution within a confined region near the burner surface was computed and imposed. Further discussion regarding the comparison of different initial conditions will be given in Chapter 4.

As a numerical method, initial condition inevitably has some uncertainties that, theoretically, will have an impact on the transient solution but the impact is expected to attenuate with time. An important question is how soon we would expect the impact to dissipate so that the transient solution is not significantly affected by the uncertainties in the initial condition. To answer this question we can consider a similar case where an initial narrow temperature spark starts diffusing into the ambient air, and the characteristic diffusion time scale τ_{diff} for the spark to be fully released is on the order of $\delta^2/D = 0.6^2/1.72 \approx 0.2$ second, where δ is the characteristic length corresponding to the initial flame width and D is the diffusion coefficient. For the case in our study, in order to ensure that the uncertainties in the initial condition do not have a significant impact on the transient solution, a time on the order of 0.2 second is enough.

Chapter 3 Radiation Modeling

Gas radiation is one of the major constituent of flame extinction and therefore needs special consideration. A complete gas radiation model involves two submodels, radiation property model which deals with the calculation of gas radiation properties and radiative transfer model which solves the radiative transfer equation (RTE).

3.1. Radiation Property Model

According to quantum mechanics theory, a gas molecule can emit or absorb photons at distinct wavenumbers or frequencies. A single spectral line at a certain spectral position is characterized by its strength and its line half-width, both of which are dependent on local temperature and pressure, and different spectral lines may overlap with each other. There are easily tens of thousands of spectral lines and their characteristics are very complex; therefore, it is literally impossible to describe radiation properties accurately and appropriate models are usually applied instead.

The various radiation property models can be categorized into four groups according to their complexity and accuracy: line-by-line model, narrow band model, wide band model, and gray gas model.

3.1.1. Line-by-line model

The line-by-line model is by far the most accurate gas radiation property model, but it demands tremendous computing time. The model relies on detailed knowledge of individual spectral lines, in which several hundred thousand wavenumbers are considered. In most cases, the line-by-line model is applied as the benchmarks for the validation of other approximate spectral models and is hardly feasible for practical engineering application. The most popular line-by-line model was developed by Taine (1983) and Hartmann *et al*. (1984), which is based on the HITRAN database developed by Rothman *et al*. (1992, 1998).

3.1.2. Narrow band model

In the narrow band model, the entire spectral domain (practically a sufficiently wide spectral range) is divided into many narrow spectral bands, and radiation property (absorption coefficient) is appropriately averaged over each narrow spectral band. In principle, the narrow band model can be as accurate as the line-by-line model as long as sufficiently accurate narrow band averages can be found. To find narrow band values of the absorption coefficient, some information about spectral lines must be available. Part of the basic information is the profile of a single spectral line. There are several commonly adopted assumptions of line shape: Lorentz shape, Doppler profile, and Voigt profile (Goody *et al.*, 1989). Among these, the Lorentz shape is the most popular and is used in this work. Common narrow band models include Elsasser model, in which equally spaced lines of equal intensity are considered, and statistical models, in which the spectral lines are assumed to have random spacing and/or intensity.

Different statistical models have been developed with different line strength probability distributions. Three popular models are the uniform statistical model, Goody model (1952), and Malkmus model (1967). The uniform statistical model is the simplest statistical model which assumes identical strengths for all the lines. Goody model assumes varying line strengths, and Malkmus modified it to obtain the Malkmus model assuming exponential-tailed inverse line strength distribution. When using the Malkmus model with Lorentz line shapes, the transmissivity averaged over a $\Delta\nu$ wide spectral interval of a homogeneous and isothermal column of length l (in cm), total pressure p (in atm), and molar fraction x in the considered absorbing gas is given by (Soufiani *et al.* 1997),

$$\bar{\tau}^{\Delta\nu} = \exp\left[-2\frac{\gamma}{\bar{\delta}}\left(\sqrt{1+xpl\kappa\frac{\bar{\delta}}{\gamma}}-1\right)\right] \tag{3.1}$$

In this expression, κ (in $cm^{-1}atm^{-1}$), $1/\bar{\delta}$ (in cm) and γ (in cm^{-1}) are the model parameters (Ronney, 2003). The parameter γ is a typical collisional half-width of the lines of the absorbing gas. Based on extensive literature search, we adopt the following expressions for γ (in cm^{-1}):

$$\gamma_{CO_2} = \frac{p}{p_S}\left(\frac{T_S}{T}\right)^{0.7}\left[0.07x_{CO_2} + 0.058\left(1 - x_{CO_2} - x_{H_2O}\right) + 0.1x_{H_2O}\right] \tag{3.2}$$

$$\gamma_{H_2O} = \frac{p}{p_S}\left\{0.462x_{H_2O}\left(\frac{T_S}{T}\right) + \left(\frac{T_S}{T}\right)^{0.5}\left[0.079\left(1 - x_{CO_2} - x_{O_2}\right) + 0.106x_{CO_2} + 0.036x_{O_2}\right]\right\} \tag{3.3}$$

$$\gamma_{CO} = \frac{p}{p_S}\left[0.075x_{CO_2}\left(\frac{T_S}{T}\right)^{0.6} + 0.12x_{H_2O}\left(\frac{T_S}{T}\right)^{0.82} + 0.06\left(\frac{T_S}{T}\right)^{0.7}\left(1 - x_{CO_2} - x_{H_2O}\right)\right] \tag{3.4}$$

The average transmissivity in each spectral band can now be readily calculated to obtain the corresponding absorption coefficient from the Beer's law:

$$\tau_\eta = e^{-\kappa_\eta s}, \tag{3.5}$$

where s is the path length that the beam travels through.

Note that column length l in Equation (3.1) corresponds to local gird size. However, the path length in Equation (3.5) is calculated by the equivalent path length which is the mean beam length L_m. For the spherical geometry, the mean beam length is calculated from the two radii corresponding to the inner and the outer spherical shells, and the mean beam length is different for inward and outward beams as follows (Andersen 1997),

For inward beams:

$$L_m = \frac{2r_2}{3\left(\frac{r_1}{r_2}\right)^2}\left[1 - \left(\frac{r_1}{r_2}\right)^3 - \left(1 - \left(\frac{r_1}{r_2}\right)^2\right)^{\frac{3}{2}}\right], \tag{3.6}$$

For outward beams:

$$L_m = \frac{2r_2}{3}\left[1 - \left(\frac{r_1}{r_2}\right)^3 - \left(1 - \left(\frac{r_1}{r_2}\right)^2\right)^{\frac{3}{2}}\right], \tag{3.7}$$

where r_1 and r_2 denote the radius of the inner and outer spherical shells separately that correspond to the two ends of the beam in calculation.

For practical applications of SNB model, the spectral domain of interest is between 150 and 9300 cm^{-1} which covers the majority of thermal radiation in the present study and radiation beyond this region is neglected. The above spectral domain is evenly

discretized into 367 bands with a resolution of 25 cm^{-1}, and it has been shown (Riviere *et al.* 1994) that this width is sufficiently narrow to assume a constant Planck function inside each band for a given temperature in the range of 300-2500 K.

3.1.3. Wide band model

In many cases engineers are only concerned with either heat fluxes or divergences of heat fluxes over the entire spectrum, and therefore total absorption or emission in the entire band instead of in each single narrow band is of more interest. As a result, wide band models have attracted a lot of interest due to its simplicity in application.

There are different kinds of wide band models and the most popular ones are box model and exponential wide band model (EWBM). Box model was developed by Penner (1959) where the total band absorptance is approximated by a rectangular box of width $\Delta\eta_e$ (the effective band width) and height $\bar{\kappa}$. Based on this assumption, we can easily set up the relationship between total band absorptance, effective band width, band intensity, absorption coefficient, etc. Despite this model's simplicity, its accuracy is largely dependent on the correct choice of $\Delta\eta_e$ and large errors can occur. Therefore it is only recommended for very rough calculation.

Another wide band model, exponential wide band model, was first developed by Edwards and Menard (1964) and then gradually improved by Edwards and coworkers, see Edwards, Glassen, *et al.* (1967) and Weiner and Edwards (1968). Edwards (1976) has a classic paper discussing the details of this model's implementation which involves three major steps as described below in detail.

According to the wide band model theory, there are three important physical parameters: the integrated band intensity α_{ij}, the line-width to spacing parameter β_{ij}, and the bandwidth parameter ω_{ij} that can be used to calculate total gas band absorptances over a wide range of temperature, path length, and pressure conditions. So the first step is to calculate these physical parameters as functions of temperature, pressure, and wavenumber. The calculation can be applied for the most important combustion gases, H_2O, CO_2, CO, CH_4, NO, SO_2, etc.

In the second step, the adjusted line-width to spacing parameter η and the optical depth τ_H are calculated as follows,

$$\eta = \beta P_e \tag{3.8}$$

$$\tau_H = \alpha X / \omega \tag{3.9}$$

where equivalent pressure P_e and

$$P_e = \left\{(P/P_0)\left[1+(b-1)x\right]\right\}^n \tag{3.10}$$

$$X = \rho L \tag{3.11}$$

in which b and n are tabulated in Edwards (1976) and x is species mole fraction.

Thirdly the dimensionless band absorption A^* is calculated and then dimensional band absorption A is determined from $A = A^*\omega$. The calculation of A^* depends on the four-region expression:

1). The linear region: $\tau_H \le 1$, $\tau_H \le \eta$

$$A^* = \tau_H \tag{3.12}$$

2). The square root region: $\eta \le \tau_H \le 1/\eta$, $\eta \le 1$

$$A^* = (4\eta\tau_H)^{1/2} - \eta \tag{3.13}$$

3). The log-root region: $1/\eta \le \tau_H \le \infty$, $\eta \le 1$

$$A^* = \ln(\tau_H \eta) + 2 - \eta \tag{3.14}$$

4). The logarithmic region: $\tau_H \ge 1$, $\eta \ge 1$

$$A^* = \ln \tau_H + 1 \tag{3.15}$$

Fourthly, spectral locations are calculated for each band for the mixture gas and final spectral blocks are determined. Lastly, transmissivity and absorption coefficient are calculated for each block.

Although only a limited number of wavebands are virtually considered, the first step is very computational intensive, which has hindered its wide application. Thanks to the recent work of Lallemant and Weber (1996) who advanced an optimized procedure to calculate α_{ij} and β_{ij}, the exponential wide band model has become more popular in engineering application.

Despite the computational convenience of the wide band model, it is well recognized that wide band correlations have a typical correlational accuracy of ± 30%, and in some cases may be in error by as much as 70% (Modest, 2003). As a result, people need to very careful while applying wide band model in scientific research.

3.1.4. Gray gas model

In the gray gas model, detailed band information is neglected and the total radiation flux is calculated directly using spectrally integrated radiative properties. A popular approach is to calculate mean emissivities and absorptivities of gas columns with fitted polynomial equations.

Several mean absorption coefficients have been introduced and incorporated into various radiation models. The most popular mean absorption coefficient is the Planck mean, which describes the total emission from a medium, and which accurately describes radiative heat loss from an optically thin gas. Values of the Planck mean absorption coefficient are available for several molecular gases from Tien (1968), and recently Zhang et al. (2002) updated these values using upgraded HITRAN96 data. For easier application especially in numerical calculation, curve fits are provided by different researchers. Starting from RADCAL (Grosshandler, 1993) as the original database, Barlow *et al.* (2001) derive the mean absorption coefficients of CO_2, H_2O, CO, and CH_4 within temperature range of between 300K and 2500K. Note that, the original data in Barlow's paper has a typo and the corrected data are given as follows,

For H_2O and CO_2,

$$\begin{aligned}\alpha_p &= c0 + c1*(1000/T) + c2*(1000/T)^2 \\ &+ c3*(1000/T)^3 + c4*(1000/T)^4 + c5*(1000/T)^5\end{aligned} \tag{3.16}$$

with coefficients:

	H2O	CO2
c0	-0.23093	18.741
c1	-1.12390	-121.310
c2	9.41530	273.500
c3	-2.99880	-194.050
c4	0.51382	56.310

c5	-1.86840E-05	-5.8169

For CH4:

$$\alpha_{p,CH4} = 6.6334 - 0.0035686 * T + 1.6682E-08 * T^2 + 2.5611E-10 * T^3 - 2.655E-14 * T^4 \quad (3.17)$$

For CO:

$$\alpha_{p,CO} = c0 + T * (c1 + T * (c2 + T * (c3 + T * c4))) \quad (3.18)$$

with coefficients:

300 ≤ T ≤ 750K		750 < T ≤ 2500K
c0	4.7869	10.09
c1	-0.06953	-0.01183
c2	2.95775E-4	4.7753E-6
c3	-4.25732E-7	-5.87209E-10
c4	2.02894E-10	-2.5334E-14

In this study, the concentration of CH_4 is very low compared with CO2, H2O, and CO; therefore, only the radiation from the last three species is considered. The plot for these three species is given as,

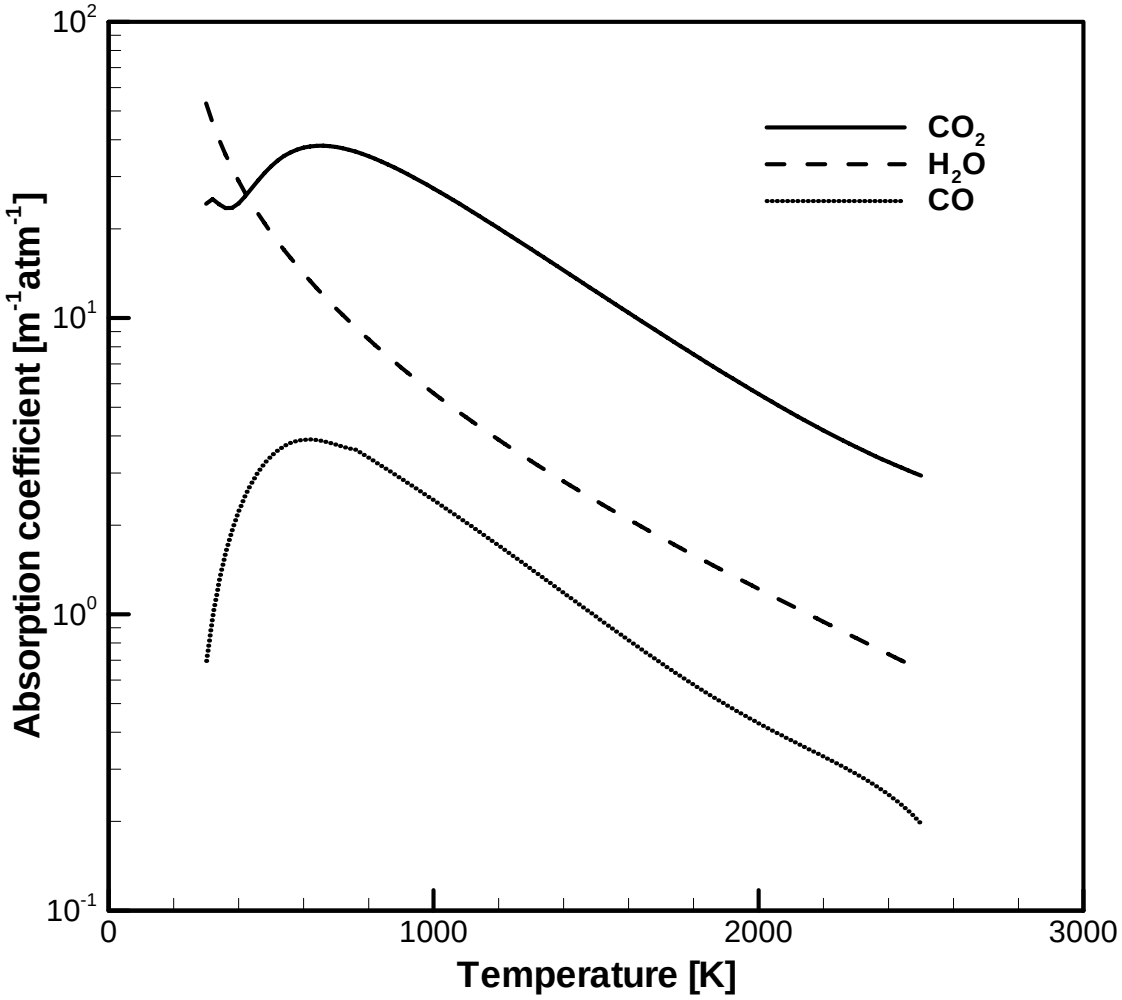

Figure 3.1: Absorption coefficient profiles as a function of temperature for different species.

3.2. Radiative Transfer Model

3.2.1. Introduction to the radiative transfer equation (RTE)

Energy equation is given as:

$$\overline{C_p}\rho\left(\frac{\partial T}{\partial t}+u\frac{\partial T}{\partial r}\right)-\left(\frac{\partial p}{\partial t}+u\frac{\partial p}{\partial r}\right)= \\ \frac{1}{r^2}\frac{\partial}{\partial r}\left(\lambda r^2\frac{\partial T}{\partial r}\right)-\sum_{k=1}^{K}\left(\dot{\omega}_k\Delta h^{\circ}_{f,k}W_k\right)-\rho\sum_{k=1}^{K}\left(C_{p,k}\left(YV\right)_k\right)\frac{\partial T}{\partial r}+q_{source}-\nabla\cdot\mathbf{q}_R \quad , \quad (3.19)$$

where the radiation term is the integration of spectral divergence of radiative heat flux vector,

$$\nabla \cdot \mathbf{q} = \int_0^\infty \nabla \cdot \mathbf{q}_\eta d\eta \,, \tag{3.20}$$

where

$$\nabla \cdot \mathbf{q}_\eta = \kappa_\eta \left(4\pi I_{b\eta} - G_\eta\right), \tag{3.21}$$

in which κ_η is spectral absorption coefficient, $I_{b\eta}$ is spectral black body radiation intensity, and G_η is the spectral incident radiation calculated by integrating local radiation intensity over the full solid angle as,

$$G_\eta = \int_{4\pi} I_\eta(\hat{\mathbf{s}})\, d\Omega \,. \tag{3.22}$$

Sometimes we are more interested in heat flux which is also a vector as a function of radiation intensity.

$$\mathbf{q}_{\text{rad}}(\mathbf{r}) = \int_{4\pi} I(\mathbf{r}, \hat{\mathbf{s}})\hat{\mathbf{s}}\, d\Omega \,. \tag{3.23}$$

From the above we find that the calculation of radiation term in energy equation relies on the information of radiation intensity at any spectral location, any space location, and any direction. As a result, the determination of radiation intensity is a crucial step as a separate effort from solving the energy equation and is implemented based on the radiative transfer equation (RTE).

For a quasi-steady system, the general formulation of radiative transfer equation for an absorbing, emitting, and anisotropically scattering medium is:

$$\hat{\mathrm{s}} \cdot \nabla I_\eta = \kappa_\eta I_{\mathrm{b}\eta} - (\kappa_\eta + \sigma_{\mathrm{s}\eta}) I_\eta + \frac{\sigma_{\mathrm{s}\eta}}{4\pi} \int_{4\pi} I_\eta(\hat{\mathbf{s}}_i)\Phi_\eta(\hat{\mathbf{s}}_i, \hat{\mathbf{s}})\, \mathrm{d}\Omega_i \,, \tag{3.24}$$

where κ_η is spectral absorption coefficient, $\sigma_{s\eta}$ is spectral scattering coefficient, and Ω_η is the scattering phase function and describes the probability that a ray from one direction, $\hat{\mathbf{s}}_i$, will be scattered into a certain other direction, $\hat{\mathbf{s}}$.

For most engineering applications, the quasi-steady assumption is satisfied, where the speed of light is sufficiently large compared with local time and length scales. The above equation is valid for a gray medium or, on a spectral basis, for a nongray medium, and is subject to the boundary condition:

$$I_w(\mathbf{r}_w, \hat{\mathbf{s}}) = \varepsilon(\mathbf{r}_w) I_b(\mathbf{r}_w) + \frac{\rho(\mathbf{r}_w)}{4\pi} \int_{\hat{\mathbf{n}}\cdot\hat{\mathbf{s}}'<0} I(\mathbf{r}_w, \hat{\mathbf{s}}') \left|\hat{\mathbf{n}} \cdot \hat{\mathbf{s}}'\right| d\Omega' \,, \tag{3.25}$$

where the enclosure is considered as opaque, diffusely emitting and diffusely reflecting walls.

In this study we assume that the medium only absorbs and emits but not scatters, so $\sigma_{s\eta} = 0$. Considering the one-dimensional spherical coordinate applied in the physical model in this project, we assume that radiation intensity is a function of radius only, then the radiative transfer equation is given by equation,

$$\mu \frac{\partial I}{\partial r} + \frac{1-\mu^2}{r} \frac{\partial I}{\partial \mu} + \kappa (I - I_b) = 0, \tag{3.26}$$

or alternatively,

$$\frac{\mu}{r^2} \frac{\partial}{\partial r} (r^2 I) + \frac{1}{r} \frac{\partial}{\partial \mu} [(1-\mu^2) I] + \kappa (I - I_b) = 0, \tag{3.27}$$

where μ is the cosine of the polar angle, measured from the radial direction.

3.2.2. Approximate solution methods for solving RTE

The complete radiative transfer equation for absorbing, emitting, and scattering media is an integro-differential equation for radiative intensity in the independent variables of space coordinates, direction coordinates, and spectral coordinates. The equation is very complicated and exact analytical solutions exist only for a few extremely simple situations, as a result approximate solution methods are needed in most engineering cases to solve the equation. Popular approximate methods include optically thin approximation, optically thick approximation, spherical harmonics method, discrete ordinate method, discrete transfer method, moment method, zonal method, among others. All these assumption models are committed to solve the volumetric radiation heat loss term which results from a balance between loss by emission and gain by absorption.

3.2.2.1 Optically thin approximation

Under optically thin approximation, each point in the space has an unimpeded isotropic view of the cold surroundings, and thus the radiative heat loss rate per unit volume is calculated as:

$$\nabla \cdot \mathbf{q} = 4\pi \int_0^\infty \kappa_{P\eta}(T) \left(I_{\eta b}(T) - I_{\eta b}(T_\infty) \right) d\eta . \tag{3.28}$$

Since optically thin approximation itself is normally applied as an inaccurate approach for radiation consideration, complicated band models are seldom adopted along with it, as a result the gray gas property model with mean absorption coefficient is most popularly applied. For the gray gas property model with optically thin approximation consideration, the above equation becomes:

$$\nabla \cdot \mathbf{q} = 4\sigma\kappa_P(T)\left(T^4 - T_\infty^4\right) = \kappa_P(T)\left(4\sigma T^4 - 4\sigma T_\infty^4\right). \tag{3.29}$$

For each single species, the Planck mean absorption coefficient can be determined with the method discussed in section *3.1.4*. For gas mixture which involves more than one radiative species, the overall Planck mean absorption coefficient is calculated as:

$$\kappa_P = \sum_i \kappa_{Pi}(T) P_i \ . \tag{3.30}$$

As another option, a more complicated band gas model could also be applied with optically thin approximation, for example, if narrow band model is chosen, the radiative heat loss rate per unit volume is:

$$\nabla \cdot \mathbf{q} = 4\pi \sum_{all\ \eta} \left(\kappa_{P\eta}(T)\left(I_{\eta b}(T) - I_{\eta b}(T_\infty)\right)\right), \tag{3.31}$$

however, this approach is seldom used.

3.2.2.2 Optically thick approximation

Entirely different from the above optically thin approximation, in optically thick media, the radiation decays very fast within a short distance and the probability that a photon propagates straight ahead without being impacted is very low. Normally optically thick media tends to be nearly isotropic and close to local equilibrium. Szoke and Brooks (2005) introduce a new analytical formulation for the transport equation which helps in numerical solutions of the equations of radiation hydrodynamics in optically thick regions.

3.2.2.3 Spherical harmonics method

Spherical harmonics method (or P_N method) was initially advanced by Jeans (1917) in the astronomy field and then applied in neutron transport field (Davison, 1958, Murray, 1957) and in thermal radiation field (Cheng, 1965, Cheng, 1966).

The process of solving radiative transfer equation is actually a process to calculate radiation intensity from an integro-differential equation in five independent variables, three space coordinates and two direction coordinates. Spherical harmonics method is an approach to find an approximate solution of arbitrarily high order by converting the radiative transfer equation into a set of simultaneous partial differential equations.

Spherical harmonics method is a relatively simple approach to solve radiative transfer equation; however, it may bring about large calculation errors especially for optically thin media. In this study, since the media varies in a wide range including optically thin and optically thick cases it is not recommended to apply spherical harmonics method.

3.2.2.4 Discrete ordinate method (DOM)

Similar to the spherical harmonics method, discrete ordinate method (or S_N method) also converts the radiative transfer equation into a group of simultaneous partial differential equations. It was initially developed by Chandrasekhar (1960) in stellar and atmospheric radiation and then more interest arose in neutron transport field (Lee, 1962, Lathrop, 1966, Carlson and Lathrop, 1968) and thermal radiation field (Love, 1965, Hsia, 1967, Hottel, 1968).

In discrete ordinate method, RTE is solved for a set of N different directions $\hat{\mathbf{s}}_i$, $i = 1, 2, \ldots, N$, and the integrals over direction are replaced by numerical quadratures:

$$\int_{4\pi} f(\hat{\mathbf{s}}) d\Omega \cong \sum_{i=1}^{N} \omega_i f(\hat{\mathbf{s}}_i), \tag{3.32}$$

where the ω_i are the quadrature weights associated with the directions $\hat{\mathbf{s}}_i$.

In DOM model, radiative heat flux q and incident radiation G are given as:

$$G(r) = \sum_{i=1}^{N} \omega_i I_i(r), \tag{3.33}$$

$$q(r) = \sum_{i=1}^{N} \omega_i \mu_i I_i(r), \tag{3.34}$$

and the divergence term in energy equation is:

$$\nabla \cdot \mathbf{q} = \int_0^\infty \kappa_\eta \left(4\pi I_{b\eta} - G_\eta\right) d\eta = \int_0^\infty \kappa_\eta \left(4\pi I_{b\eta} - \sum_{i=1}^{N} \omega_i I_{i,\eta}(r)\right) d\eta. \tag{3.35}$$

In order to solve radiation intensity from Equation (3.27), we apply central difference on the derivative term of μ (Modest, 2003) and rewrite it into,

$$\mu_i \frac{\partial I_i}{\partial r} + \frac{\mu_i}{r} I_i + \frac{\alpha_{i+1/2} I_{i+1} - \alpha_{i-1/2} I_{i-1}}{2r\omega_i} + \kappa\left(I_i - I_b\right) = 0\,, \tag{3.36}$$

where $I_{i\pm 1/2}$ is evaluated at the angular edges between ordinate i and i+1, and the geometrical coefficients α are determined by,

$$\alpha_{i+1/2} = \alpha_{i-1/2} - 2\mu_i\omega_i\,, \tag{3.37}$$

and

$$\alpha_{1/2} = \alpha_{N+1/2} = 0,\ i = 1, 2, ..., N \tag{3.38}$$

Depending on the number of ordinate N, we have a set of values for coefficient μ_i and weight ω_i (i = 1, 2, …, N), for example, when N = 4, we have,

$$\mu_1 = -0.9082483,\ \mu_2 = -0.2958759,\ \mu_3 = 0.2958759,\ \mu_4 = 0.9082483 \tag{3.39}$$

$$\omega_1 = 2.0943951,\ \omega_2 = 4.1887902,\ \omega_3 = 4.1887902,\ \omega_4 = 2.0943951 \tag{3.40}$$

and Figure 3.2 shows the diagram of the discrete ordinates for 4 ordinates.

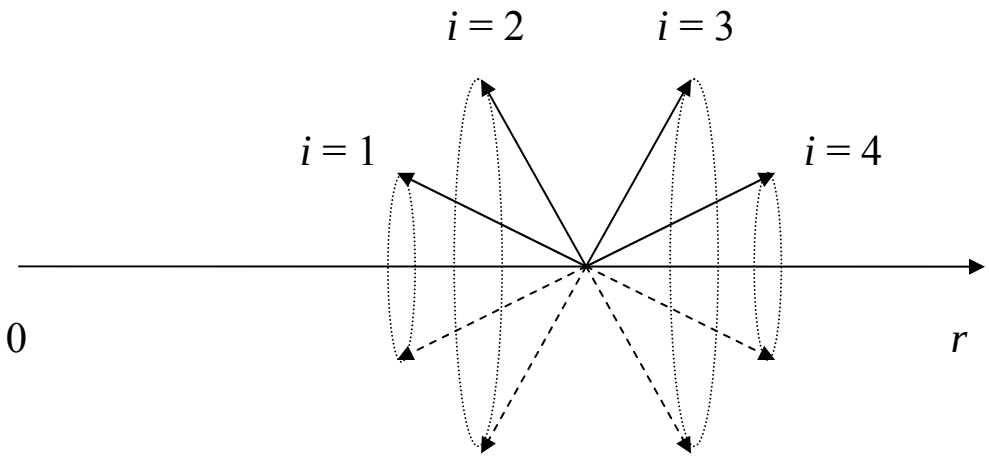

Figure 3.2: A typical diagram of discrete ordinates for 4 ordinates.

In order to solve Equation (3.36) we have different approaches. The traditional one is the iterative method, in which Equation (3.36) is rewritten for each ordinate at each grid point separately, and at any time all the intensities are updated repeatedly until the intensity converges. The convergence criterion is for the integrated intensity error

between iterations to be below the prescribed error bar. Equations (3.39) – (3.46) show an example of iteration equations for 4 ordinates,

for $i = 1,\ \mu_i < 0$ (inwards)

for j=jj, $$I_{jj,1} = I_{jj,b} \text{ (outer boundary)} \tag{3.41}$$

for j<jj, $$I_{j,1} = \frac{\left(\frac{\kappa_j \left(r_{j+1} - r_j \right)}{\mu_1} I_{j,b} - I_{j+1,1} - \frac{\alpha_{3/2} \left(r_{j+1} - r_j \right)}{2 r_j \omega_1' \mu_1} I_{j,2} \right)}{\left(\frac{r_{j+1}}{r_j} - 2 + \frac{\kappa_j \left(r_{j+1} - r_j \right)}{\mu_1} \right)} \tag{3.42}$$

for i =2, $\mu_i < 0$ (inwards)

for j=jj, $$I_{jj,2} = I_{jj,b} \text{ (outer boundary)} \tag{3.43}$$

for j<jj, $$I_{j,2} = \frac{\left(\frac{\kappa_j \left(r_{j+1} - r_j \right)}{\mu_2} I_{j,b} + \frac{\alpha_{3/2} \left(r_{j+1} - r_j \right)}{2 r_j \omega_2' \mu_2} I_{j,1} - I_{j+1,2} - \frac{\alpha_{5/2} \left(r_{j+1} - r_j \right)}{2 r_j \omega_2' \mu_2} I_{j,3} \right)}{\left(\frac{r_{j+1}}{r_j} - 2 + \frac{\kappa_j \left(r_{j+1} - r_j \right)}{\mu_2} \right)} \tag{3.44}$$

for $i = 3,\ \mu_i > 0$ (outwards)

for j=1, $$I_{1,3} = I_{1,b} \text{ (inner boundary)} \tag{3.45}$$

for j>1, $$I_{j,3} = \frac{\left(\frac{\kappa_j \left(r_j - r_{j-1} \right)}{\mu_3} I_{j,b} + \frac{\alpha_{5/2} \left(r_j - r_{j-1} \right)}{2 r_j \omega_3' \mu_3} I_{j,2} + I_{j-1,3} - \frac{\alpha_{7/2} \left(r_j - r_{j-1} \right)}{2 r_j \omega_3' \mu_3} I_{j,4} \right)}{\left(2 - \frac{r_{j-1}}{r_j} + \frac{\kappa_j \left(r_j - r_{j-1} \right)}{\mu_3} \right)} \tag{3.46}$$

for $i = 4,\ \mu_i > 0$ (outwards)

for j=1, $$I_{1,4} = I_{1,b} \text{ (inner boundary)} \tag{3.47}$$

for j>1, $$I_{j,4} = \frac{\left(\frac{\kappa_j \left(r_j - r_{j-1} \right)}{\mu_4} I_{j,b} + \frac{\alpha_{7/2} \left(r_j - r_{j-1} \right)}{2 r_j \omega_4' \mu_4} I_{j,3} + I_{j-1,4} \right)}{\left(2 - \frac{r_{j-1}}{r_j} + \frac{\kappa_j \left(r_j - r_{j-1} \right)}{\mu_4} \right)} \tag{3.48}$$

where j represents local grid ID, jj means total grid number, i represents local ordinate ID, and I_b stands for black body radiation intensity.

Figure 3.3 illustrates the implementation of the iterative method in order to solve Equation (3.36) for 4 ordinates.

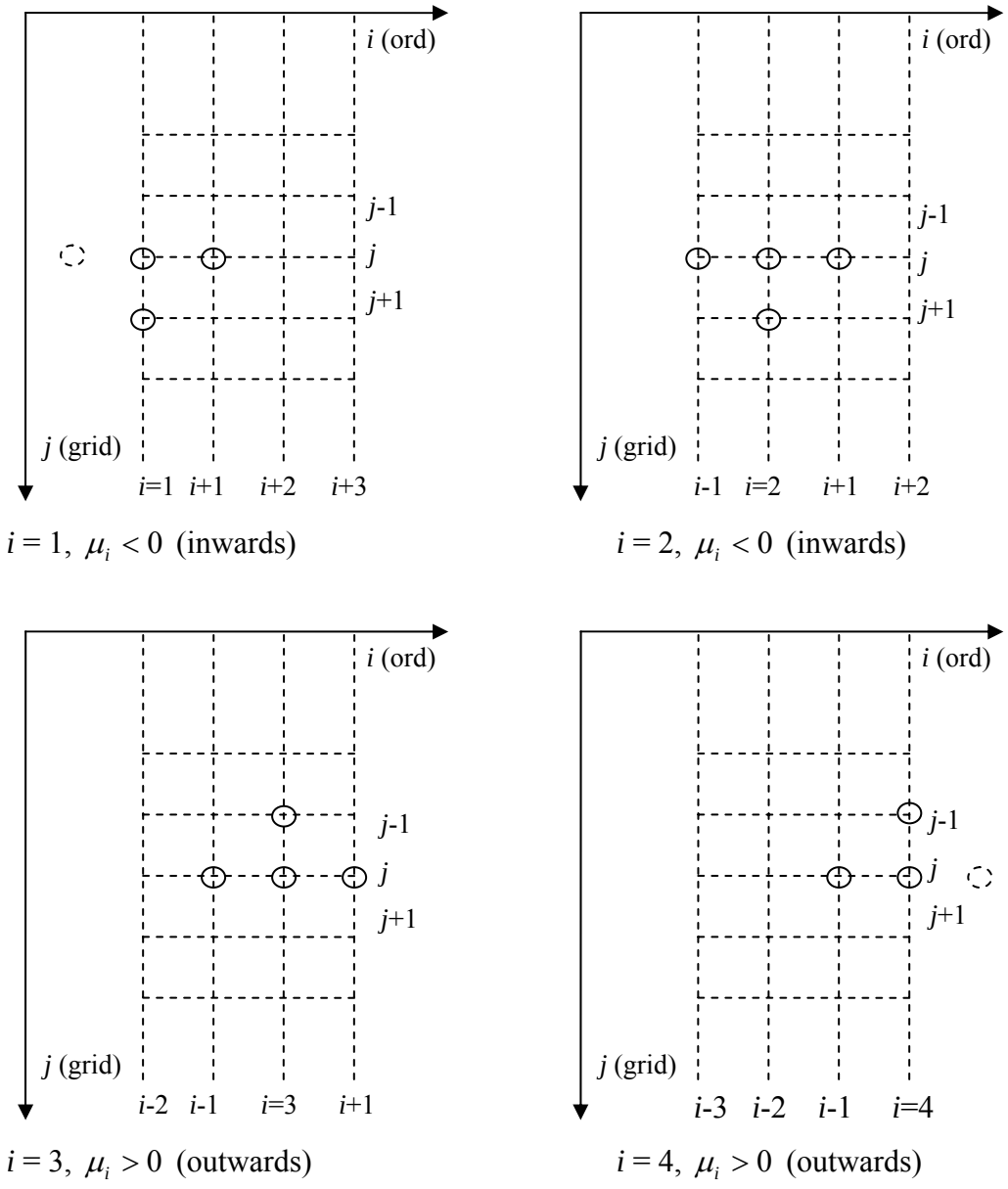

Figure 3.3: A typical diagram for solving RTE for 4 ordinates.

Although easy to understand and implement, the iterative method can easily run into convergence difficulty and thus might be tremendously time consuming in many

circumstances. Because of this, an alternative approximate method (Tsai *et al.* 1989) was introduced to solve Equation (3.36).

In Tsai's method, instead of solving Equation (3.36) an alternative equivalent equation is solved as given below,

$$\frac{\mu_i}{r^2}\frac{\partial}{\partial r}\left(r^2 I_i\right)+\frac{\alpha_{i+\frac{1}{2}} I_{i+\frac{1}{2}}-\alpha_{i-\frac{1}{2}} I_{i-\frac{1}{2}}}{r\omega_i}+\kappa\left(I_i-I_b\right)=0, \tag{3.49}$$

where geometrical coefficients α also satisfy Equations (3.37) and (3.38).

Multiplying Equation (3.49) by $4\pi r^2 dr$ and integrate it over the domain from $r=r_j$ to $r=r_{j+1}$, we have,

$$\mu_i\left(A_{j+1}I_{i,j+1}-A_j I_{i,j}\right)+\left(A_{j+1}-A_j\right)\frac{\alpha_{i+\frac{1}{2}} I^0_{i+\frac{1}{2}}-\alpha_{i-\frac{1}{2}} I^0_{i-\frac{1}{2}}}{2\omega_i}+\kappa^0 V^0\left(I_i^0-I_b^0\right)=0 \tag{3.50}$$

where

$$A_j=4\pi r_j^2 \tag{3.51}$$

$$V^0=4\pi\left(r_{j+1}^3-r_j^3\right)/3, \tag{3.52}$$

and the quantities with a superscript 0 denote values at the node center, i.e., (j+1/2).

The intensity at the cell center I_i^0 is related to the intensities $I_{i,j}$ and $I_{i,j+1}$ at the cell boundaries *j* and (*j*+1) by

$$I_i^0=\left(I_{i,j}+I_{i,j+1}\right)/2, \tag{3.53}$$

and I_i^0 is also related to the intensities $I^0_{i-1/2}$ and $I^0_{i+1/2}$ at the angular edges (*i*-1/2) and (*i*+1/2) by,

$$I_i^0=\left(I^0_{i-1/2}+I^0_{i+1/2}\right)/2. \tag{3.54}$$

The computation in Equation (3.49) can be performed from $r=r_2$ to $r=r_1$ (inwards) for $\mu_i<0$ and from $r=r_1$ to $r=r_2$ (outwards) for $\mu_i>0$ as follows.

For $\mu_i<0$ (inward calculations)

Eliminating $I_{i,j}$ and $I^0_{i+1/2}$ from Equation (3.49) by utilizing Equations (3.53) and (3.54), we have

$$I_i^0 = \frac{-\mu_i A I_{i,j+1} + \gamma_i^0 I_{i-1/2}^0 + \kappa^0 V^0 I_b^0}{-\mu_i A + \gamma_i^0 + \kappa^0 V^0}, \tag{3.55}$$

where

$$A = A_j + A_{j+1}, \tag{3.56}$$

$$\gamma_i^0 = \frac{\left(\alpha_{i-1/2} + \alpha_{i+1/2}\right)\left(A_{j+1} - A_j\right)}{2\omega_i}. \tag{3.57}$$

For $\mu_i > 0$ (outward calculations)

Eliminating $I_{i,j+1}$ and $I_{i+1/2}^0$ from Equation (3.49) by utilizing Equations (3.53) and (3.54), we have

$$I_i^0 = \frac{\mu_i A I_{i,j} + \gamma_i^0 I_{i-1/2}^0 + \kappa^0 V^0 I_b^0}{\mu_i A + \gamma_i^0 + \kappa^0 V^0}, \tag{3.58}$$

where A and γ_i^0 have been defined by Equations (3.56) and (3.57).

Combining Equations (3.55), (3.58), and (3.53) along with corresponding boundary conditions we can calculate radiation intensities on all the grids and all the ordinates.

Since iteration is not needed in this method, radiation intensities can be solved much more efficiently with convergence difficulty being avoided, and computational accuracy was also validated with the comparison to the iterative method solution, so this method is always used in the following chapters.

Chapter 4 Validation of the Model

Prior to extensive parametric studies, we first validate the computational model described in previous chapters against experimental data for some typical parameter conditions. The main observables in the experiments are the flame radius and temperature monitored in time, so the comparison of the simulation results will be made on these quantities. One of the important objectives of the model validation is to compare the various levels of the radiation models considered in Chapter 3, thereby identifying an adequate model to be used in the subsequent parametric studies. In order to enable the model validation an appropriate approach is needed to ignite the flame which constitutes an important part of the transient simulation.

4.1. Comparison of Initialization Methods

In the experiment (Chernovsky *et al*. 2006), the flame was ignited by a heating wire which releases a given amount of energy in the vicinity of the burner surface within a short period of time, when the local temperature is raised to a sufficiently high level to activate the chemical reaction. In order to mimic the ignition process for all different cases in numerical simulation we have various options, and in this study three different approaches have been introduced and compared, each corresponding to a different initial condition discussed in Chapter 2.

First, an external heat source in a spatially Gaussian distribution was imposed such that the peak value of the distribution attenuates gradually with time. A uniform initial temperature distribution was imposed and the temperature rises in time as a result of the heat source. Although this approach appears to resemble the experimental ignition condition, it required too many parameters to be adjusted in order to successfully ignite flames for a wide range of conditions. Consequently, it was decided that this approach is not adequate for consistent validation against experiment.

Second, an initial temperature profile representing a local heating of gases by the wire was imposed with some success. To achieve successful ignition, however, a careful choice of the initial temperature as well as species concentration profiles are needed. For example, fuel and oxygen profiles need to have a sufficient level of overlap across the peak temperature location. Even with these adjustments, we have experienced a number of unsuccessful cases in which the flame either does not ignite or bursts out abruptly causing a numerical difficulty. For some cases, it was necessary to add some amount of radicals in the initial species profiles, which introduces even more adjustable parameters. Therefore, this approach was also deemed too *ad hoc* and was not adopted.

In the last approach, the flame ignition process was divided into two steps. In the first step a steady diffusion flame was calculated within a confined region near the burner surface, and then it was mapped onto the computational domain for the transient calculation. This is consistent with the approach adopted by Tse and coworkers (2001). In the experimental work (Atreya *et al.* 2001, Chernovsky *et al.* 2007), it was found that the initial flame size upon spark ignition was insensitive to the different parametric conditions despite their wide differences in the subsequent flame growth behavior. The adopted initiation method appeared to reproduce this behavior adequately. In all the different cases to be compared with experimental data, the confined domain size for the steady calculation was determined to be 0.6 cm, which allowed the steady flames established with a size close to that of the initial flames observed in experiments. Although there are more than one parameters associated with the steady calculation, the sensitivity to the parameters vanishes through the iterative solution process. Therefore, as far as the transient calculation is concerned, the only relevant parameter is the size of the confined domain which determines the initial steady flame size. Since all the computational cases to be compared with experimental data use the same parameter (0.6 cm), the model validation can be conducted in a more systematic and consistent manner.

Therefore, the last initiation method was adopted throughout the study. Computational tests showed that when the confined domain size was increased from 0.6 cm to 1.0 cm the overall computational efficiency was increased. Computational cases in Chapter 5 and 6 are artificial cases without counterpart experimental cases to compare,

and thus we chose domain size of 1.0 cm for all the cases in Chapter 5 and 6 unless otherwise mentioned.

The confined region is so small that the steady flame is very thin and radiation heat loss from the flame zone is negligible, so radiation model is turned off for steady calculation.

4.2. Validation on Flame Radius

In the experiment (Chernovsky *et al*. 2006), the flame growth was recorded by a CCD camera at a frequency of 30 frame/s. The flame radius was measured by averaging two pairs of orthogonal diameter based on the luminous zone. In the simulation, the flame radius was determined by the location of the maximum temperature in the computational domain.

Various radiation models were tested in the simulations. In terms of the radiation property models, the gray gas, wide band, and narrow band models were employed and the resulting flame growth behavior was compared. We chose a typical experimental case in which 100% C_2H_4 is supplied through the porous sphere burner at a flow rate of 6 ml/s, while the ambient gases consist of 21% O_2, 17% N_2, 21.3% CO_2, and 40.7% He.

Figure 4.1 shows the comparison of the flame radius growth between the experimental data and simulation results with different radiation models, including the adiabatic condition without incorporating any radiative models. For all comparisons, the time axis was synchronized to be at 0.3 s when the flame radius becomes 1.2 cm. As discussed in Chapter 2, the initialization of the calculation was implemented in a consistent manner such that uncertainties in the time synchronization were minimized. First, the adiabatic condition (line a) yields a flame radius much larger than the experimental data, which is attributed to the high flame temperature (to be discussed in Section 4.2) due to the lack of radiative heat losses. The quantitative analysis shows that the adiabatic assumption results in an average relative error of 10.5% in flame radius compared to the experimental data. Therefore, it is evident that the gas radiation effect cannot be neglected in the present microgravity combustion study, in which the flame thickness is much larger than that in Earth's gravity conditions, resulting in a large volume of high temperature gases that participate in radiative heat transfer.

When the gray gas and optically thin model (line b) is applied, the flame radius increases at a slower rate and then drops suddenly at approximately 0.65 s, which implies a flame extinction. The subsequent increase in the flame radius curve after the drop only represents the growth of the hot product gas pocket due to diffusive and convective transport, and should not be considered behavior of an intensely burning flame. The early extinction behavior in this case is attributed to the excessive radiative heat loss inherent in the optically thin model which does not account for the reabsorption by the product gases. The quantitative analysis shows that this case has an average relative error of 19.1% in flame radius compared to the experimental data, which shows that the prediction is unacceptable.

Next, employing the wide band model (line c) yields the flame radius behavior much closer to the experimental data. However, the flame extinction occurs earlier at approximately 1.5 s, again suggesting that the radiative heat losses are overestimated. Although this case only has an average relative error of 8.7% in flame radius compared to the experimental data, the early extinction shows that the wide band model should not be selected for application in our study.

Finally, the best agreement is obtained when the statistical narrow band model (line d) is applied. Although there are some discrepancies in the flame radius growth, the overall trend and the absence of extinction up to 2.0 s best reproduce the experimental measurement. Computational results in this model only have an average relative error of 5.9% in flame radius compared to the experimental data, which confirms the best accuracy of the statistical narrow band model.

In conducting the above comparisons, except for some uncertainties in the initial flame ignition phase (which was minimized by the adopted initiation method and time synchronization), the calculations were carefully undertaken to match the experimental conditions. Therefore, the results shown in Figure 4.1 demonstrate the importance of radiation models on accurate prediction of the microgravity flame behavior. Among the various radiation models considered, the statistical narrow band model with a detailed spectral resolution capability appears to be a necessary and adequate for subsequent parametric studies. The line-by-line radiation model can offer an even higher level of spectral resolution, but it is computationally too expensive to be employed in the present

study. Therefore, the statistical narrow band model is adopted for the rest of the parametric studies.

4.3. Validation on Flame Temperature

From the purpose of validation against the experimental data, flame radius comparison alone does not seem sufficient, and therefore further efforts were made to compare flame temperature history information between the experimental data and the computational results.

The experiment of Chernovsky and coworkers (2006, 2007) is especially valuable for this purpose since this was the first microgravity experiment with spatially-resolved temperature measurements by the use of thermocouples placed at various positions from the burner surface. The measured temperature data was post-processed with corrections for conductive and radiative heat transfer as well as transient response of the thermocouple bead. The temperature signal was sampled every 0.02 seconds and the frequency was partly determined by the thermal response characteristics of thermocouples in experiment. The transient temperature data at various locations collectively provide very detailed information of the flame, and thus serves as a useful means to validate the accuracy of the numerical model.

A total of eight thermocouples were placed in the experiment. However, some of them were located far away from flame zone and thus did not provide very significant information. Consequently, only the temperature information from the four thermocouples closest to the burner surface was used for comparison. Figure 4.2 shows transient experimental temperature profiles at four different locations, whose distance from the burner center is 1.45, 1.75, 2.15, and 2.70 cm, respectively. In the simulation, the transient temperature behavior at the same spatial locations was computed for direct comparison with the thermocouple measurements.

Figure 4.3 shows the simulated transient temperature history at the same four locations as shown in Figure 4.2, under the adiabatic condition without any radiation model. Although the initial peak temperature in this simulation is close to the experimental data, the peak temperature continues to increase in time due to the absence of radiative heat loss. The quantitative analysis shows that computational results with

adiabatic assumption have an average relative error of 38.6% in temperature at the above four locations compared to the experimental data. It is evident that the overestimated flame temperature is responsible for the rapid flame growth prediction shown in Figure 4.1.

Figure 4.4 shows the simulated transient temperature history at the same four locations using the gray gas and optically thin radiation model. The flame extinction behavior at 0.65 s is clearly observed. This further confirms that no flame exists beyond this extinction point and the flame radius growth shown by line b in Figure 4.1 is indeed the growth of the product gases at lower temperatures. The average relative error between computational results in this model and the experimental data is 63.3%, which quantitatively illustrates the inaccuracy of this model.

Figure 4.5 shows the simulated transient simulation temperature profiles at the same four locations, using the narrow band radiation model. It is seen that flame temperature decreases gradually with time when flame continues to grow. The behavior is most consistent to the experimental data shown in Figure 4.2. To quantitatively assess the accuracy of the modeling results, in Figure 4.6 the experimental and simulation results are overlaid. The discrepancies at early times are attributed to the inevitable uncertainties in reproducing the experimental initialization method in the numerical model. Nevertheless, the agreement between the experiment and simulation improves at later times and at the location further away from the burner surface, which is shown by the envelope line coving both experimental data and simulation results very well. Computational results in this model have a very low average relative error of 5.7% in temperature compared to the experimental data, and this demonstrates that the narrow band radiation model reproduces the experimental behavior at reasonable accuracy after the effect of the ignition method disappears.

Based on the validation results for various radiation models, we conclude that the narrow band model is necessary to provide realistic flame behavior, and is adopted throughout the remainder of the studies.

4.4. Accuracy of the Discrete Ordinate Method

4.4.1. Number of ordinates

Thus far, different radiation property models have been compared in terms of their predictable capabilities. The other important component of the radiation model is the solver for the RTE equations. Although DOM was adopted as a reasonable approach for the current finite-difference model, its computational accuracy must be tested. The main numerical parameter for DOM that determines accuracy is the number of ordinates, and hence we have tested various numbers of ordinates for the accuracy and computational efficiency.

From the computational results with different numbers of ordinates (4, 6, and 8), it is confirmed that full computational convergence is achieved for the number of ordinates at 4 and above. Figure 4.7 compares the detailed radiative intensity profiles at the wave band of 2350 cm^{-1} for various numbers of ordinates, the intensity profiles correspond to the transient solution at 2.0 second for case 3F-3A. When the number of ordinates increases from 4 to 6, the radiation intensity solution for both inward and outward ordinates has large differences. When we increase the number of ordinates to 8, however, the radiation intensity solution shows little differences compared to that with 6 ordinates. Compared to the case with 4 ordinates, the relative increase in the computational cost was approximately 6% with 6 ordinates and 12% with 8 ordinates. Since the computational overhead was not significant for the present one-dimensional simulations, the number of ordinates of 8 is chosen for all calculations.

4.4.2. Radiation sub-cycling

The radiation model is coupled to the rest of the system of equations, such that it should be updated each time step to ensure accurate evaluation of radiative heat transfer terms in the energy equation. For transient calculations, the solver (DASPK) has variable time step, and the typical time step is on the order of 10^{-5} seconds. Therefore, if the radiation model was updated each time step the corresponding computational overhead would be significantly high. For example, if the SNB radiation property model and DOM model are updated at each time step, the additional computational load involves the calculation

of the absorption coefficients for 367 wavebands at each grid point according to the local pressure, temperature, and species composition data, along with the radiation intensity for each waveband at each ordinate and each grid point. Although the approximate method (Tsai *et al.* 1989) for solving radiative transfer equations eliminates the need for iterative technique for the RTE solver, the overall overhead for the radiation intensity calculation is substantial.

Considering that the radiation information actually varies at slower time scales, a common practice to reduce the computational overhead is to update the radiation model at a larger number of time steps – referred to as sub-cycling. Since an excessive level of sub-cycling may affect the computational accuracy, it is important to conduct test simulations to identify an appropriate level of sub-cycling for optimal computational accuracy and efficiency. Our test simulations revealed that, for the parametric conditions under study, a satisfactory level of accuracy is achieved as long as the sub-cycling period does not exceed 10 milliseconds. This assessment was based on the accuracy of the temperature profile, which is the most important solution variable that determines the overall flame behavior. The overall computational efficiency was improved by approximately a factor of five when the 1 millisecond sub-cycling was applied and a factor of ten when the 10 milliseconds sub-cycling was applied.

4.4.3. Coupling of SNB model and DOM model

Since we have decided to choose SNB model for radiation property assumption and DOM model for radiative transfer description for the future parametric study, further discussion is needed for better understanding.

Equation (3.24) is the general spectral radiative transfer equation for absorbing, emitting, and anisotropically scattering media,

$$\hat{\mathrm{s}} \cdot \nabla I_{\eta} = \kappa_{\eta} I_{\mathrm{b}\eta} - (\kappa_{\eta} + \sigma_{\mathrm{s}\eta}) I_{\eta} + \frac{\sigma_{s\eta}}{4\pi} \int_{4\pi} I_{\eta}(\hat{\mathbf{s}}_i) \Phi_{\eta}(\hat{\mathbf{s}}_i, \hat{\mathbf{s}}) \, \mathrm{d}\Omega_i \,. \tag{3.24}$$

In this study scattering is always neglected, so Equation (3.24) can be rewritten for an absorbing and emitting medium in the wavenumber-averaged form as (Kim *et al.* 1991, De Miranda *et al.* 1996, Liu *et al.* 1998),

$$\frac{\partial \bar{I}_\eta(s,\Omega)}{\partial s} + \overline{\kappa_\eta I_\eta(s,\Omega)} = \bar{\kappa}_\eta(s)\bar{I}_{b\eta}(s), \tag{4.1}$$

where the terms under overbar are averaged values over a narrow band $\Delta\eta$ centered at η.

We notice that the term $\overline{\kappa_\eta I_\eta(s,\Omega)}$ has one complete overbar; however, the overbar is broken for term $\bar{\kappa}_\eta(s)\bar{I}_{b\eta}(s)$. This is because blackbody radiation intensity $I_{b\eta}$ is a determined smooth function of wavenumber and is independent of absorption coefficient κ_η, so it can be taken out as a constant; however, since narrow band model itself does not readily assume constant radiation property and radiation intensity across each single narrow band, and theoretically absorption coefficient κ_η spectral function and radiation intensity I_η spectral function are correlated; therefore, these two terms can not readily be taken out of the overbar.

Assuming boundary spectral radiation intensity $I_{w\eta}(s_w,\Omega)$ high-emissivity wall condition, we have

$$\begin{aligned}\frac{\partial \bar{I}_\eta(s,\Omega)}{\partial s} &= \left(\frac{\partial \overline{\tau_\eta(s'\to s)}}{\partial s'}\right)_{s'=s} \bar{I}_{b\eta}(s) \\ &+ \bar{I}_{w\eta}(s_w,\Omega)\frac{\partial}{\partial s}\left[\bar{\tau}_\eta(s_w\to s)\right] + \int_{s_w}^{s}\frac{\partial}{\partial s}\left(\frac{\partial \overline{\tau_\eta(s'\to s)}}{\partial s'}\right)\bar{I}_{b\eta}(s')ds'\end{aligned}, \tag{4.2}$$

The discretized form of Equation (4.2) along a line of sight is (Kim *et al.* 1991)

$$\bar{I}_{\eta,i,j+1} = \bar{I}_{\eta,i,j} + \left(1-\bar{\tau}_{\eta,i,j\to j+1}\right)\bar{I}_{b\eta,j+1/2} + \bar{C}_{\eta,i,j+1/2}, \tag{4.3}$$

where

$$\begin{aligned}\bar{C}_{\eta,i,j+1/2} &= \bar{I}_{w\eta,i,1}\left(\bar{\tau}_{\eta,i,1\to j+1} - \bar{\tau}_{\eta,i,1\to j}\right) \\ &+ \sum_{k=1}^{j-1}\left\{\left[\left(\bar{\tau}_{\eta,i,k+1\to j+1} - \bar{\tau}_{\eta,i,k+1\to j}\right) - \left(\bar{\tau}_{\eta,i,k\to j+1} - \bar{\tau}_{\eta,i,k\to j}\right)\right]\bar{I}_{b\eta,k+1/2}\right\}\end{aligned}, \tag{4.4}$$

where spatial discretization index $j = 1$ corresponds to the wall.

Equations (4.3) and (4.4) show that the calculation of radiation intensity at any grid point depends on information of all grid points between the wall and this grid point, which makes the computing effort extremely high. When grid number increases the computing effort increases exponentially, which makes it almost impractical to solve the

detailed radiation information along with transient complex system involving flows and chemical reactions.

In practical application, we have to make some assumptions to make it feasible to solve radiation intensity, and one important assumption is noncorrelated narrow-band assumption from which we have

$$\bar{\tau}_{\eta,i,1\to j} = \prod_{k=1}^{j-1} \bar{\tau}_{\eta,i,k\to k+1} \ . \tag{4.5}$$

As a result, Equation (4.3) changes into

$$\bar{I}_{\eta,i,j+1} = \bar{I}_{\eta,i,j}\,\bar{\tau}_{\eta,i,j\to j+1} + \left(1-\bar{\tau}_{\eta,i,j\to j+1}\right)\bar{I}_{b\eta,j+1/2}\,, \tag{4.6}$$

which only depends on local radiation information and extremely reduces the computing effort.

We notice that, Equation (4.6) is in the same form as the radiative transfer equation for spectral or gray radiation intensity, which means as long as we assume radiation property to be independent of the wavenumber within each narrow band, Equation (4.6) is valid. For SNB model, the narrow band width of 25 cm^{-1} is sufficiently small so that radiation property can be assumed constant or "gray", and thus application of Equation (4.6) will not cause notable error.

Actually in Chapter 3, equations starting from Equation (3.24) are all based on the gray-band assumption, but we did not mention clearly this assumption at that point. Although those equations seem "obviously" valid, they are not correct without the gray-band assumption which is not readily stated in narrow band model. In conclusion, the discussion in this section will not affect the application of the equations in Chapter 3; however, it helps us to better understand the underlining models.

Another issue to be mentioned here is that, the gray-band assumption here is different from the gray gas model in Chapter 3 although both have the keyword "gray". In the former case, it is assumed gray for each narrow band; however, in the latter case the entire spectral domain is assumed gray.

4.4.4. Negative radiation intensity

When DOM model is applied for solving radiative transfer equation, it is not uncommon to find negative values in radiation intensity results. Although the physically unrealistic

negative intensities are not desired, it is very difficult to completely avoid it unless prohibitive fine meshes are used, and the same observation has also been reported by other researchers (Fiterman *et al.* 1999, Liu *et al.* 1996). A conventional fix-up procedure is to set negative intensities to zero whenever they are encountered, and the error is sufficient small to be acceptable as reported by Liu and coworkers (1996) to be up to 4%. In our work, the odds of negative radiation intensity are on the order of 0.1%, and consequently the error associated with this fix-up procedure can be neglected.

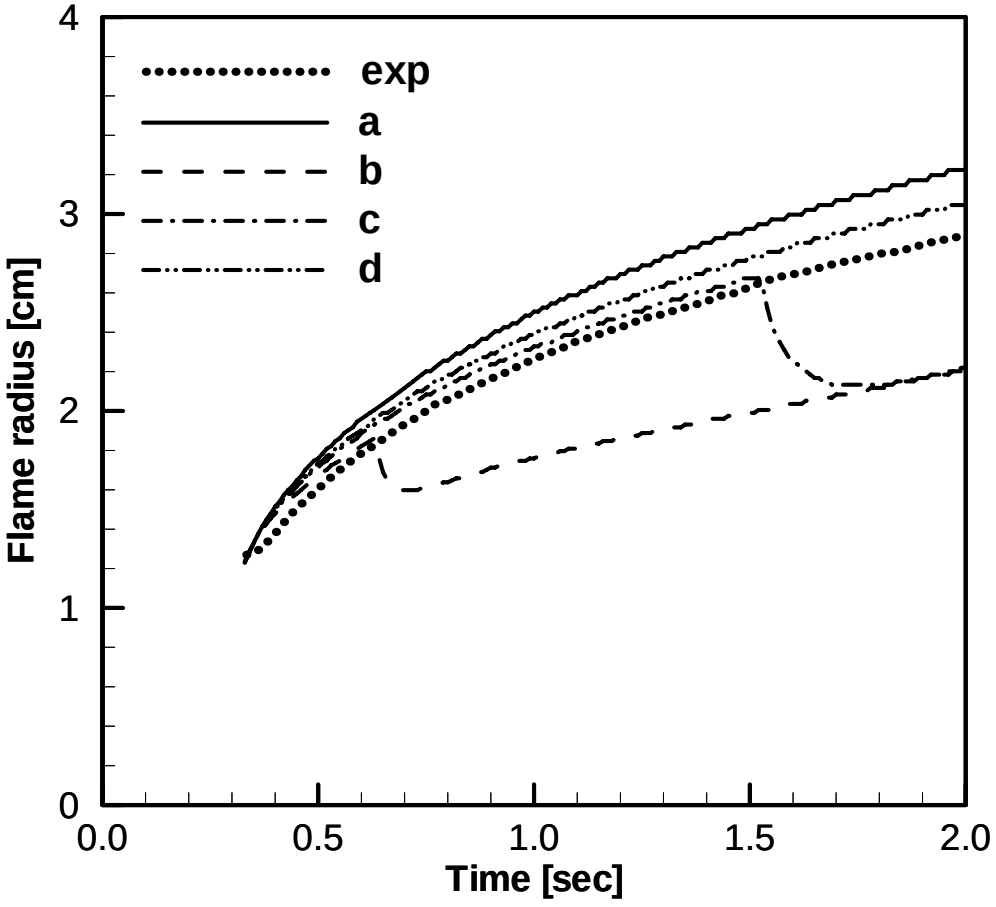

Figure 4.1: Flame radius comparison between experimental data and simulation results with various radiation models.

a: adiabatic; b: gray gas + optically thin model; c: wide band model; d: statistical narrow band model.

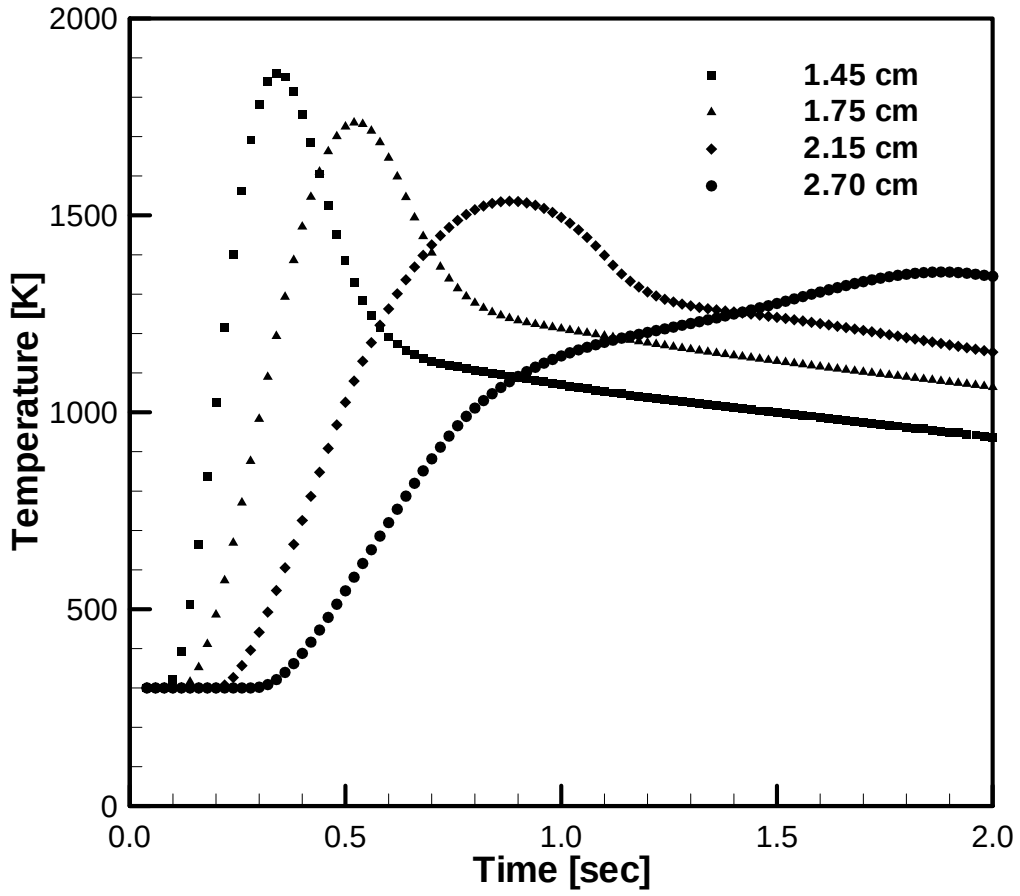

Figure 4.2: Transient temperature history measured at four locations: 1.45 cm, 1.75 cm, 2.15 cm, and 2.70 cm.

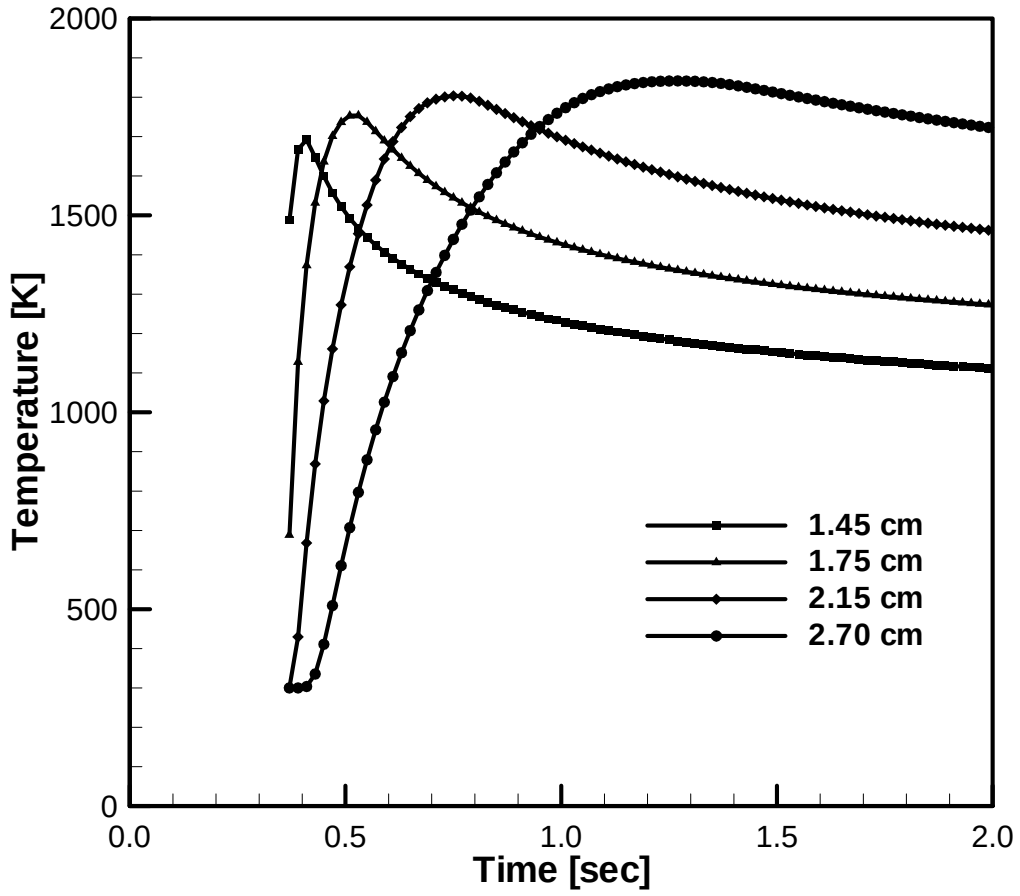

Figure 4.3: Simulated transient temperature history at the same four locations as shown in Figure 4.2, under the adiabatic condition.

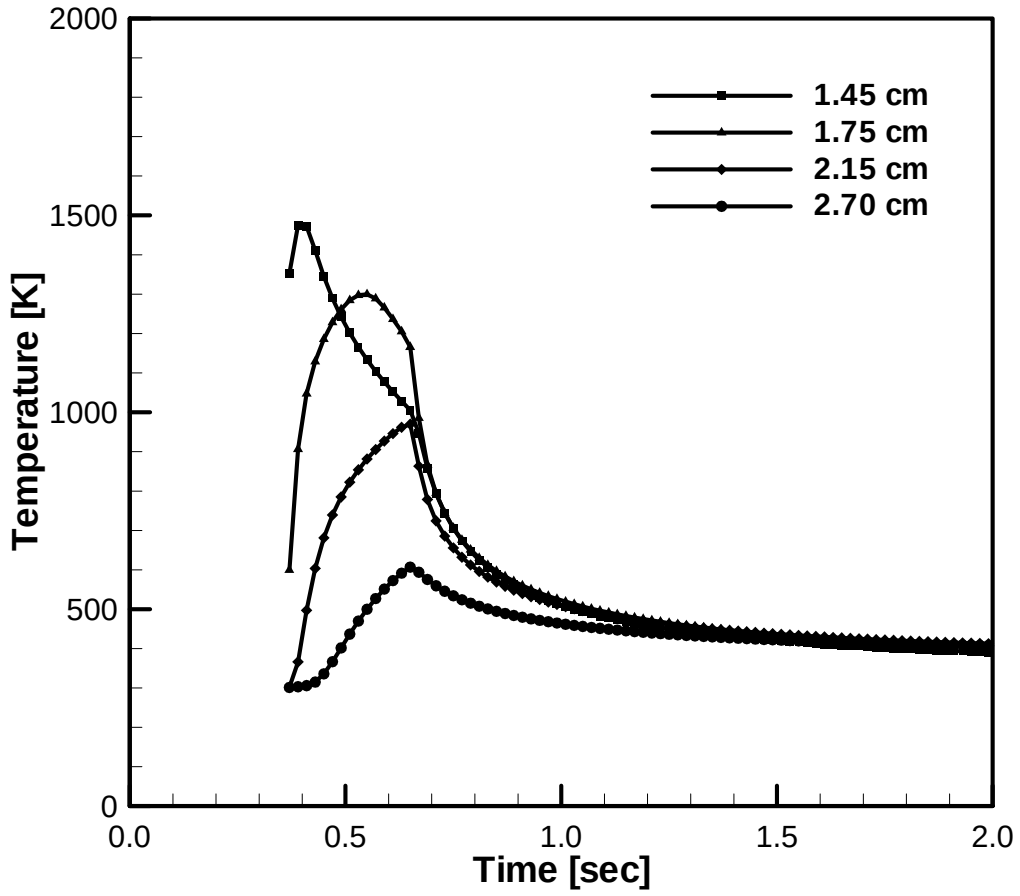

Figure 4.4: Simulated transient temperature history at the same four locations as shown in Figure 4.2, using the gray gas and optically thin radiation models.

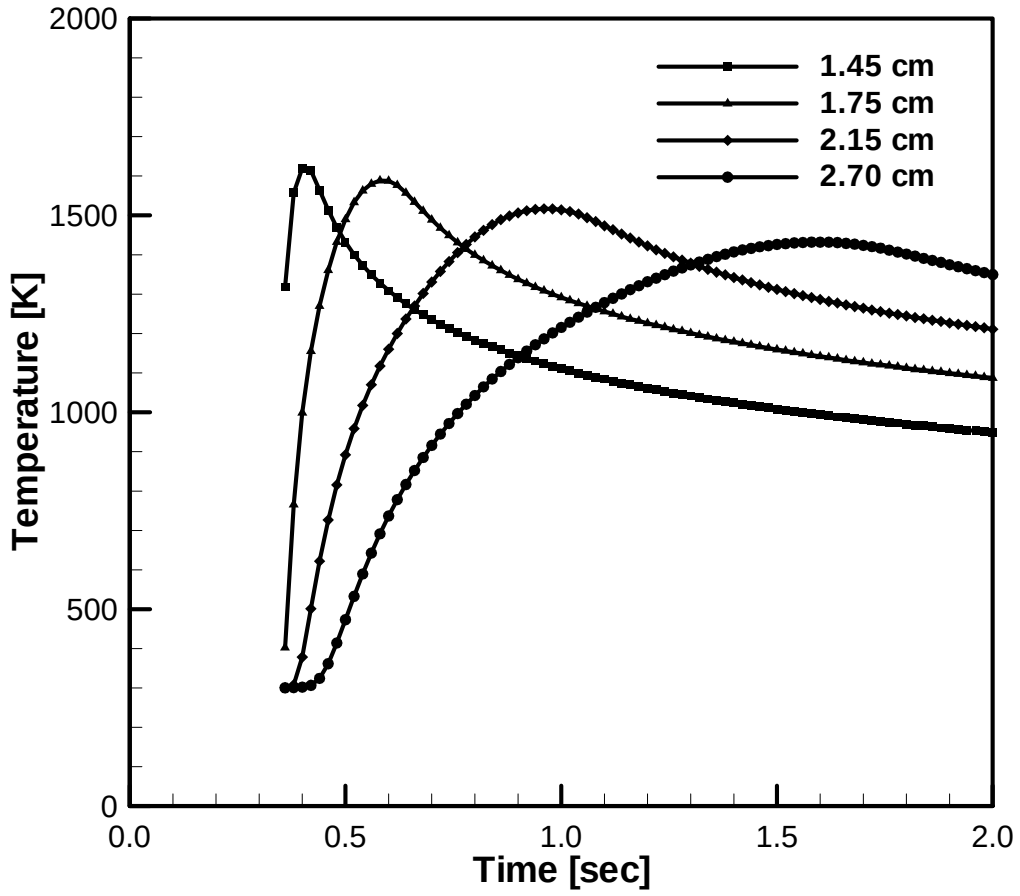

Figure 4.5: Simulated transient temperature history at the same four locations as shown in Figure 4.2, using the narrow band radiation model.

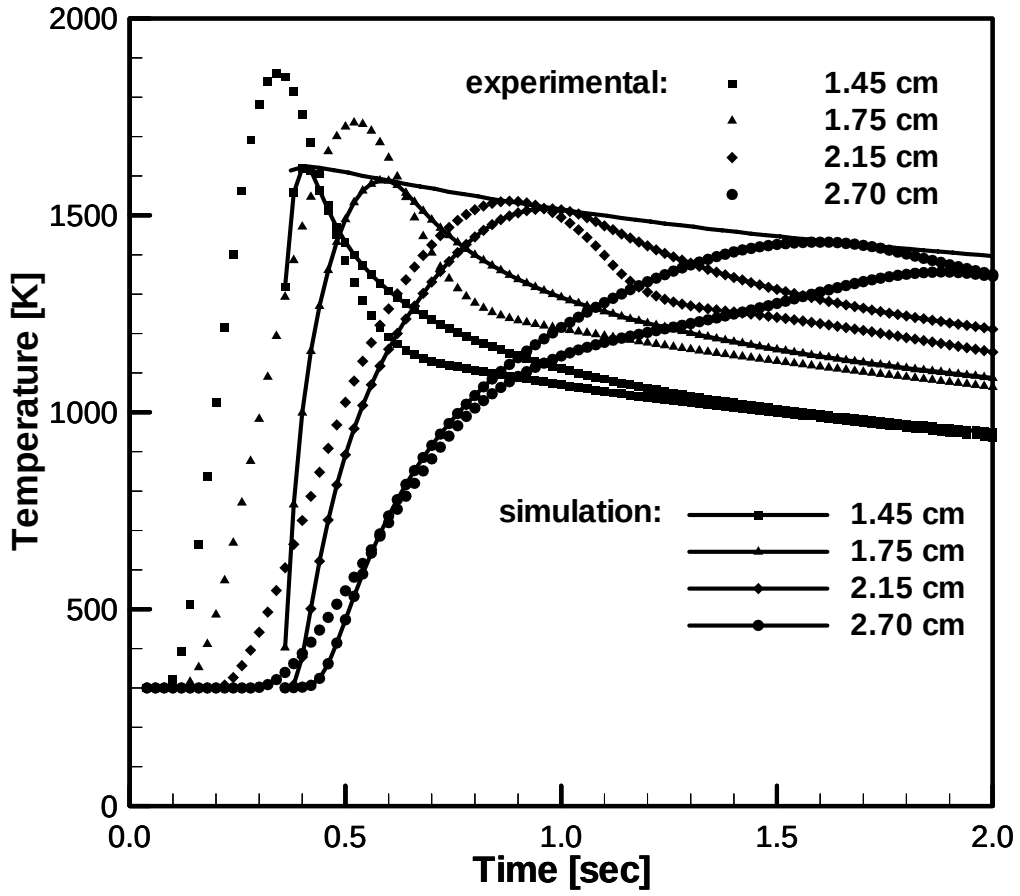

Figure 4.6: Comparison of temperature history between experimental and simulation results by overlaying Figures 4.2 and 4.5.

symbols: experiment; symbol lines: simulation; solid line shows the envelope of the peak temperature representing the flame temperature history.

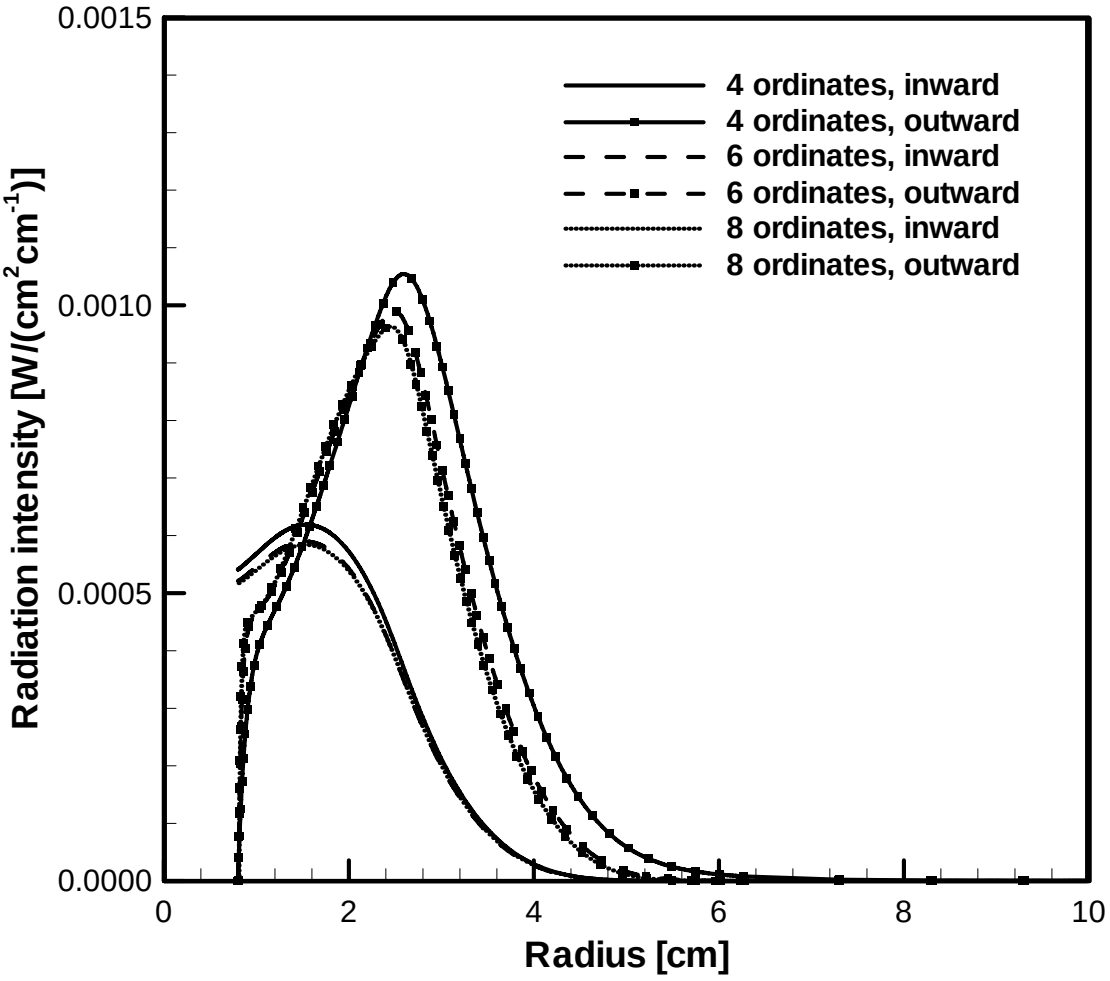

Figure 4.7: Comparison of radiation intensity solution between different ordinate options.

Chapter 5 Effects of Fuel- and Oxidizer-Side Dilution

One of the key issues in the present study is to investigate the effects of diluent gases on the flame behavior, especially in terms of radiation-induced extinction. Therefore, the control of fuel- and oxidizer-side composition is varied independently by adding a certain amount of diluents on the fuel side or the oxidizer side or both sides. The diluents used are N_2, CO_2, and He. In this chapter we will investigate the relative impact of diluents added to either fuel or oxidizer side.

To quantitatively study the effect of dilution on fuel side and oxidizer side individually, a group of cases were designed with fuel- and oxidizer-side compositions shown in Table 5.1.

Table 5.1: Case matrix for fuel- and oxidizer-side dilution comparison

Case number	Fuel mole fraction (%)				Oxidizer mole fraction (%)				T_{adb} (K)
	C_2H_4	N_2	CO_2	He	O_2	N_2	CO_2	He	2508.1
3F-3A	30	70	0	0	30	70	0	0	2361.6
3F7C-3A	30	0	70	0	30	70	0	0	2563.9
3F7H-3A	30	0	0	70	30	70	0	0	2506.9
3F7M-3A	30	0	17	53	30	70	0	0	2160.5
3F-3A7C	30	70	0	0	30	0	70	0	2673.6
3F-3A7H	30	70	0	0	30	0	0	70	2507.6
3F-3A7M	30	70	0	0	30	0	17	53	2508.1

There are 7 cases in this table, all of which have 30% mole fraction of C_2H_4 on the fuel side and 30% mole fraction of O_2 on the oxidizer side. The volume flow rate is also identical for all the cases at 12 ml/s, so that the same amount of reactants (C_2H_4 and O_2) is provided. The domain size is 1.0 cm for all the cases. The nomenclature for the case numbers are chosen to be self-explanatory; Case 3F-3A is the baseline case where 70%

N_2 is applied as diluent on both sides, case 3F7C-3A, 3F7H-3A, and 3F7M-3A represent that only the fuel-side diluents are changed to 70% CO_2, He, and the mixture of CO_2 and He, respectively. Similarly, Cases 3F-3A7C, 3F-3A7H, and 3F-3A7M represent that the oxidizer-side diluents are replaced by 70% CO_2, He, and their mixture, respectively. Cases 3F7M-3A and 3F-3A7M were chosen so that the adiabatic flame temperature of the homogeneous mixture becomes identical to that in the baseline case, 3F-3A (2508 K).

5.1. Flame Radius and Temperature Behavior

As in Chapter 4, the flame behavior is investigated in terms of flame radius and flame temperature during the transient process. Figures 5.1 and 5.2 show the comparison of the flame radius and temperature behavior for different fuel-side dilution cases (3F-3A, 3F7C-3A, and 3F7H-3A as in Table 5.1). Similarly, Figures 5.3 and 5.4 show the comparison for different oxidizer-side dilution cases (3F-3A, 3F-3A7C, and 3F-3A7H as in Table 5.1).

Comparing Figure 5.1 with 5.3 and Figure 5.2 with 5.4 we find that, with the same level of diluent composition, the oxidizer-side dilution cases show a larger variation in the flame behavior for both flame radius and flame temperature compared with fuel-side dilution cases. This can be explained by the spherical configuration under study. The outer edge of the flame is connected to the environment and thus has the same species concentration condition as the ambient condition; however, species compositions at the burner surface are affected by both fuel-side and oxidizer-side boundary conditions through the flux balance as described in Equation 2.20, thus they do not keep the same values as the far upstream condition. When fuel-side dilution alone is applied, the fuel-lean side species profiles are barely affected because they are closely controlled by the ambient condition which is constant; at the same time, the species profiles on the fuel-lean side help to “stabilize” the species profiles on the fuel-rich side even though the far upstream condition is different for different dilution cases. However, when oxidizer-side dilution alone is applied, on the contrary, the species profiles on the fuel-lean side is directly controlled by the ambient condition which is different for different dilution cases; at the same time, the fuel-rich side species profiles are affected by the fuel-lean side although the far upstream condition is the same for different cases. Figures 5.5 and 5.6

illustrate the transient computational results at 1.0 second for fuel-side and oxidizer-side dilution cases separately, where the profiles of temperature and C_2H_4 as well as O_2 mole fractions are plotted. Comparing these two figures we find that the plots for fuel-side dilution cases are very close to each other, but the oxidizer-side dilution cases have more scattered profiles, which helps to explain the comparison between Figures 5.1~5.4 discussed above.

The observed larger variation of flame radius and temperature behavior among oxidizer-side dilution cases than that among fuel-side dilution cases is in contrast to an earlier experimental study (Chernovsky 2006, Chernovsky *et al*. 2007) in which the flame radius and temperature behavior for some cases was found to be more sensitive to the fuel-side dilution. However, the comparison between fuel-side dilution case variation and oxidizer-side dilution case variation was not consistent throughout the entire experimental data set, such that it was difficult to draw a definite conclusion. We believe that the present computational study provides a more systematic and consistent data set without experimental uncertainties, hence concluding that the oxidizer-side dilution has dominant effects on flame radius and temperature behavior.

To further confirm that the fuel-side dilution has little effect on the flame behavior, we investigate more cases for the fuel-side dilution as listed in Table 5.2, where the amount of the diluent is varied for each choice of diluent. For all the cases, the oxidizer side was set to be air (mixture with 21% O_2 and 79% N_2 in volume); however, note that the domain size for steady calculation was 0.6 cm, and the volume flow rate was 6 ml/s which are different from the cases listed in Table 5.1. Figure 5.7 shows flame radius for the nine cases under consideration, and it is evident that flame radius is more sensitive to the amount of diluent (20% → 40% → 70%) than to the diluent species type variation. At finer scales, it is observed that the effect of different diluents becomes larger as the total amount is increased; the three cases with 20% dilution almost collapse with each other, the three cases with 40% dilution have variations of no more than 0.02 cm at the end of 2.0 second, while for the three 70% dilution cases the variations are as large as 0.11 cm.

Another observation from Figure 5.7 is that an increase on the fuel-side dilution results in a decreased flame radius. As the fuel-side dilution amount increases, the mole fraction of C_2H_4 in the fuel decreases; therefore, the fuel does not need to travel outwards

as far to meet with enough oxygen for stoichiometric combustion, and consequently the flame grows more slowly. This result agrees with the experimental observation by Chernovsky (2006).

Table 5.2: Case matrix for fuel-side dilution comparison

Case number	Fuel mole fraction (%)				Oxidizer mole fraction (%)			
	C_2H_4	N_2	CO_2	He	O_2	N_2	CO_2	He
8F-AIR	80	20	0	0	21	79	0	0
8F2C-AIR	80	0	20	0	21	79	0	0
8F2H-AIR	80	0	0	20	21	79	0	0
6F-AIR	60	40	0	0	21	79	0	0
6F4C-AIR	60	0	40	0	21	79	0	0
6F4H-AIR	60	0	0	40	21	79	0	0
3F-AIR	30	70	0	0	21	79	0	0
3F7C-AIR	30	0	70	0	21	79	0	0
3F7H-AIR	30	0	0	70	21	79	0	0

In conclusion, the oxidizer-side dilution is found to be much more effective in modifying the flame radius and temperature behavior, and as such this method will be primarily considered in the subsequent parametric studies for flame extinction to be discussed in Chapter 6.

5.2. Cases with Mixed Diluents

In Table 5.1, Cases 3F7M-3A and 3F-3A7M were considered as an attempt to match the mixture-averaged specific heat so that the ideal adiabatic flame temperature becomes identical to that in the baseline case, 3F-3A. Despite the effort, however, the actual flame temperature in the transient solutions differs significantly from the adiabatic flame temperature.

Figures 5.8 and 5.9 show the flame radius and temperature history during the first 2 seconds for the three cases 3F-3A, 3F7M-3A, and 3F-3A7M. It is clearly seen that the flame temperature for each case differs significantly from one another, as much as 600K.

This is due to the differences in radiative and conductive heat losses through the surrounding gases due to the different addition of CO_2 and helium. As discussed in the previous section, addition of diluents on the oxidizer side is found to be more effective in lowering the flame temperature. Figures 5.8 and 5.9 show a consistent trend in that flames with lower temperature are weaker and have smaller flame radius, and this trend will be further discussed in Chapter 6.

This exercise suggests that elimination of thermodynamic effect (through the specific heat modification) for various diluent gases cannot be simply achieved by the matching of the mixture-averaged specific heat, because the additional changes in radiation and transport properties also play a significant role in determining the flame radius and temperature behavior.

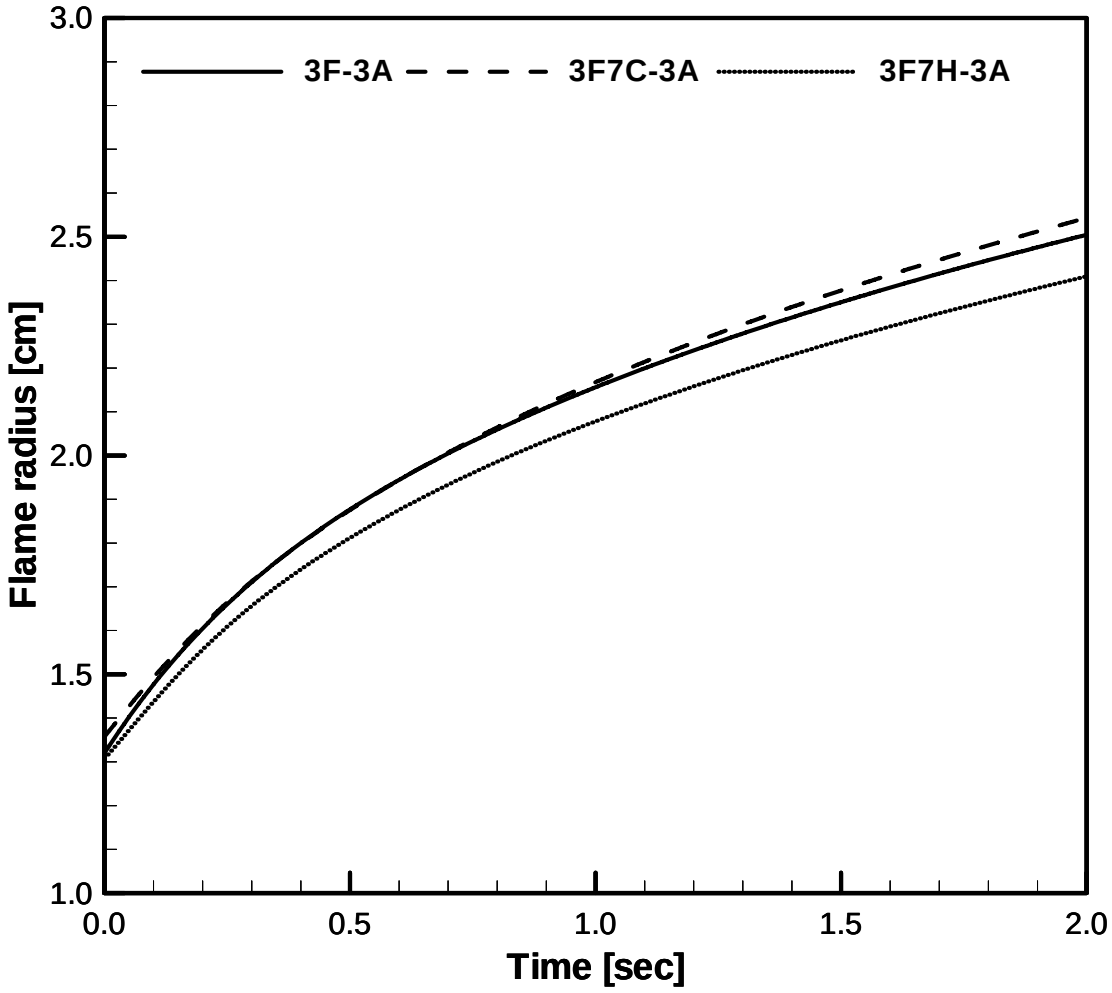

Figure 5.1: Flame radius versus time for different fuel-side dilution cases with volume flow rate 12 ml/s.

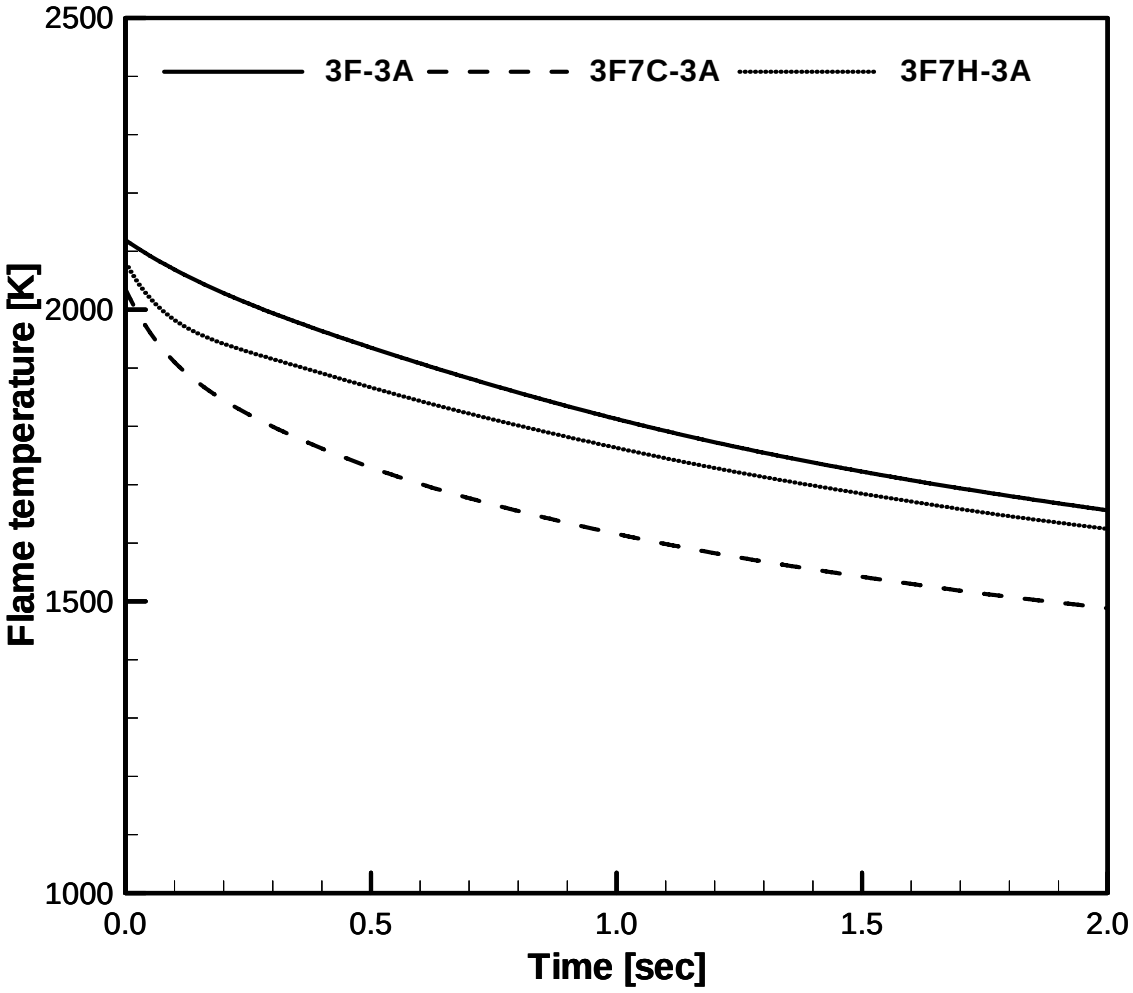

Figure 5.2: Flame temperature versus time for different fuel-side dilution cases with volume flow rate 12 ml/s.

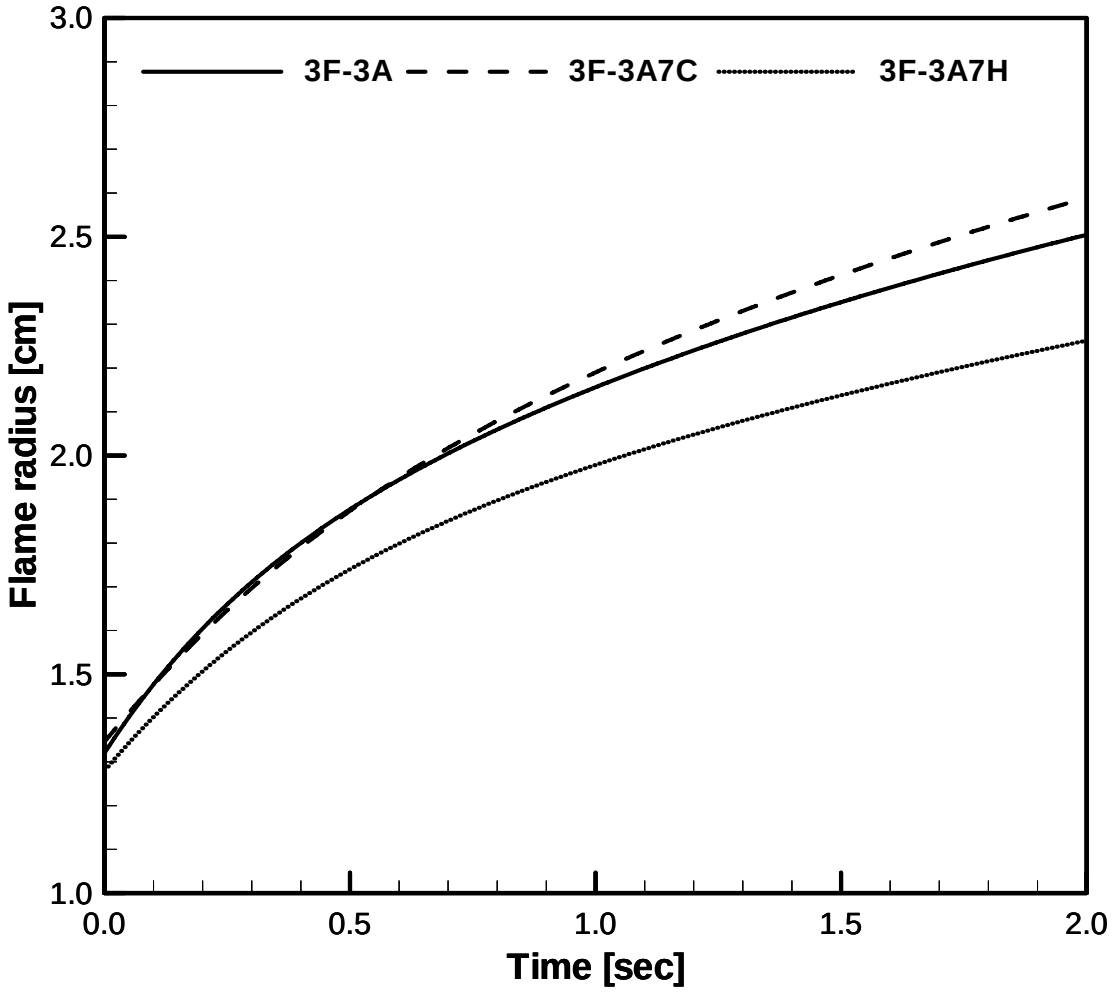

Figure 5.3: Flame radius versus time for different oxidizer-side dilution cases with volume flow rate 12 ml/s.

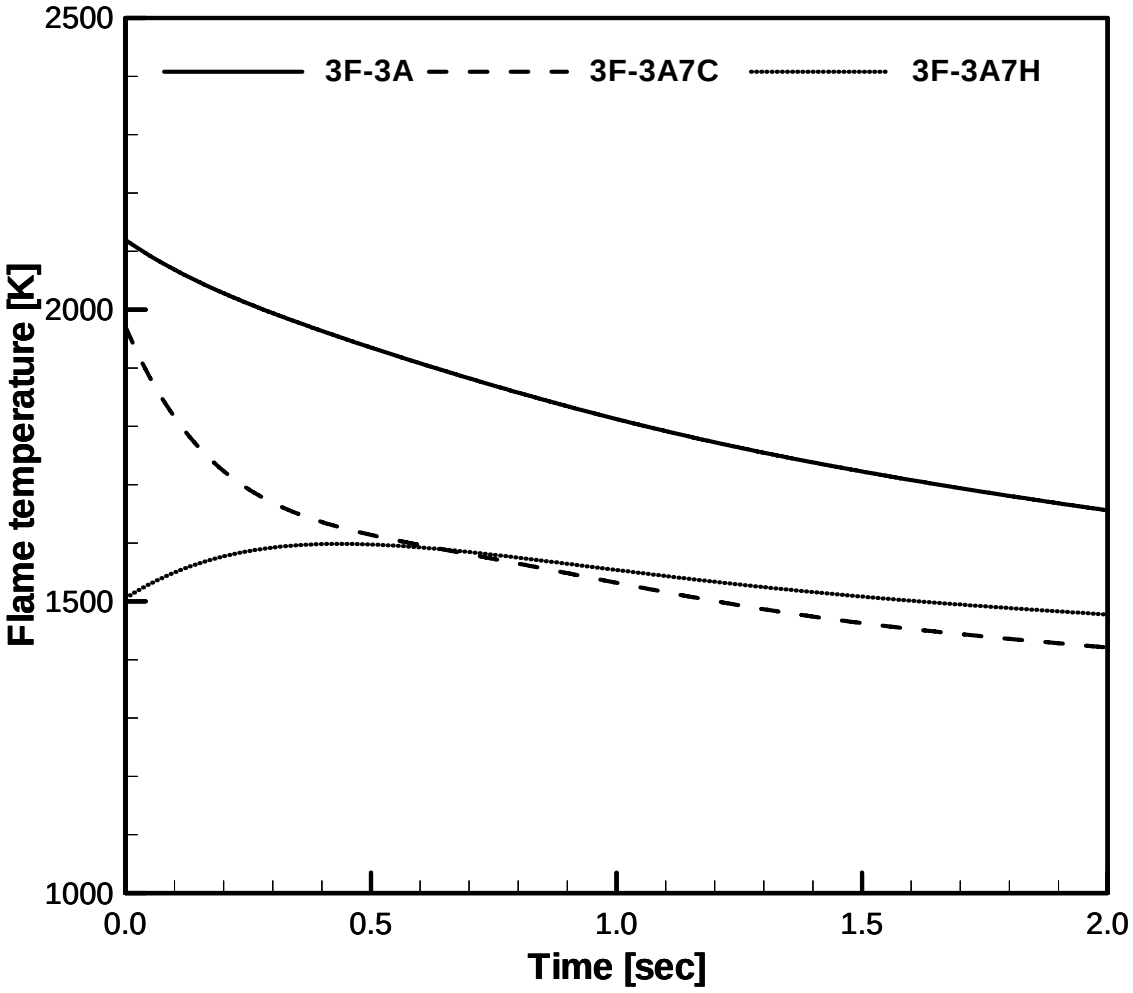

Figure 5.4: Flame temperature versus time for different oxidizer-side dilution cases with volume flow rate 12 ml/s.

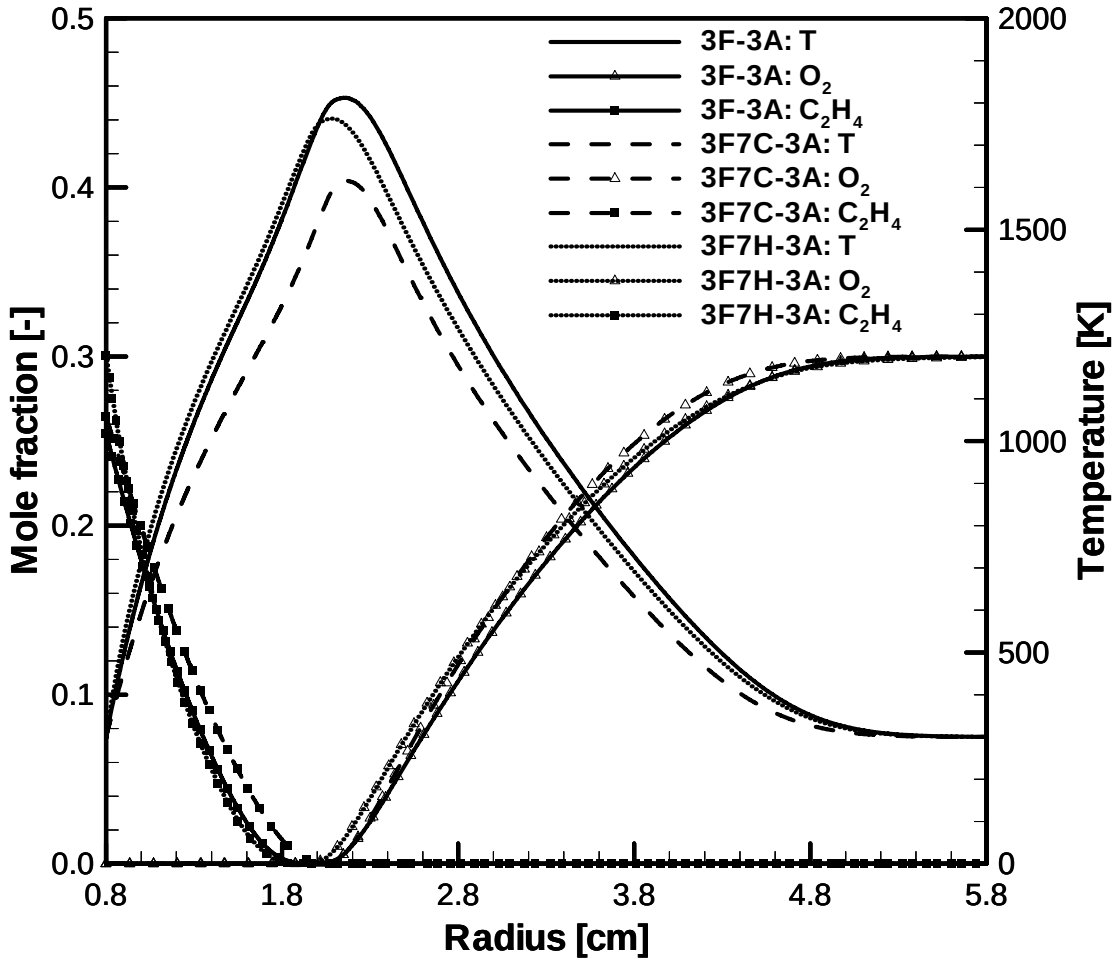

Figure 5.5: Transient temperature and mole fraction profiles at 1.0 second for different fuel-side dilution cases with volume flow rate 12 ml/s.

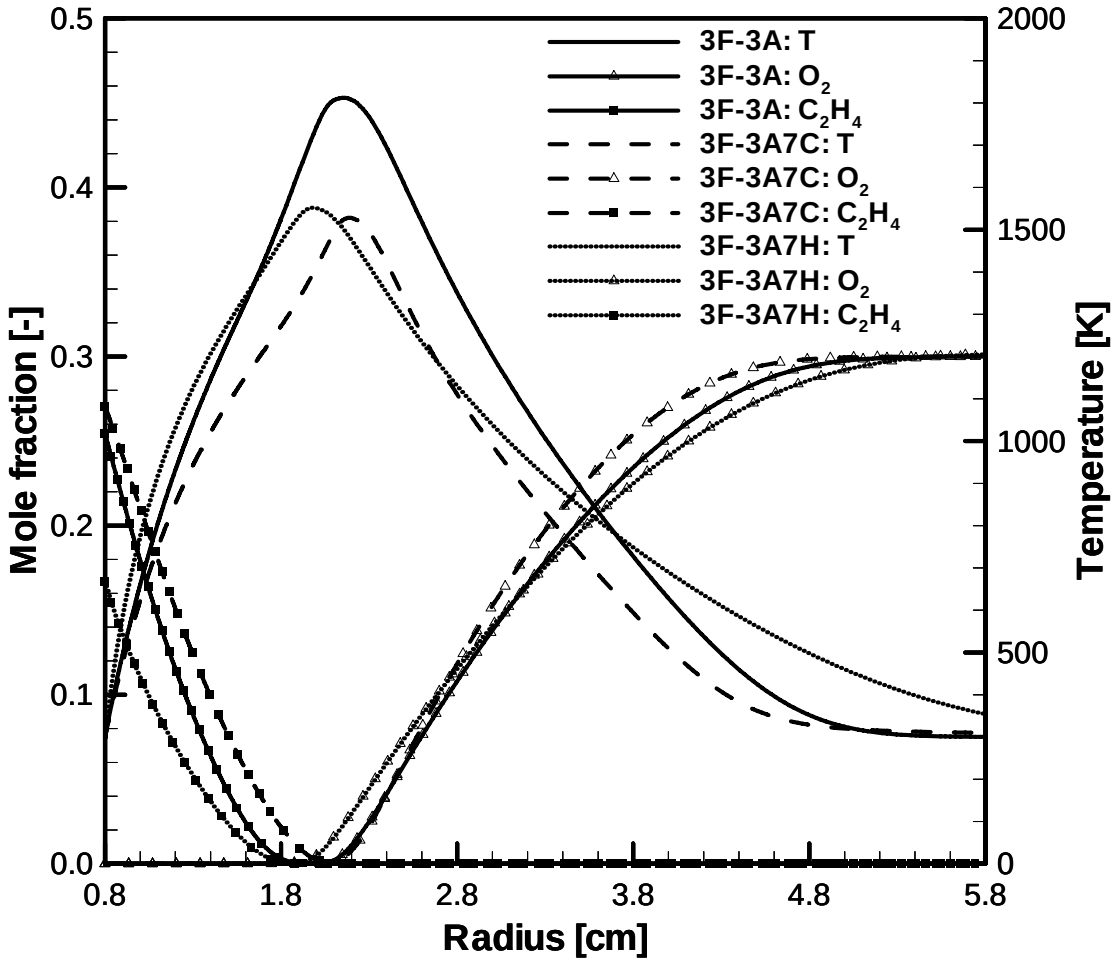

Figure 5.6: Transient temperature and mole fraction profiles at 1.0 second for different oxidizer-side dilution cases with volume flow rate 12 ml/s.

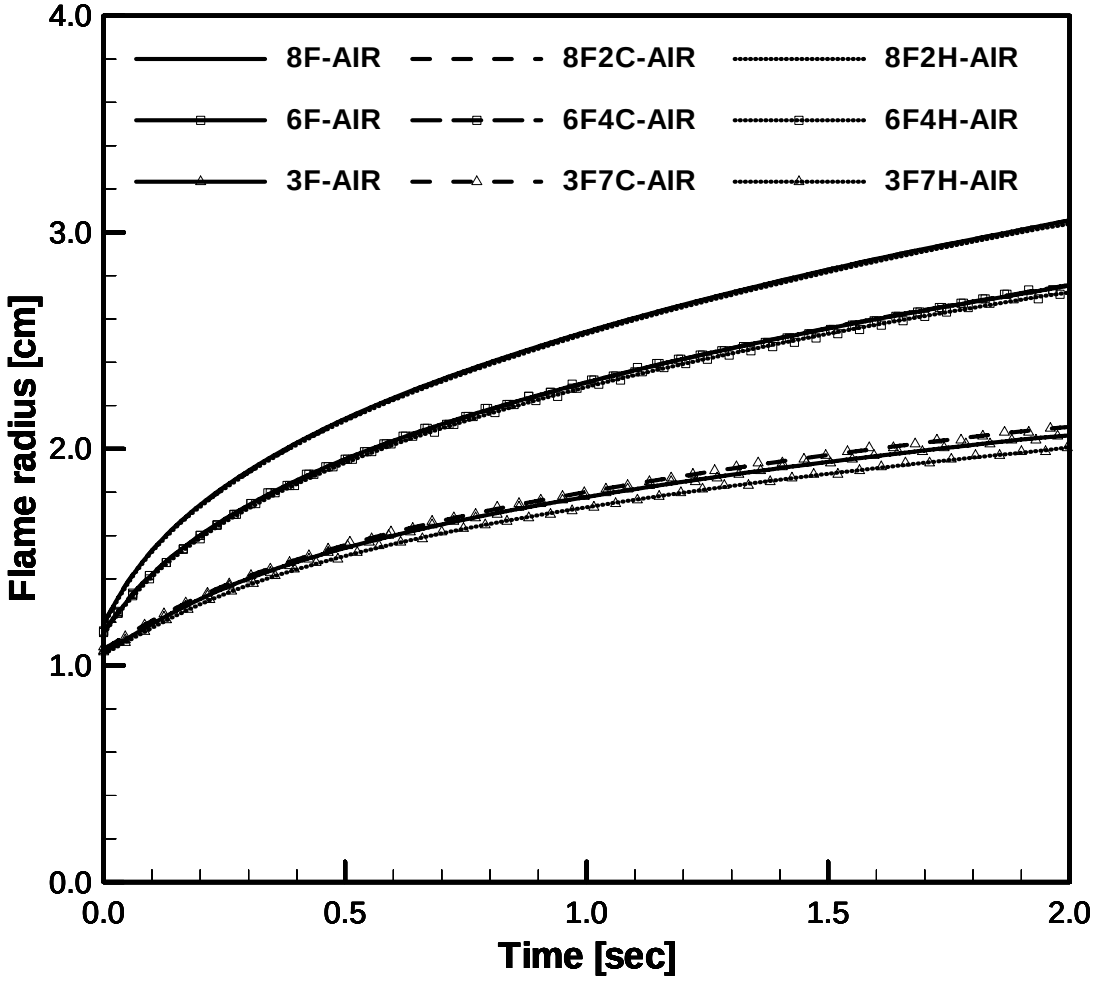

Figure 5.7: Transient flame radius history for different fuel-side dilution cases with volume flow rate 6 ml/s.

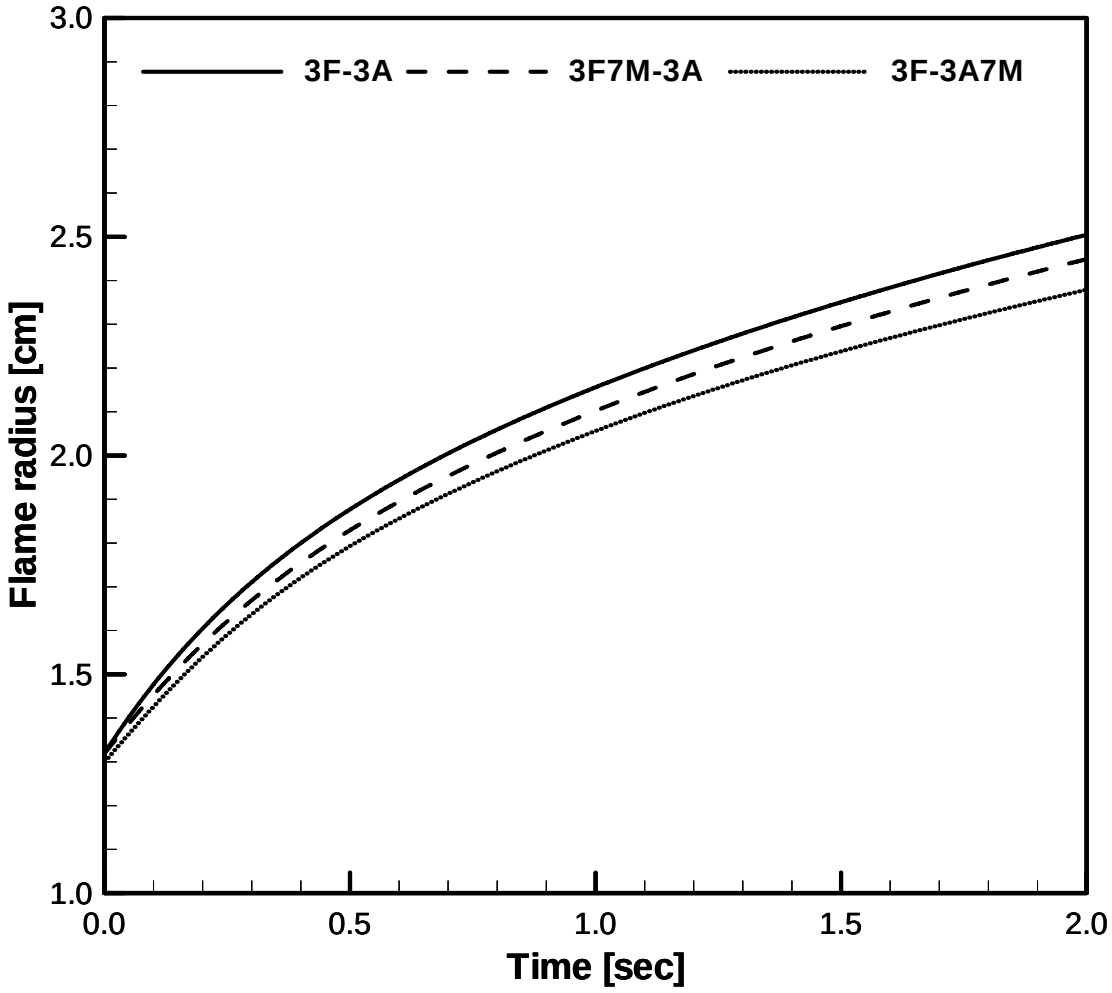

Figure 5.8: Flame radius versus time for different dilution cases with volume flow rate 12 ml/s.

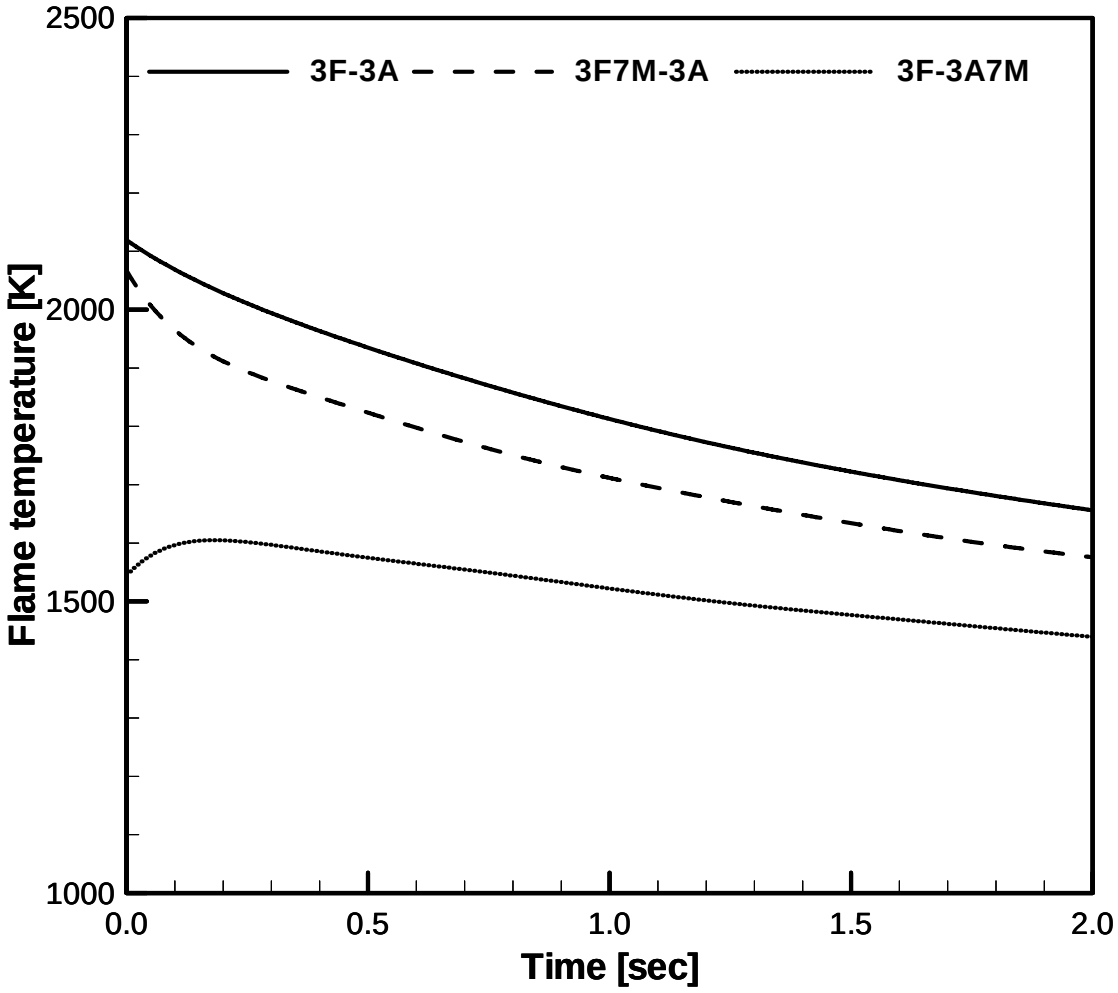

Figure 5.9: Flame temperature versus time for different dilution cases with volume flow rate 12 ml/s.

Chapter 6 Effects of Oxidizer-Side Dilution on Flame Behavior

From Chapter 5 we understand that dilution on the fuel side has relatively small effects on the flame radius and temperature behavior compared with dilution on the oxidizer side, such that the rest of the study will focus on oxidizer-side dilution. In this chapter, we will investigate the influence of oxidizer-side dilution in further detail.

6.1. Effect of Diluent Species Type on Flame Behavior

In this study, we have covered three different kinds of diluents, N_2, CO_2, and helium. Figures 5.3 and 5.4 show the history of flame radius and flame temperature for three different oxidizer-side dilution cases, 3F-3A, 3F-3A7C, and 3F-3A7H. In order to understand the effect of different diluent species on flame behavior, we will study these cases in detail.

6.1.1. Steady solution analysis for different oxidizer dilution cases

According to the discussion of the characteristic diffusion time scale at the end of Chapter 2, the influence of the initial condition uncertainties can be neglected after around 0.2 second; however, it is still valuable to investigate the steady solution that is the initial condition for the subsequent transient calculation.

As observed in Figure 5.3, different oxidizer-side dilution cases start from different flame radius and the initial flame radius is in the increasing order for He, N_2, and CO_2, and the flame radius of He is especially lower. This trend is clearly exhibited in Figure 6.1 which shows the initial temperature profiles within the narrow domain near the burner surface. The difference in initial flame radius is primarily due to the different diffusion coefficients. Table 6.1 lists the binary diffusion coefficient of O_2 versus different diluents for the corresponding oxidizer-side dilution cases at different temperature. It shows that at any temperature the binary diffusion coefficient is always the lowest for CO_2, it is a

little larger for N_2 although the difference is not significant, and it is the highest for helium and much larger than the other two. With the larger diffusion coefficient of O_2 in the helium diluted oxidizer mixture compared to that in other cases, O_2 travels faster towards the fuel-rich side, thus the fuel (C_2H_4) does not need to travel outwards that far to reach the oxidizer for stoichiometric combustion, and consequently flame radius is smaller; this explains why helium diluted case has the smallest flame radius in the steady solution. On the contrary, in the CO_2 dilution case O_2 has the largest diffusion coefficient, thus the flame radius is the largest; however, the difference of diffusion coefficient between CO_2 and N_2 is very small, so the steady solution flame radius difference is not significant, either between CO_2 and N_2 dilution cases.

Table 6.1: Binary diffusion coefficients at different temperatures (unit: cm^2/s)

Temperature [K]	300	800	1300	1800	2300
O_2-N_2 (3F-3A)	0.21	1.131	2.542	4.359	6.54
O_2-CO_2 (3F-3A7C)	0.156	0.894	2.033	3.499	5.258
O_2-He (3F-3A7H)	0.767	3.908	8.721	14.94	22.425

Besides flame radius, flame temperature is also very different in the steady solution for different oxidizer-side dilution cases. Figures 5.4 and 6.1 both show that when N_2 is substituted by CO_2 on the oxidizer side (3F-3A7C), initial flame temperature is lower than that in the baseline case 3F-3A by about 150 K. This is because CO_2 has a higher specific heat (ρCp) than N_2, resulting in a lower temperature for the same heat release.

Figures 5.4 and 6.1 also show that, when N_2 is substituted by helium on the oxidizer side, despite the lower specific heat (ρCp) of helium, the initial flame temperature is much lower, which can be explained by the significantly larger thermal conductivity of helium. Figure 6.2 shows the comparison of thermal conductivity of some primary species in the combustion system, from which we find that, over a wide temperature range (300K ~ 2300K), thermal conductivity of helium is on the average 4 times as large as that of other species. Since C_2H_4 composition in the fuel stream and the fuel flow rate are both identical for all the cases, similar amount of chemical heat release rate is expected; for the initial narrow flame, heat conduction is the primary way of heat loss, so

heat conduction is also expected to be close to each other among all the cases. Consequently, temperature gradient and peak temperature are expected to be much lower on both boundaries for the helium dilution case in order to keep the energy balance.

Note that the above discussion assumes that heat conduction is the dominant heat loss mode, and this is can be confirmed by the data in Table 6.2. This table shows the volume-integrated quantities of the heat release and various heat losses over the steady solution calculation domain for the three different dilution cases. The radiation heat loss is neglected for all steady calculations and thus is not listed. It is evident that the heat release is predominantly contributed by the conduction heat loss. As mentioned in Chapter 4, the radiation heat loss was neglected for all the steady calculations due to the very thin flame zone and thus not listed in Table 6.2.

Table 6.2: Volume-integrated heat release and heat loss for different cases (unit: W)

Case number	3F-3A	3F-3A7C	3F-3A7H
Q_{reac}	193.867	192.843	192.943
Q_{cond}	191.420	190.139	191.527
Q_{conv}	6.557	6.304	1.096
Q_{diff}	-4.111	-3.606	0.320

6.1.2. Transient result analysis for different oxidizer dilution cases

Steady solution analysis helps us understand the initial condition of flame radius and flame temperature, based on which we will investigate the transient flame behavior calculated from the steady solution as the initial condition.

Flame radius curves in Figure 5.3 show that the flame radius is the lowest for the helium dilution case and the highest for the CO_2 dilution case. This can be explained by comparing the diffusion coefficients among different species, which is almost identical to the analysis for steady solution and thus not repeated here. The results shown in Figure 5.3 are consistent with the experimental observation (Chernovsky, 2006). Figure 6.3 shows experimental observation of flame radius for three different oxidizer-side dilution cases FUE-3A, FUE-3A7C, and FUE-3A7H, as listed in Table 6.3. Note that, for all the cases in Figure 6.3, fuel side is composed of 100% C_2H_4. Although Figure 6.3 and Figure

5.3 can not be directly compared, a consistent trend is observed in which the CO_2 dilution case yields the largest radius and the helium dilution case yields the smallest one.

Table 6.3: Cases in experiments with different oxidizer-side dilution

Case number	Fuel mole fraction (%)				Oxidizer mole fraction (%)			
	C_2H_4	N_2	CO_2	He	O_2	N_2	CO_2	He
FUE-3A	100	0	0	0	30	70	0	0
FUE-3A7C	100	0	0	0	30	0	70	0
FUE-3A7H	100	0	0	0	30	0	0	70

As briefly discussed in Chapter 5, Figure 5.4 shows the distinct trend of flame temperature for the three oxidizer-side dilution cases. We find that the 3F-3A7H starts with much lower flame due to the high conductivity of helium. On the other hand, the initial flame temperature for the 3F-3A7C shows a value close to the reference condition. As the flame size grows after the ignition, however, the flame temperature for the 3F-3A7C case drops quickly, while the flame temperature for the 3F-3A7H case first increases and then slowly decreases. Consequently, after approximately 0.8 seconds the two curves cross over and that the flame temperature for the 3F-3A7H case becomes higher than that in the 3F-3A7C case. For the helium dilution case, the large heat conduction is prominent only in the early phase when the flame size is narrow, but eventually the flame temperature catches up due to the lower value of specific heat. The initial rise of flame temperature can be considered a sudden burst of flame which is originally confined to a narrow domain but then released to an open space. As the flame size grows further, the flame temperature decreases gradually even for helium dilution cases due to radiative losses by product gases. The computational results agree with experimental observation, for example, it was very difficult to ignite helium diluted flames and normally higher ignition power was needed, which is due to the higher heat conductivity of helium discussed above.

Figure 5.4 suggests that, despite the higher initial flame temperature, the CO_2 dilution can lead to a significant temperature drop by additional heat losses. Nevertheless, none of the cases was able to exhibit flame extinction within 2.2 seconds, which is

consistent with the experiment. However, the numerical calculations can be further extended to investigate the extinction behavior for four test cases: in addition to the three cases discussed in Figure 5.4, the case of 70% dilution with a mixture of CO_2 and helium was also considered.

Figures 6.4 and 6.5 show, respectively, the flame radius and temperature evolution for the four test cases. It is clearly seen that the 3F-3A7C case extinguishes earliest (approximately at 8 seconds), while the 3F-3A7H extinguishes at much later time (approximately at 19 seconds), although it is still earlier than the baseline case (3F-3A). When the helium and CO_2 mixture was used (3F-3A7M), the extinction time was in between that of 3F-3A7C and 3F-3A7H. It is interesting to note that the flame temperature at extinction (the sudden drop in the curve in Figure 6.5) appears approximately the same for all cases considered. The results show both CO_2 and helium dilutions have flame suppression effects, but for two different physical causes: the latter is due primarily to enhanced conductive heat loss, while the former is through increased radiative heat losses. The results in Figures 6.4 and 6.5 suggest that CO_2 serves as a better fire suppressant in microgravity application in favor of its stronger radiative performance. The fact that the 3F-3A7M case falls in between the two cases further confirms that the radiative loss has a more dominant effect. The suppression effect can be quantitatively measured by the extinction time, thus it is concluded that CO_2 has a suppression effect of around 2.5 as strong as that of helium in terms of flame extinction time. The finding of CO_2 as a better suppression agent than helium contrasts a recent study by Ronney (Son *et al.* 2006) in which helium was suggested as a strong candidate for fire suppressant. In this study, however, the flame configuration in their study is flames spreading over thermally thick fuel beds.

6.2. Effects of Dilution Level on Flame Behavior

We have investigated the influence of different diluents on the flame behavior, and now we will study how dilution amount affects the flame behavior.

Table 6.4 provides a list of oxidizer-side dilution cases, in which all have the same fuel mixture composition (30% C_2H_4 / 70% N_2) but oxidizer-side N_2 mole fraction is gradually changed to CO_2 and helium.

Table 6.4: Case matrix for oxidizer-side dilution amount comparison

Case number	Fuel mole fraction (%)				Oxidizer mole fraction (%)			
	C_2H_4	N_2	CO_2	He	O_2	N_2	CO_2	He
3F-3A	30	70	0	0	30	70	0	0
3F-3A1C	30	70	0	0	30	60	10	0
3F-3A4C	30	70	0	0	30	30	40	0
3F-3A7C	30	70	0	0	30	0	70	0
3F-3A1H	30	70	0	0	30	60	0	10
3F-3A4H	30	70	0	0	30	30	0	40
3F-3A7H	30	70	0	0	30	0	0	70

Figure 6.6 shows transient flame radius profile for CO_2 oxidizer-side dilution cases (3F-3A, 3F-3A1C, 3F-3A4C, and 3F-3A7C) with different dilution amount ranging from 0% to 70%, and Figure 6.7 shows transient flame temperature profile for the same CO_2 oxidizer-side dilution cases. Figure 6.8 shows transient flame radius profile for helium oxidizer-side dilution cases (3F-3A, 3F-3A1H, 3F-3A4H, and 3F-3A7H) with different dilution amount ranging from 0% to 70%, and Figure 6.9 shows transient flame temperature profile for the same helium oxidizer-side dilution case group.

Figures 6.6 and 6.7 show that when oxidizer side helium dilution amount increases from 0% to 10% to 40% to 70%, the extinction time decreases from 20.5 second to 17.2 second to 10.9 second to 7.9 second. The comparison shows that the suppression effect is positively correlated with the oxidizer side CO_2 dilution amount. Figure 6.6 shows that cases with more CO_2 dilution have larger flame radius, and this is due to the relatively lower diffusion coefficient of O_2 in CO_2 diluted mixture compared to in N_2 diluted mixture. Combining Figures 6.6 and 6.7, we also find that, a larger flame radius corresponds to a lower flame temperature, and this is because a larger flame tends to result in more radiative heat loss and thus a lower temperature.

Figures 6.8 and 6.9 show that, extinction is observed for all the oxidizer-side helium dilution cases. Among these cases, the baseline case 3F-3A extinguishes the latest, at 20.5 second, and adding helium on the oxidizer side helps to advance the flame extinction although the influence on extinction timing is much smaller compared to the influence for

fuel side dilution cases (as seen in Figures 6.6 and 6.7). We also find that the case that extinguishes the earliest (at 18 second) is 3F-3A4H, while case 3F-3A7H extinguishes at around 19 second, which means the suppression effect is not positively correlated with helium dilution amount on the oxidizer side. The trend in Figure 6.8 shows that cases with more helium dilution have smaller flame radius, and this is partially due to the relatively higher diffusion coefficient of O_2 in helium diluted mixture compared to in N_2 diluted mixture. Figure 6.9 shows that, within the first 10 second decreasing flame temperature is observed with the increase of oxidizer side helium dilution amount; higher temperature results in stronger flame intensity when radiative heat loss is not dominant, and this partially explains the decreasing trend of flame radius with the increasing oxidizer side helium dilution amount. After 10 second, although the order of flame temperature among different dilution cases changes the difference in temperature is very small, and since the trend of flame radius has already been set up it is not significantly affected by the new order of temperature.

6.3. Quantitative Analysis of CO_2 Dilution Cases

In Section 6.2, we concluded that CO_2 has a stronger suppression effect on spherical diffusion flame due primarily to the radiative heat loss. However, the actual effects of CO_2 can be more complex, including thermal, diffusion, chemical, and radiation effects. While it has been commonly argued that thermal effect plays an important role when CO_2 is added to combustion systems (Lee *et al.* 2001), no literature has provided a detailed quantitative assessment among the various effects imparted by the CO_2 dilution for spherical diffusion flame. Here we attempt to provide clearer insights into this issue.

To distinguish various effects clearly, various realistic and hypothetical cases were considered. Case A is the original 3F-3A case where 70% N_2 is used as diluent on the oxidizer side. Case B is modified from A, assuming that the oxidizer-side diluted N_2 has the radiation property of CO_2 while retaining its original thermal, transport, and chemical properties. The difference in the flame temperature between Cases A and B should reveal the pure radiation effect of CO_2 as diluent on the oxidizer side. Next, Case C considers CO_2 to replace the oxidizer-side diluted N_2 but the artificial CO_2 as diluent behaves as an inert gas without further participating in chemical reaction (in other words, the diluent

CO_2 is distinguished from the product CO_2). Thus, the difference between Cases B and C should represent the pure thermal and transport effects of CO_2 on the oxidizer side. Last, Case D is the original CO_2 dilution case (3F-3A7C) without further modification, such that the result shows the entire effects by CO_2. In other words, the difference between Cases C and D would show the chemical effects of CO_2 only.

Figure 6.10 compares the flame temperature behavior for these artificial cases. We find that the temperature comparison always has the same trend, in which temperature is in the decreasing order for A, B, C, and D. At 2.0 second, the relative temperature drops caused by radiation, thermal/transport, and chemical effects are 145K, 75K, and 15K, respectively. Therefore, it is confirmed that radiation is indeed the dominant effect for the flame weakening when CO_2 is added as diluent in the ambient air. Quantitative analysis shows that radiation accounts for about 60% of the overall suppression effect, thermal/transport accounts for 30%, and chemical reaction has the minimum effect, account for only 10% of the overall suppression effect.

To further separate the thermal and transport effects of the diluent gases, we have conducted the following exercise. All four cases use nitrogen as diluent, so that no additional radiation effect (other than the product species) was considered. Compared to Case A (3F-3A), Case E assumes that nitrogen has both thermal and transport properties of CO_2; Case F assumes that the nitrogen has only the thermal property of CO_2; and finally Case G assumes that the nitrogen has only the transport property of CO_2.

Figure 6.11 compares the four cases and shows that, the transport effect alone of CO_2 is very small especially when the flame grows wider, which is demonstrated by the comparison between curve A and G. The higher temperature in G than in A also implies that lower diffusion coefficient of CO_2 helps to attenuate the diffusive heat loss from the flame and this effect is only significant for a narrow flame. The temperature difference between F and A is much larger than the temperature difference between G and A, which clearly shows that the thermal effect, which is mostly due to the higher specific heat of CO_2, is more important than the transport effect. Consequently, the net thermal/transport combined effect of CO_2 dilution is to lower the flame temperature, but is a balance of the two competing effects. Generally, the combined thermal/transport effect, instead of thermal or transport effect alone, makes more sense when it is compared with radiation

effect. The temperature of curve E in Figure 6.11 is higher than that of curve B in Figure 6.10, which again confirms that the radiation effect is the dominant reason for the temperature drop in CO_2 dilution.

6.4. Discussion of Critical Heat Loss for Extinction

This investigation was motivated by a recent study by Axelbaum and coworkers (Santa *et al.*, 2007), in which it was reported that flame extinction occurs when the ratio of the radiative heat loss to the heat release rates becomes a critical value of approximately 0.7, suggesting that there exists a unified heat generation/loss balance mechanism that is responsible for the microgravity flame extinction behavior. To assess the validity of this finding, we have conducted the energy budget analysis by quantifying various terms in the energy equation (Equation 2.12):

$\overline{C_p}\rho\dfrac{\partial T}{\partial t}$: storage (Q_{stor})

$\overline{C_p}\rho u\dfrac{\partial T}{\partial r}$: convection (Q_{conv})

$\dfrac{1}{r^2}\dfrac{\partial}{\partial r}\left(\lambda r^2\dfrac{\partial T}{\partial r}\right)$: conduction (Q_{cond})

$\sum_{k=1}^{K}\left(\dot{\omega}_k\Delta h^{\circ}_{f,k}W_k\right)$: reaction (Q_{reac})

$\rho\sum_{k=1}^{K}\left(C_{p,k}(YV)_k\right)\dfrac{\partial T}{\partial r}$: diffusion (Q_{diff})

$\nabla\cdot\mathbf{q}_R$: radiation (Q_{rad})

To analyze their contribution to the total energy budget, each term was integrated over the entire computational domain and its temporal evolution was examined.

Figure 6.12 shows the volume integrated energy terms for case 3F-3A7H. Throughout the entire flame history three terms are dominant, Q_{stor}, Q_{reac}, and Q_{rad}. The fact that diffusive and convective loss terms are less significant has been discussed in the previous section, hence no further discussion is needed. The results show that the volumetric heat generation by reaction remains almost constant up to the extinction point, while the radiative heat loss increases with the flame volume and simultaneously the

energy storage in the volume is diminishing. It is evident that the extinction as a criticality phenomenon occurs when the volumetric energy level is reduced to a critical limit due to the increasing radiative heat loss. During this time, the total chemical reactivity manages to maintain a constant level by broadening the reaction zone until the nonlinear criticality limit is reached.

To verify the findings by Santa *et al.* (2007), similar calculations were performed for the three diluent cases and the results for Q_{rad}/Q_{reac} ratio are shown in Figure 6.13. Although the values are close to 0.7, there is still a significant level of variations among the cases, up to almost 0.2. Therefore, the critical heat loss ratio $Q_{rad}/Q_{reac} = 0.7$ does not appear to be an accurate and reliable indicator to predict the extinction condition over a wide range of parametric conditions.

To this end, we recall that the interesting observations throughout Figures 6.5, 6.7, 6.9, that the flame extinction occurs at an almost flame temperature of 1130K for the wide variety of parametric conditions in this study. This suggests that the critical flame temperature may serve as a more consistent criterion for extinction.

In the above discussion, integrating Q_{reac} and Q_{rad} over the entire domain provides global information. Alternatively, the integration can be done over a narrower region in order to distinguish the energy balance within active flame zones only. For this purpose, the integration was conducted within the zone of full-width-half-maximum temperature zone, i.e. the region in which temperature is above the half peak value. Figure 6.14 shows the comparison of the two dominant terms, Q_{reac} and Q_{rad}, computed based on two different integral volumes, for the 3F-3A4H case. The two integration methods result in almost indistinguishable curves, indicating that the contribution of the two terms outside the main reaction zones is negligible. On the other hand, Figure 6.15 shows the same comparison for the 3F-3A4C case, showing that there is a significant difference in the volume-integrated radiative heat loss. This further confirms that the abundant CO_2 diluent gases actively contribute to radiative reabsorption of the heat generated by the flame, even in the region where temperature is substantially lower. This result implies that the critical Q ratio as an extinction criterion can become practically difficult to apply due to the uncertainties in the estimation of Q_{rad}, especially when the radiative heat loss to the surrounding gases becomes important.

6.5. Effects of Diluent Types on Ignition

Besides flame extinction behavior we are also interested in flame ignition behavior because flame ignition is also part of fire safety concerns. Normally fire starts from a diffusion flame so we are more interested in diffusion flame ignition. We determine the difficulty of igniting a diffusion flame is by investigating the steady calculation and finding the minimum initial peak temperature with a prescribed profile that can ignite the diffusion flame. Table 6.5 shows the ignition temperature for different dilution cases and the fuel/oxidizer components of which are described in Table 6.6.

Table 6.5: Ignition temperature for different dilution cases

Case number	3F-3A	3F-3A2C	3F-3A4C	3F-3A2H	3F-3A4H
T_{min} (K)	1165	1170	1210	1190	1215

Table 6.6: Case matrix for diffusion flame ignition comparison

Case number	Fuel mole fraction (%)				Oxidizer mole fraction (%)			
	C_2H_4	N_2	CO_2	He	O_2	N_2	CO_2	He
3F-3A	30	70	0	0	30	70	0	0
3F-3A2C	30	70	0	0	30	50	20	0
3F-3A4C	30	70	0	0	30	30	40	0
3F-3A2H	30	70	0	0	30	50	0	20
3F-3A4H	30	70	0	0	30	30	0	40

Table 6.5 shows that applying helium and CO_2 as oxidizer-side diluent helps to increase ignition temperature (although the increase is small) compared to the baseline case where N_2 is applied as the diluent, and therefore it helps to impede fire initiation. The higher ignition temperature for helium oxidizer dilution case shows that it is more difficult to ignite a diffusion flame if helium is added to the environment. This fact was

also observed during the experiments. Based on this observation, we would propose to add helium in the environment in order to help prevent diffusion flame ignition.

Besides diffusion flame ignition, we also would like to consider premixed flame ignition as a comparison. In order to calculate premixed flame ignition temperature we assume a mixture of C_2H_4, helium, and corresponding diluents based on stoichiometric condition and calculate the final system temperature from the initial temperature and with the constant pressure adiabatic condition, initial temperature is gradually increased until the final temperature abruptly increases. The premixed flame ignition temperature for the different oxidizer-side dilution cases is listed in Table 6.8.

Table 6.7: Ignition temperature for different dilution cases as premixed flames

Case number	3F-3A	3F-3A7C	3F-3A7H
T_{min} (K)	1180	1174	1182

Table 6.8: Case matrix for premixed flame ignition comparison

Case number	Initial mixture mole fraction (-)				
	C_2H_4	O_2	N_2	CO_2	He
3F-3A	3/40	9/40	28/40	0	0
3F-3A7C	3/40	9/40	7/40	21/40	0
3F-3A7H	3/40	9/40	7/40	0	21/40

As shown in Table 6.7, when CO_2 is applied as the diluent the minimum ignition temperature is obtained, and this is because both N_2 and helium are inert but when CO_2 is added the dissociation of CO_2 helps to initiate the flame. Either CO_2 or helium is applied as the diluent the ignition temperature is very close to each other. This means, for a premixed flame when helium is used as the diluent it does not obviously affect the ignition temperature much. The reason that helium does not have an obvious difference with N_2 is that the thermal properties like thermal conductivity is not considered in

premixed ignition temperature calculation and therefore the trend is different from that in diffusion flame ignition comparison. Since in most combustion systems fuel and oxidizer are initially spatially separated (Law, 2006), we should pay greater attention to diffusion flame combustion in terms of fire prevention, and therefore adding helium seems appropriate which would increase the ignition temperature. At the same time, since helium is health friendly adding a certain amount of helium in the space shuttle does not have any biological impact on the people in it. On the other hand, when a fire disaster happens we recommend using CO_2 as the fire extinguishing agent because our study shows that adding CO_2 on the oxidizer side helps to bring forward fire extinction.

6.6. Steady Solution Analysis for Steady Flame Pursuit

Although it has been a few years since people started microgravity combustion research the question is still open whether there exists a steady flame in microgravity. Due to the limitation of experimental conditions, microgravity combustion experiments so far normally lasted at most for several seconds. Within that scale of time period spherical diffusion flames were observed to either keep growing or extinguish, and people are wondering whether spherical diffusion flame can sustain for ever or whether there could be a steady flame. Since it was difficult to verify this issue by experiment due to the limitation in the measurement of long time behavior, we would like to exploit our simulation model to answer this question.

With the vehicle of our numerical model we can try to answer this question computationally. If we have a steady flame we should be able to find a steady solution with a sufficiently large calculation domain. In our previous study we have always applied a very narrow domain, but here we choose much larger domain with the outer boundary (R_{max}) located at 21 cm, 61 cm, 101 cm, and 151 cm separately. Figure 6.16 shows a group of steady solution temperature profiles with different domain size conditions. We find that with the increase of domain size although flame temperature seems to be stabilized at about 2600 K and peak temperature location also seems to approach a limit value of 13 cm, the flame always keeps growing. We always have a non-zero gradient on the right edge of temperature profile, which means the outer boundary does not satisfy the ambient condition in which case we should have zero gradient of

temperature on the outer boundary. This implies that even though we keep increasing domain size we still cannot obtain a steady solution which has a zero gradient on the outer boundary.

Note that the steady solutions in Figure 6.16 are obtained with adiabatic conditions where radiative heat loss is neglected; however, in reality there is always gas radiation and radiation could increase dramatically with the growth/expansion of the spherical flame since the amount of radiative heat loss is largely related to the flame zone volume. With the consideration of gas radiation, we would expect the flame to extinguish much sooner before the right edge could reach as far as shown in Figure 6.16. Based on this analysis, we can conclude that there does not exist a steady spherical diffusion flame in microgravity.

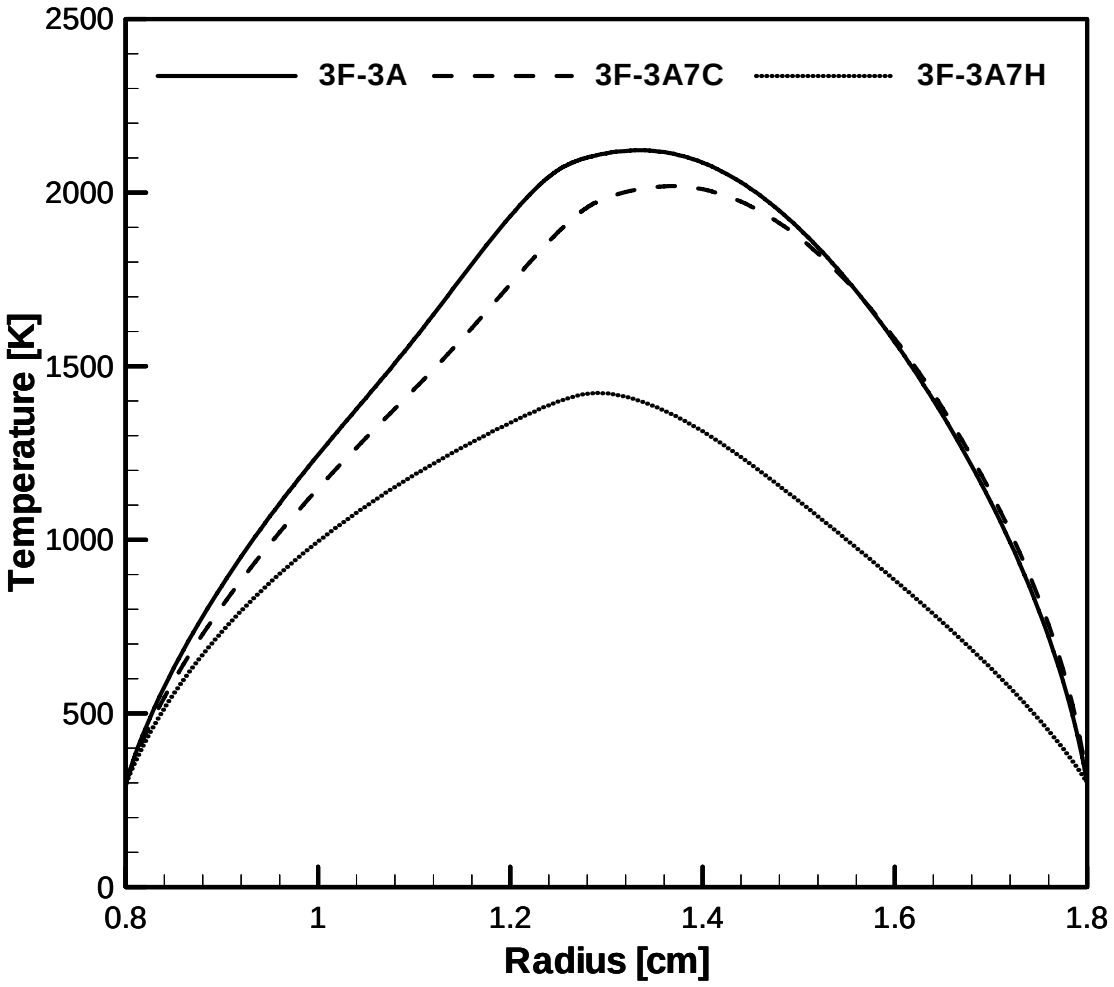

Figure 6.1: Steady solution temperature profiles for different oxidizer-side dilution cases with volume flow rate 12 ml/s.

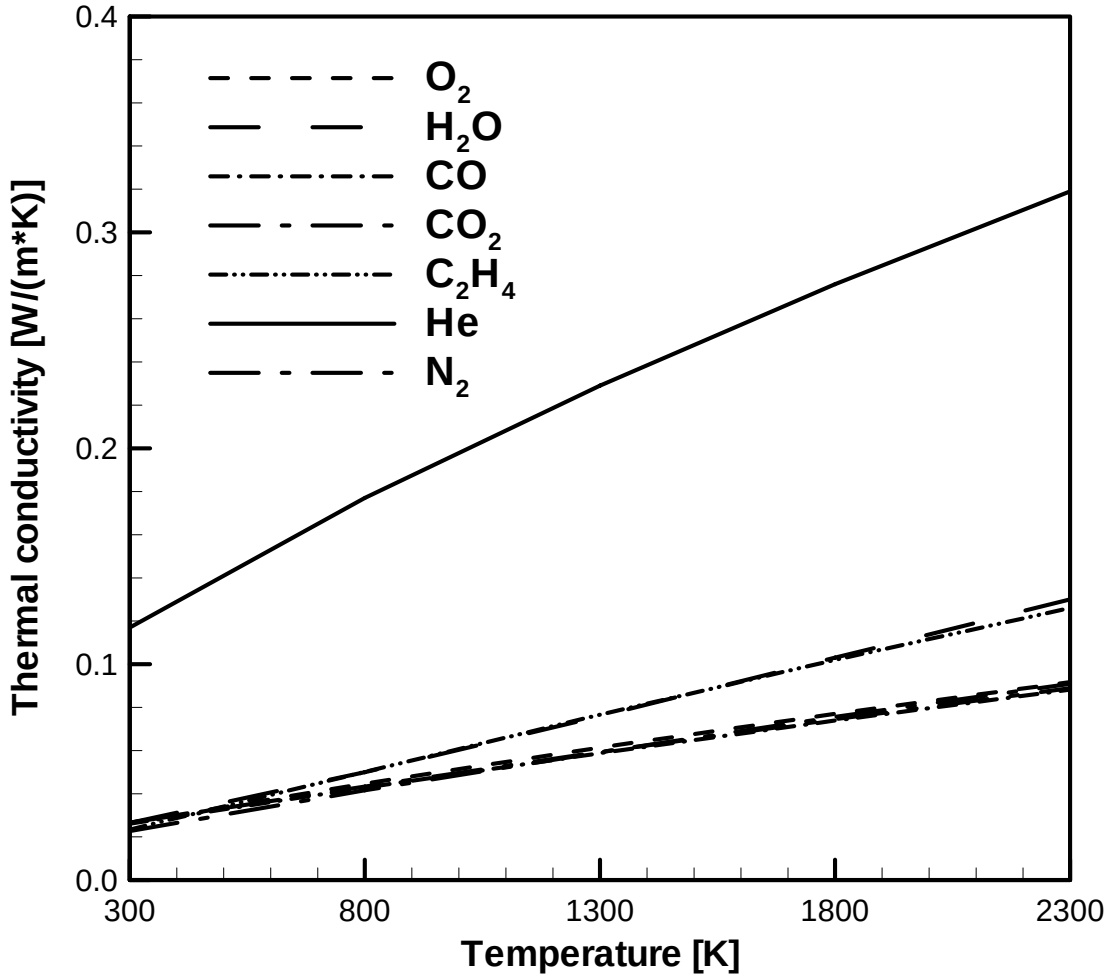

Figure 6.2: Thermal conductivity versus temperature for different species.

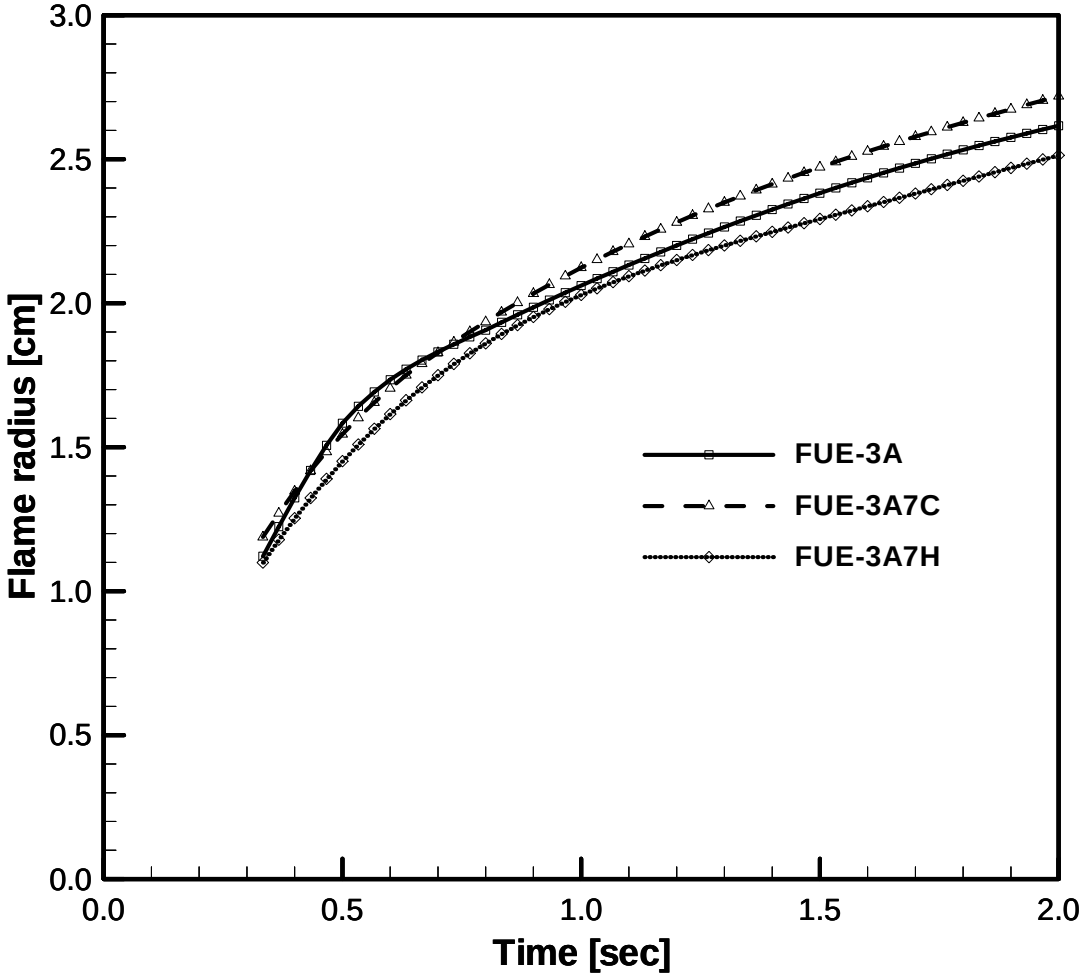

Figure 6.3: Experimental transient flame radius history for different oxidizer-side dilution cases with volume flow rate 6 ml/s.

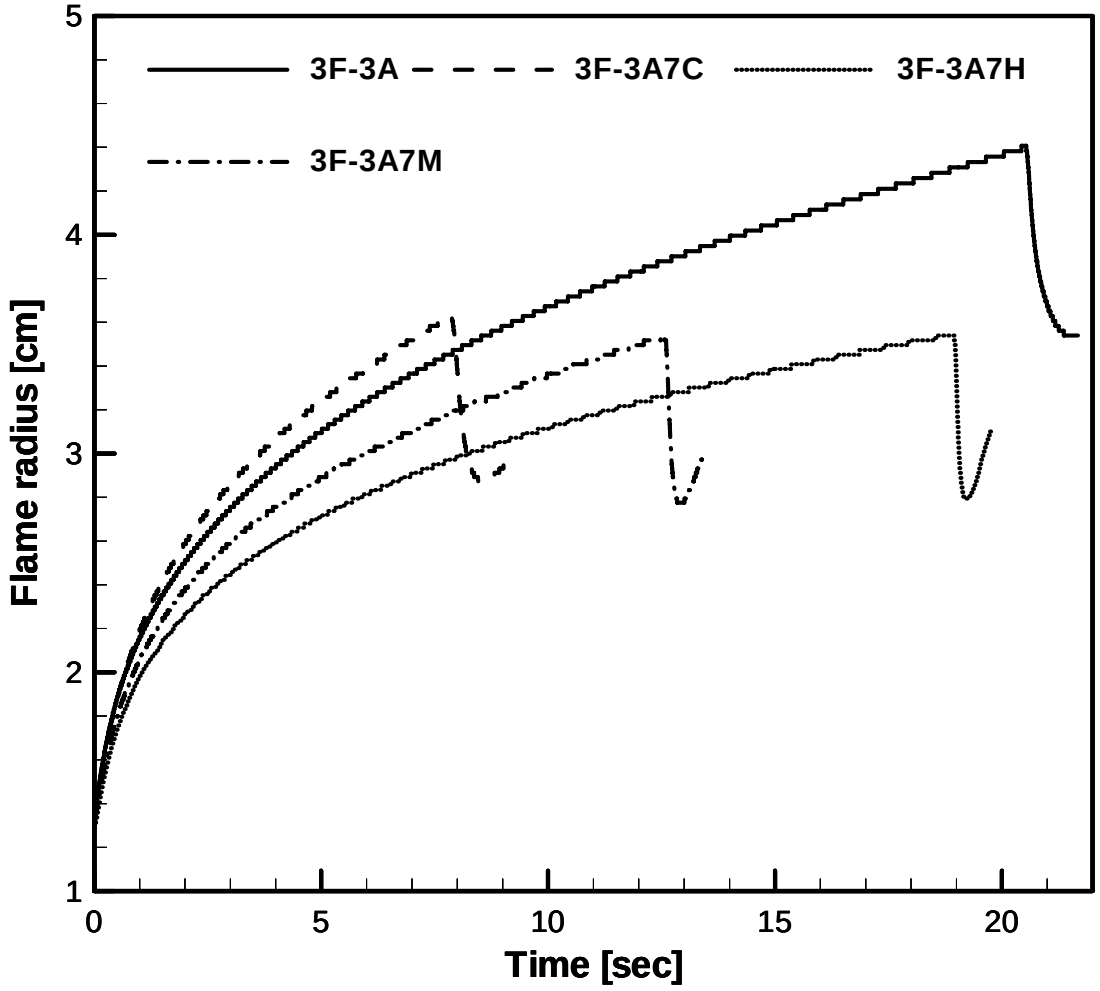

Figure 6.4: Flame radius versus time for different oxidizer-side dilution cases with volume flow rate 12 ml/s.

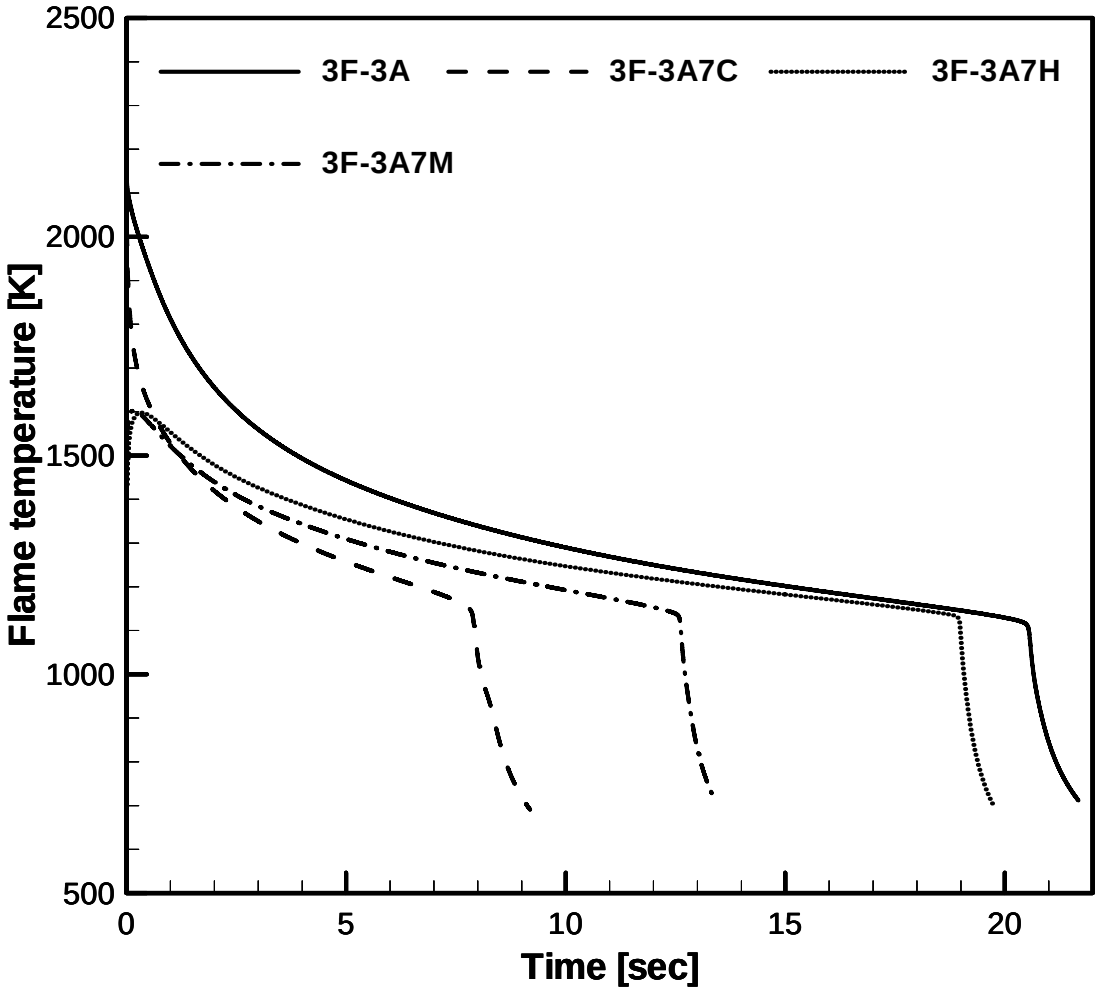

Figure 6.5: Flame temperature versus time for different oxidizer-side dilution cases with volume flow rate 12 ml/s.

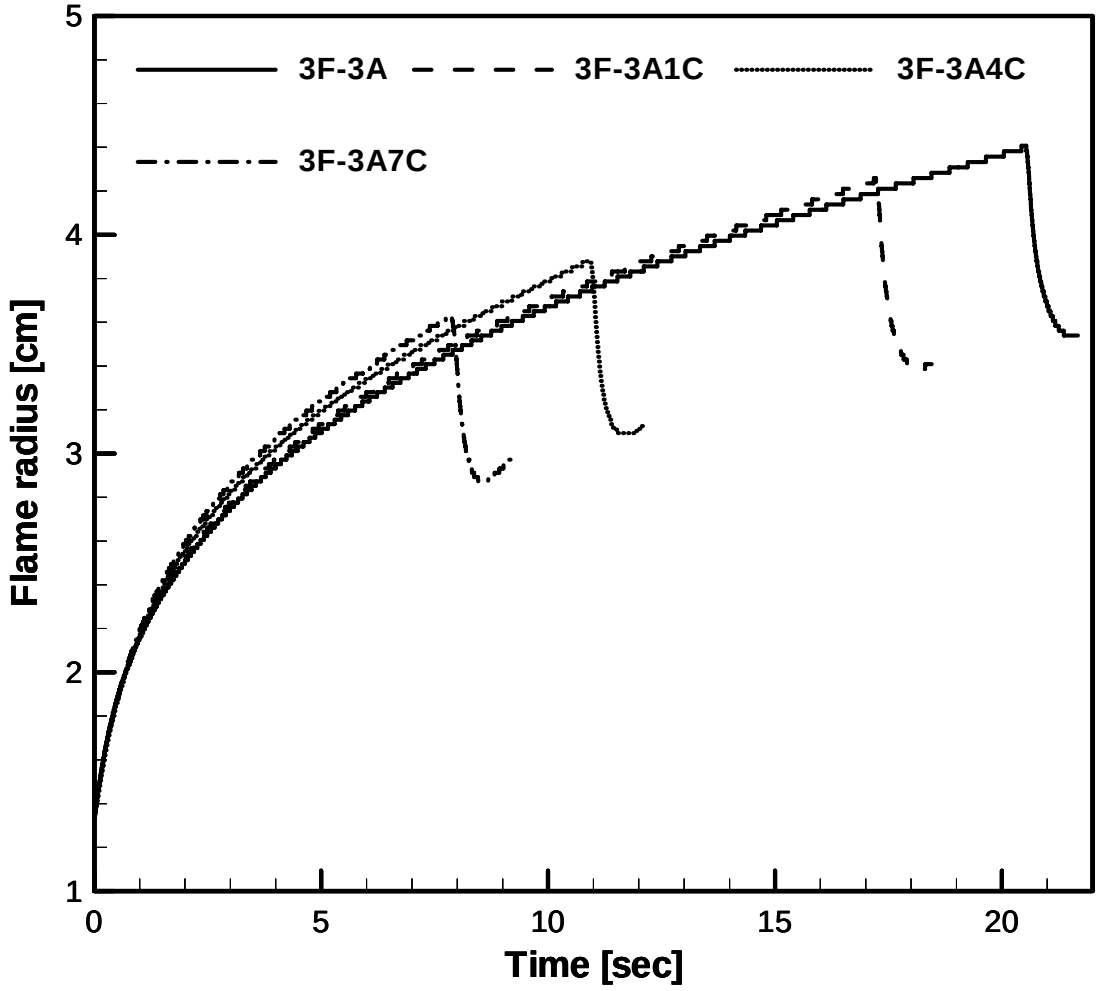

Figure 6.6: Flame radius versus time for different oxidizer-side dilution cases with volume flow rate 12 ml/s.

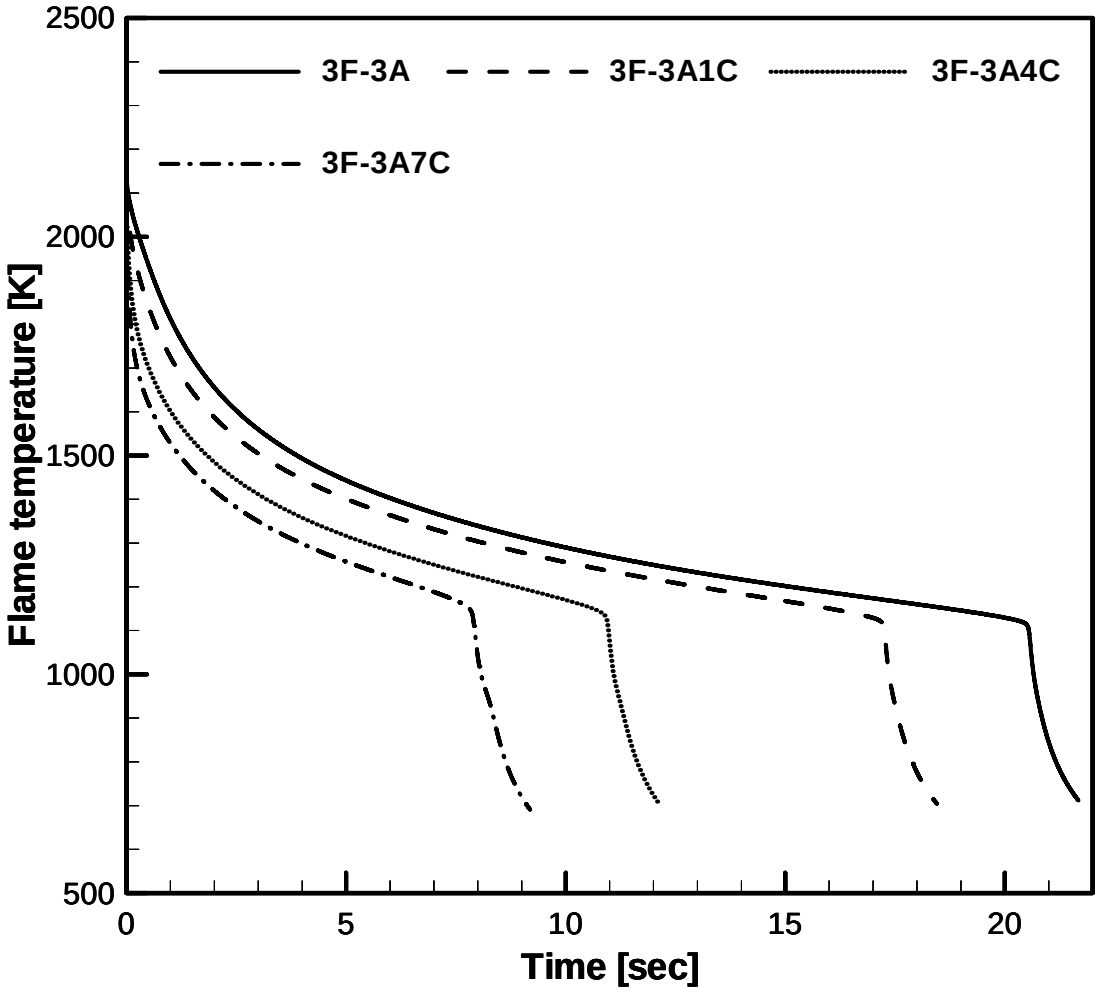

Figure 6.7: Flame temperature versus time for different oxidizer-side dilution cases with volume flow rate 12 ml/s.

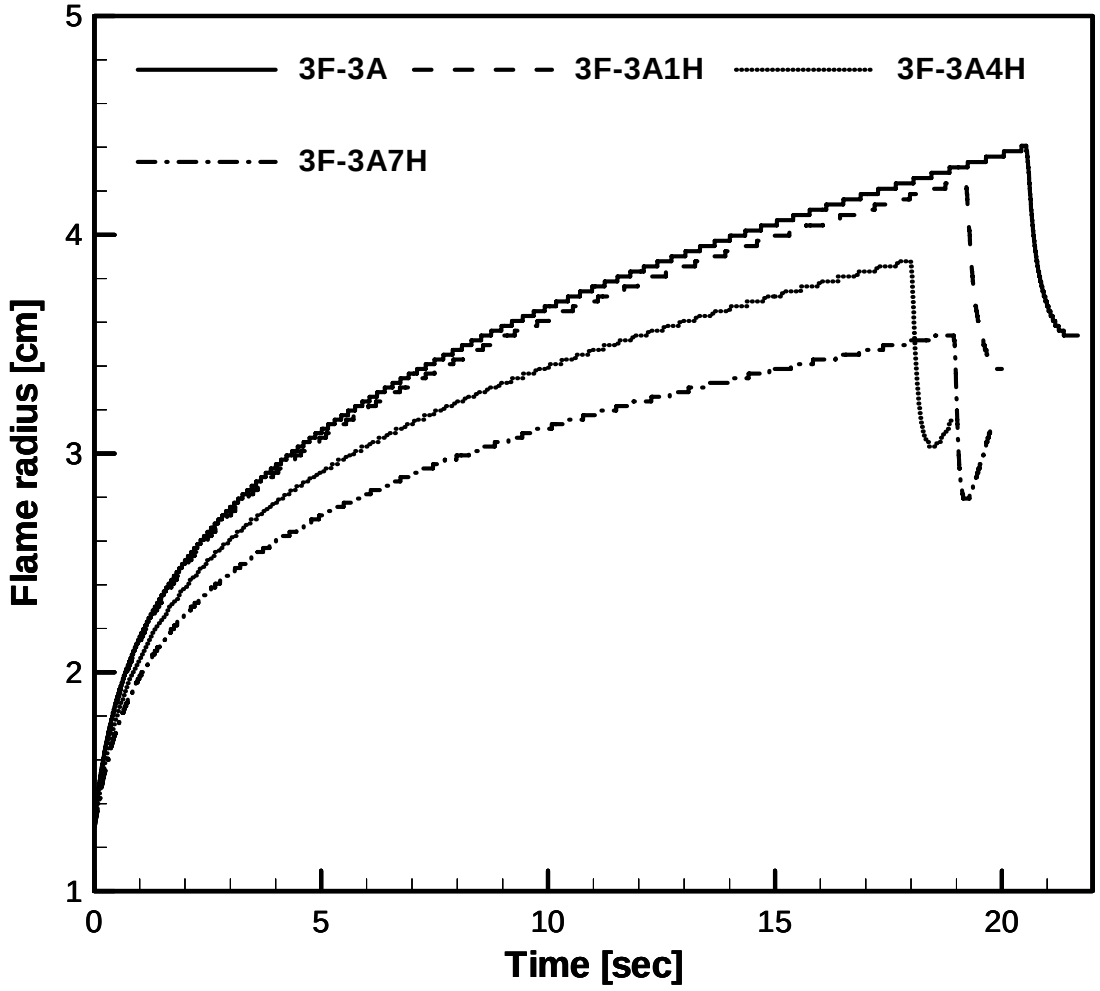

Figure 6.8: Flame radius versus time for different oxidizer-side dilution cases with volume flow rate 12 ml/s.

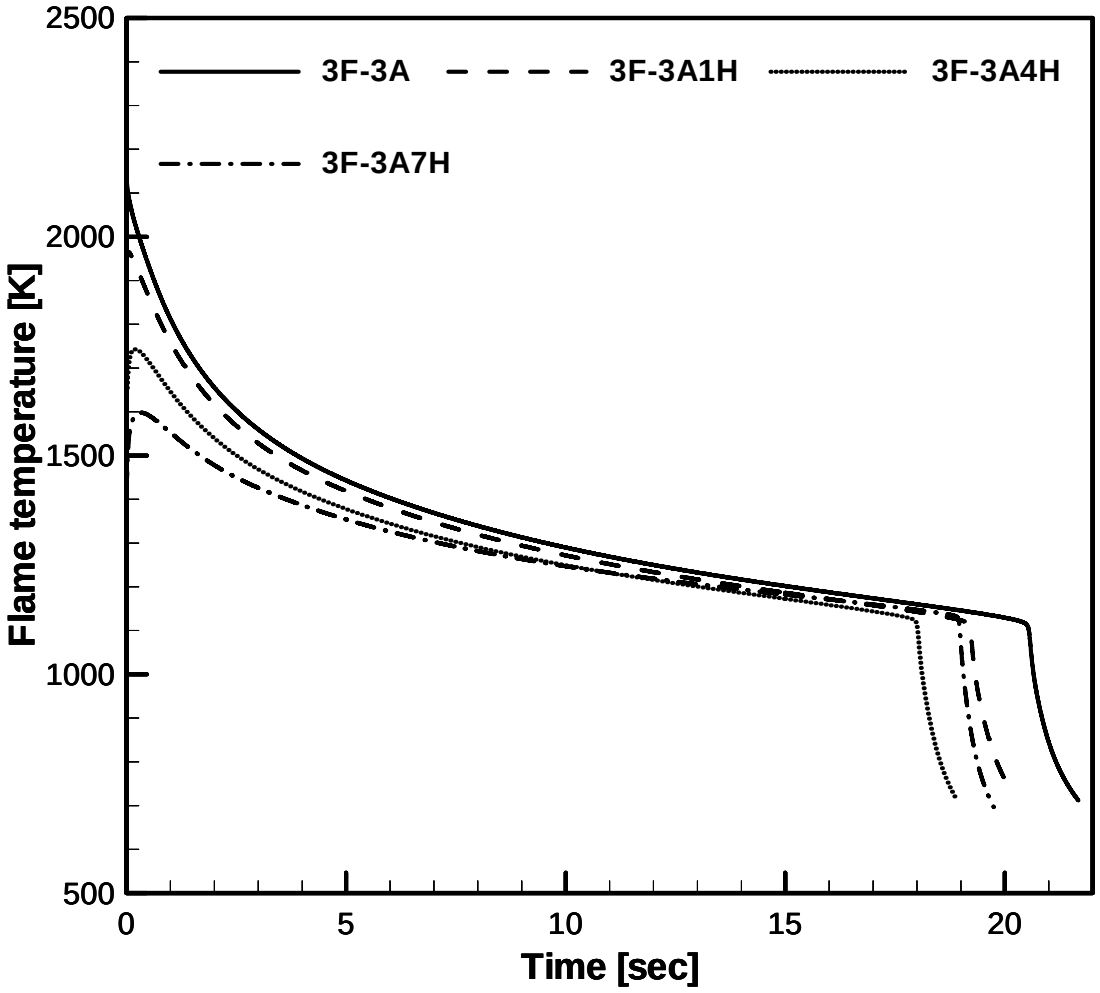

Figure 6.9: Flame temperature versus time for different oxidizer-side dilution cases with volume flow rate 12 ml/s.

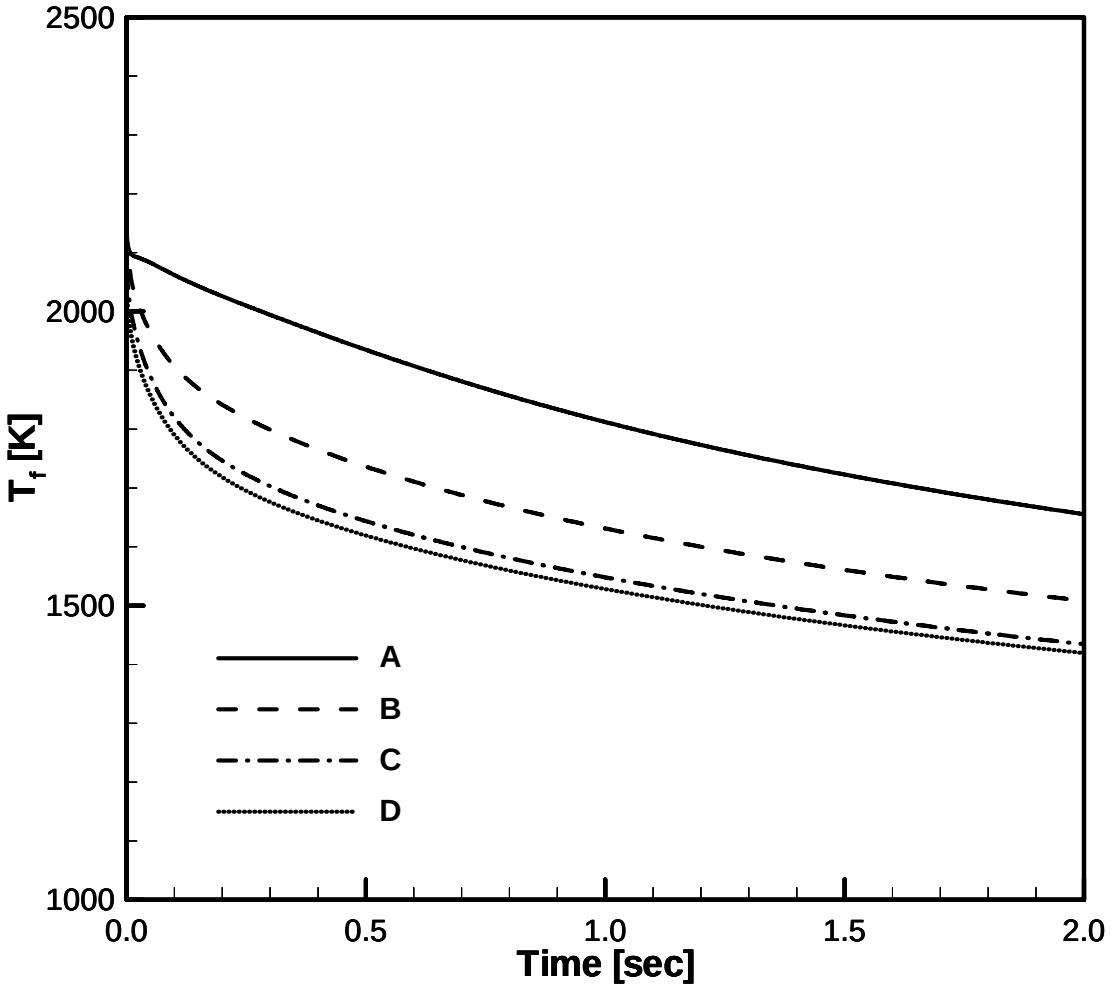

Figure 6.10: Flame temperature versus time for 70% oxidizer-side dilution cases with volume flow rate 12 ml/s.

A: Case 3F-3A, B: Same as Case A but assuming that nitrogen has the same radiation property as CO_2, C: Same as 3F-3A7C but assuming that the diluent CO_2 is inert, D: Case 3F-3A7C.

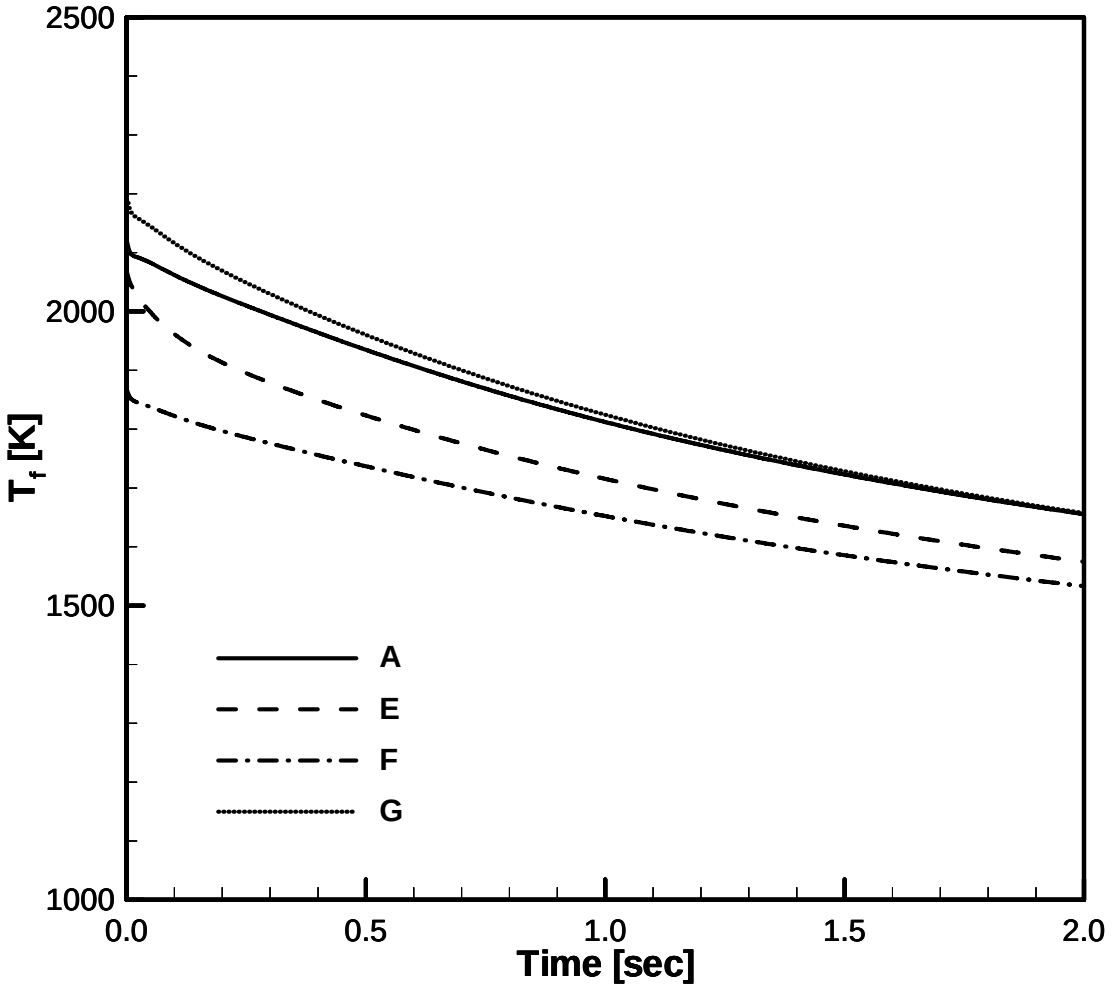

Figure 6.11: Flame temperature versus time for different oxidizer-side dilution cases with volume flow rate 12 ml/s.

A: case 3F-3A; E: modified case from 01 assuming oxidizer-side diluent N_2 has the thermal/transport properties of CO_2; F: modified case from 01 assuming the oxidizer-side diluent N_2 has the thermal property of CO_2; G: modified case from 01 assuming the oxidizer-side diluent N_2 has the transport property of CO_2.

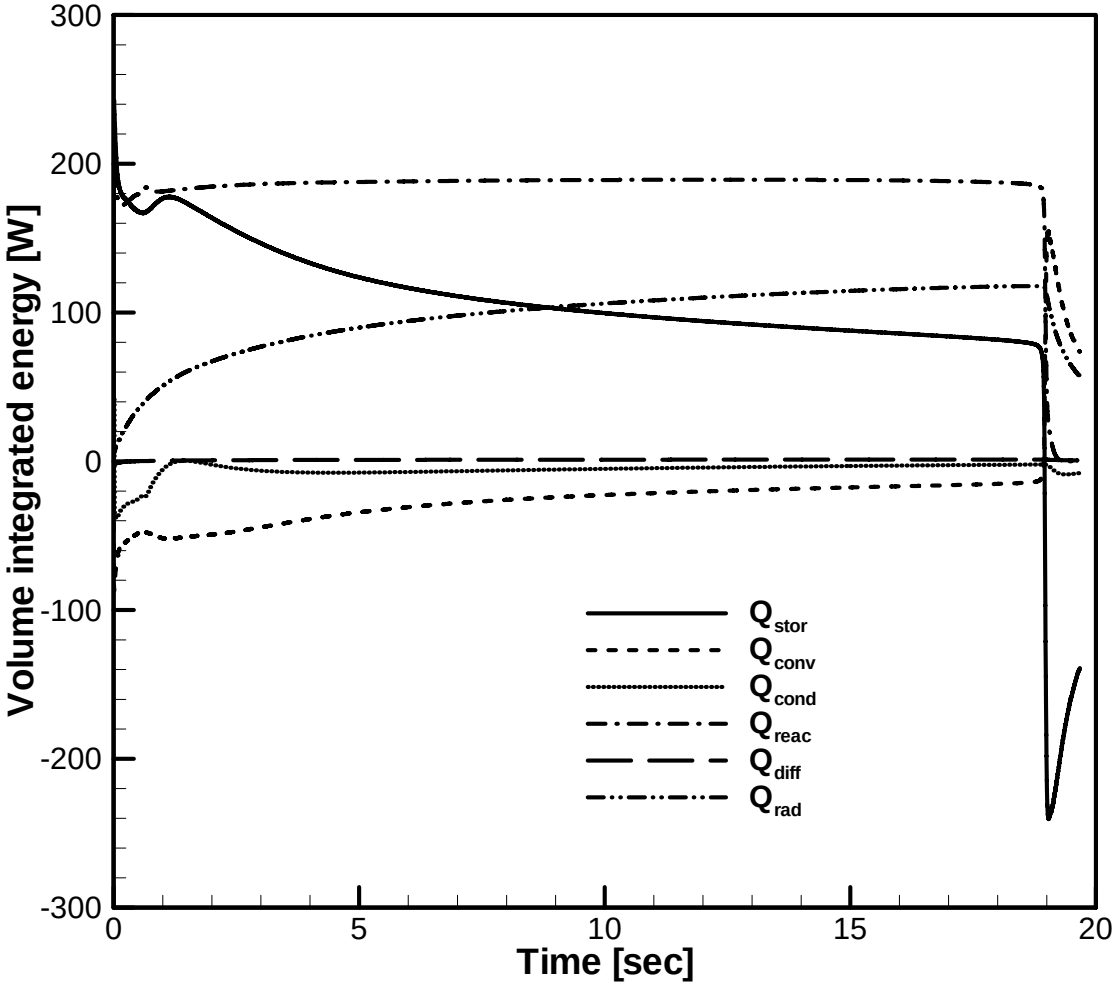

Figure 6.12: Volume-integrated terms in the energy equation versus time for Case 3F-3A7H with volume flow rate 12 ml/s.

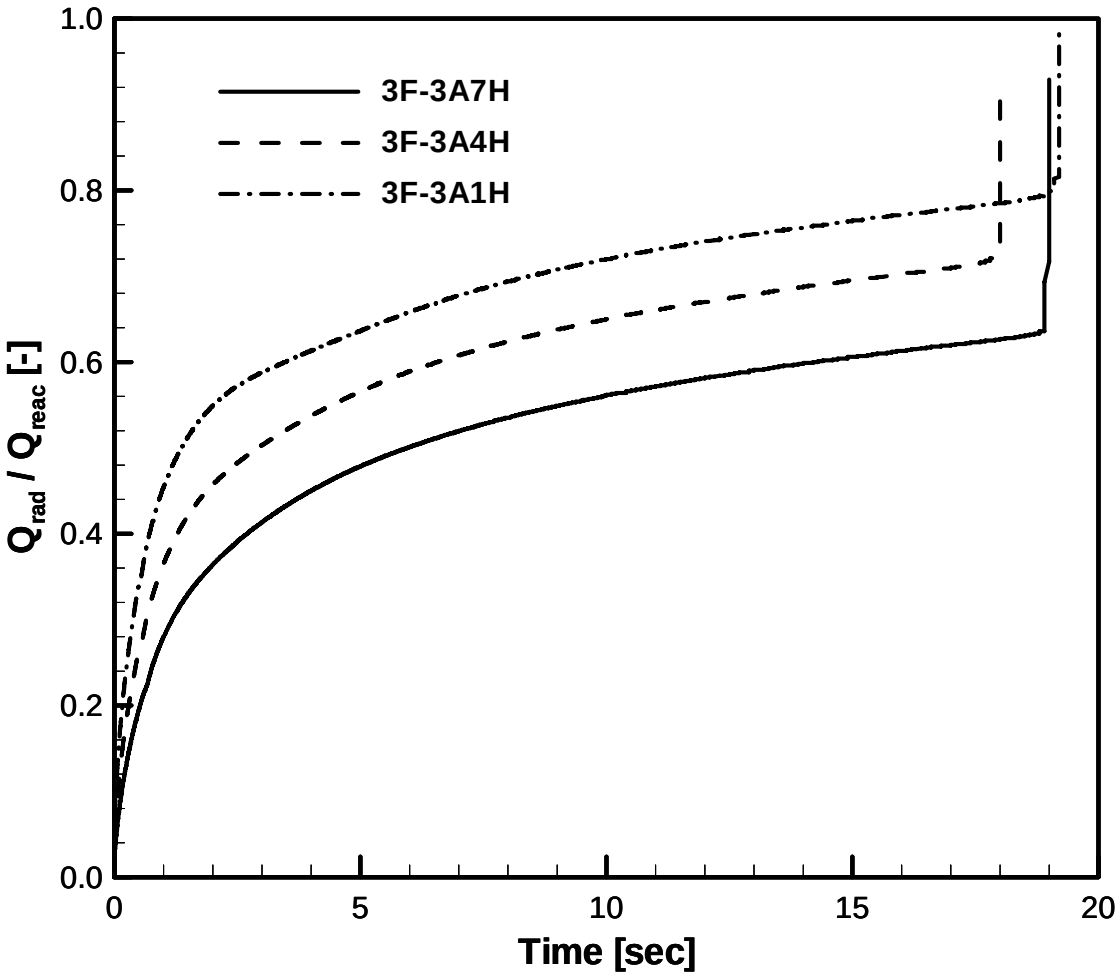

Figure 6.13: Volume integrated energy terms versus time for different oxidizer-side helium dilution cases with volume flow rate 12 ml/s.

non-symbol lines: 3F-3A7H, square symbol lines: 3F-3A4H, triangle symbol lines: 3F-3A1H.

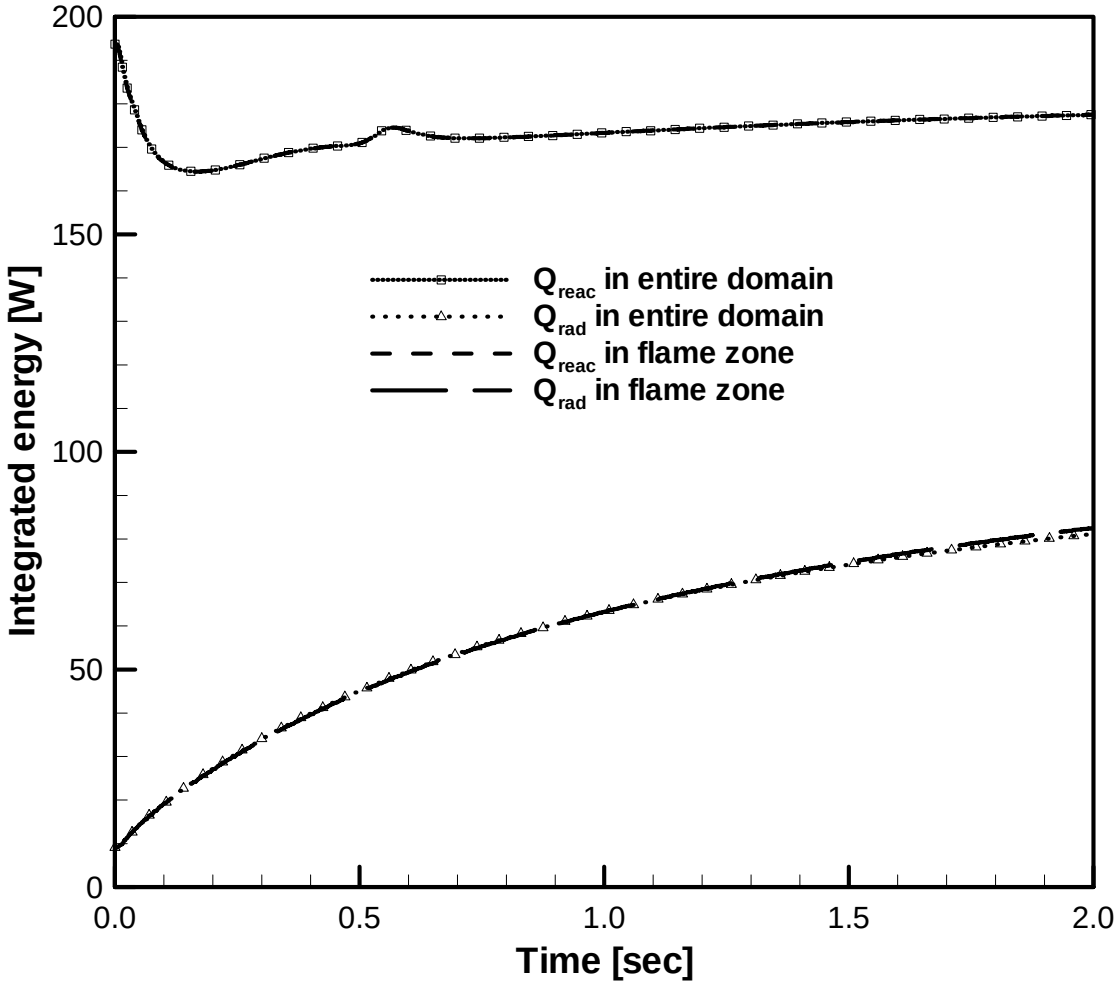

Figure 6.14: Volume-integrated Q_{reac} and Q_{rad} for two different integral volumes, for the 3F-3A4H case with volume flow rate 12 ml/s.

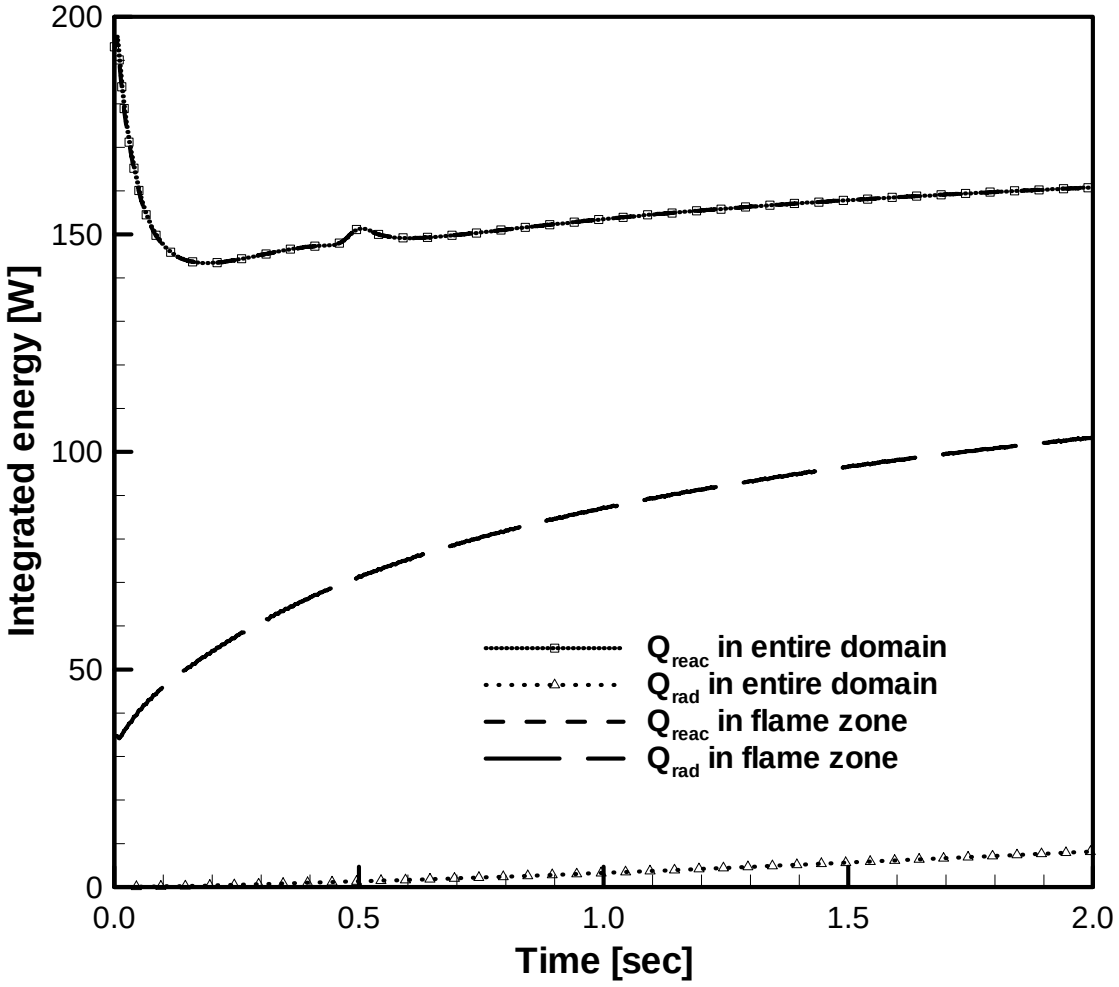

Figure 6.15: Volume-integrated Q_{reac} and Q_{rad} for two different integral volumes, for the 3F-3A4C case with volume flow rate 12 ml/s.

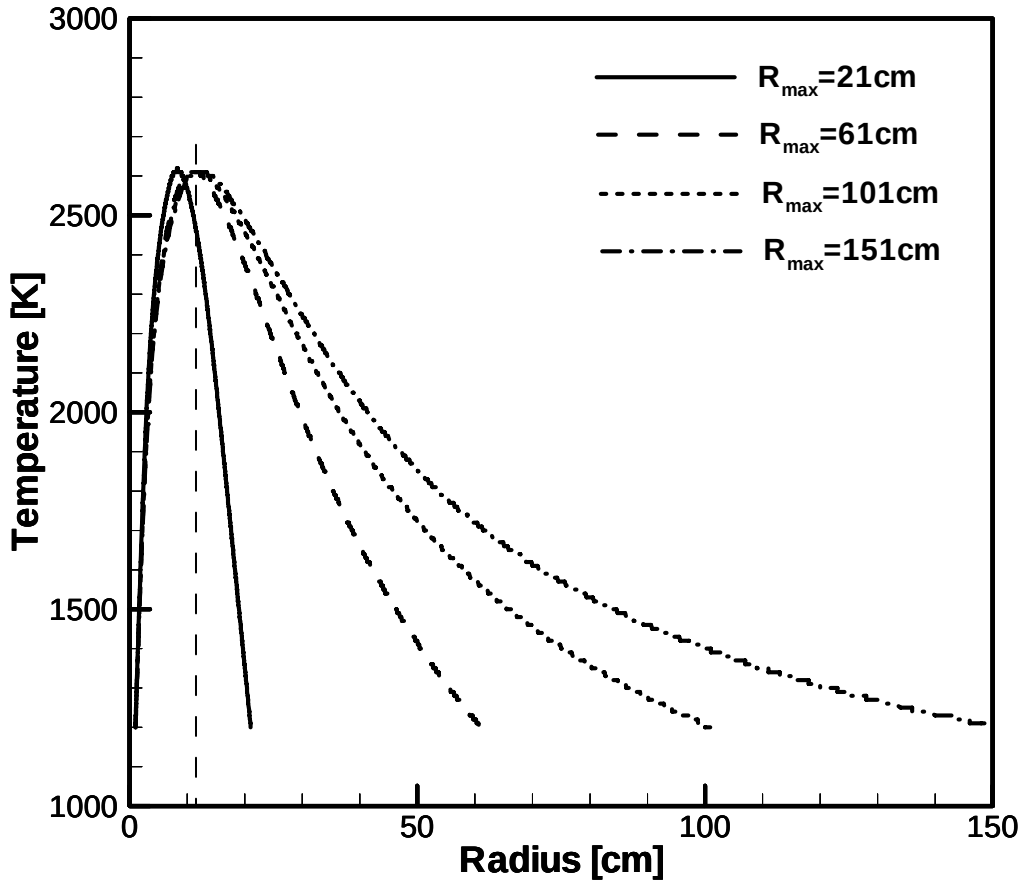

Figure 6.16: Steady solution temperature profile for different domain size options with volume flow rate 6 ml/s.

Chapter 7 Conclusions and Future Work

As part of the NASA funded project, this study presented a computational investigation of the nonpremixed flame extinction characteristics in the presence of radiative heat transfer in microgravity. A one-dimensional spherical diffusion flame was adopted as a model configuration, for which continuity, momentum, energy, and species equations were solved to describe the transient flame evolution. Different radiation property models have been applied including the gray-gas, wide band, and statistical narrow band (SNB) models, while the discrete ordinate method was used to solve the radiation transfer equations. The model was validated against the results from the NASA drop tower experiment, performed by the project group at the University of Michigan, primarily in terms of the flame radius growth rate and the temperature history monitored at various radial locations. The model was then extended to conduct extensive parametric studies to investigate the role of radiation-induced quenching. For various types of diluent gases added to either the fuel or the oxidizer side, their effects on the flame growth, temperature, and quenching characteristics were systematically analyzed.

Major original contributions and scientific findings obtained from the present study can be summarized as follows.

1. The present study provided a comprehensive and consistent comparison of various radiation models in a microgravity combustion problem, where the effects of gas radiation become more pronounced due to the absence of buoyancy-induced flows. The validation was performed by carefully reproducing the experimental data by Atreya and coworkers (Atreya *et al*. 2001, Chernovsky *et al.* 2007), which provided unique data for quantitative measurements of spatially- and temporally-resolved flame radius and temperature information. It was confirmed that a detailed radiation property model at the level of SNB was necessary in order to predict the experimental

results accurately. To our knowledge, this is the first attempt to compare the transient temperature history against direct experimental measurements, with a careful matching of the parameter and boundary conditions within experimental uncertainties.

2. Study on dilution effect on flame behavior showed that oxidizer side dilution results in larger variations of flame radius and temperature behavior than fuel side dilution does. It was concluded that oxidizer-side dilution has a stronger effect on flame transient behavior than fuel-side dilution. This is due to the spherical configuration under study, in which ambient condition significantly controls the fuel-lean side species profiles, while the fuel-rich side species profiles are affected by both fuel-side and oxidizer-side boundary conditions. This finding shows that adding diluent in the ambient environment is more effective on flame behavior control than adding diluent in the fuel supply.
3. Study on various oxidizer-side dilution cases showed that different diluents have different effect on spherical diffusion flame extinction behavior. For the same oxidizer-side volume dilution amount, CO_2 has a suppression effect of around 2.5 as strong as that of helium in terms of flame extinction time. When dilution amount is increased, flame extinction time is reduced greatly for CO_2 dilution cases, but the flame extinction time has limited variation for helium dilution cases. The conclusion is, the diluent becomes more effective on flame extinction in the order of N_2, He, and CO_2.
4. Quantitative analysis of oxidizer-side dilution cases with CO_2 dilution versus nitrogen dilution shows that, CO_2 dilution has multiple effects on flame behavior including radiation effect, thermal/transport effect, and chemical effect. Our study shows that radiation effect is the primary factor accounting for flame temperature drop by around 60%, thermal/transport effect accounts for around 30% of the total CO_2 dilution effect, and chemical effect only accounts for around 10% of it. There are two primary reasons for the dominant effect of radiation over thermal/transport, first the absence of buoyancy-induced flows significantly increases the residence time of gaseous products (CO_2, CO, and H_2O) accumulated in the reaction zone that in turn increases gas radiation from the flame zone, second the low stretch rate in microgravity spherical diffusion flame increases the flame zone thickness which significantly

increases gas radiation due to the increased hot zone volume. To our knowledge, this is the first attempt to quantitatively compare different suppression effects of CO_2 as a fire extinguishing agent.

5. Investigation of the volume integrated reaction heat release and radiation heat loss shows that, although radiation heat loss gradually reduces flame temperature it is not the most important reason accounting for the onset of flame extinction. Although other researchers claim that the ratio of radiation heat loss to the reaction heat release is a constant when flame extinction happens, various cases in our study show a wide range of this ratio, which means the ratio might not be a good criterion for the onset of flame extinction. The computational results show that flame temperature is almost always at 1130 K for different cases in our study when flame extinction happens, which means flame extinction is caused by flame temperature dropping down to the critical temperature and thus chemical reactions are not sustained. Consequently we propose flame temperature as an alternative criterion for the onset of flame extinction.
6. Study on flame ignition behavior for different oxidizer-side dilution cases shows that when helium dilution is applied flame is more difficult to ignite than when CO_2 is imposed. This computation experience is in line with the observation in previous experimental research. This is explained by the relatively larger heat conductivity of helium which helps to take away the heat from the flame zone.
7. Investigation on steady flame solution within different of domain sizes shows that although steady solution can be obtained from numerical calculation, zero gradient is never observed on the outflow boundary even for a domain size as large as 151 cm. It shows that no matter how large a spherical diffusion flame may grow, due to the non-zero gradient of temperature and species fraction on the outflow boundary, the flame always keeps growing although the flame center seems to be stabilized. Considering that gas radiation is inevitable which reduces flame temperature gradually, flame will eventually extinguishes when its temperature drops down to a critical value; therefore, steady state spherical diffusion flames do not exist in microgravity.

The above findings lead to a number of fundamental and practical issues that require additional research efforts. Some possible subjects as an extension of the present work may be listed as follows.

1. For all computational and experimental conditions under consideration in this study, the amount of soot formation was relatively small. For many practical combustion conditions, however, soot formation in nonpremixed flames can be significant. In fact, the spherical diffusion flame configuration is well-suited to investigate the soot effect because the lack of buoyancy-driven flows allows a longer residence time for soot formation (Liu *et al.* 2005). The presence of soot particles in the flame can substantially modify the radiative characteristics and thus can impact the extinction conditions. However, the detailed outcome of the interaction among chemical reactions, gas radiation, soot formation, and soot radiation is still not clearly understood. Therefore, further work is needed to conduct experimental measurements at sooting conditions. To predict these flames computationally, detailed soot formation and radiation models need to be developed at a level of complexity comparable to the gas-phase radiation models.
2. The detailed soot chemistry and radiation models are expected to impose a significant overhead on the computational cost, thereby requiring an additional effort to improve the computational efficiency. While the fixed zonal mesh refinement was sufficient for the present study, implementation of a more advanced adaptive mesh refinement may be needed to achieve a desired level of computational efficiency. This will allow an extensive parametric investigation of soot-radiation interaction through high-fidelity simulations.
3. While the one-dimensional spherical diffusion flame serves as a baseline configuration of the fundamental studies on flame behavior under diffusion-dominant conditions, the knowledge gained from the idealized system can then be extended to include more realistic fluid dynamic effects, such as the buoyancy-driven convective flows. The investigation in this dissertation has provided a good understanding of flame extinction and fire suppression mechanism in microgravity; however, the behavior and mechanism of flame extinction could be very different in Earth's gravity,

and an extended study based on the three-dimensional model will significantly improve our understanding and ability of fire safety control in Earth's gravity.

Bibliography

M. Abid, M. S. Wu, J. B. Liu, P. D. Ronney, M. Ueki, K. Maruta, H. Kobayashi, T. Niioka, and D. M. Vanzandt, "Experimental and numerical study of flame ball IR and UV emissions", Combustion and Flame, Vol. 116, P. 348-359, 1999.

F. M. B. Andersen, "Geometric mean beam lengths between two concentric spheres", ASME Journal of Heat Transfer, Vol. 119, P. 379-380, 1964.

A. Atreya, S. Agrawal, K. R. Sacksteder, and H. R. Baum, "Observations of methane and ethylene diffusion flames stabilized around a blowing porous sphere under microgravity conditions", 32nd Aerospace Sciences Meeting & Exhibit, AIAA, Washington, DC, P. 1-10, 1994.

A. Atreya, S. Agrawal, T. Shamim, K. Pickett, K. R. Sacksteder and H. R. Baum, "Radiant extinction of gaseous diffusion flames", Third International Microgravity Combustion Workshop, Cleveland, P. 319-325, 1995.

A. Atreya and S. Agrawal, "Effect of radiative heat loss on diffusion flames in quiescent microgravity atmosphere", Combustion and Flame, Vol. 115, P. 372-382, 1998.

A. Atreya, S. Berhan, M. Chernovsky, and K. R. Sacksteder, "Unsteady spherical diffusion flames in microgravity", Sixth International Microgravity Combustion Workshop, Cleveland, P. 113-116, 2001.

G. Balakrishnan, M. D. Smooke, and F. A. Williams, "A numerical investigation of extinction and ignition limits in laminar nonpremixed counterflowing hydrogen-air streams for both elementary and reduced chemistry", Combustion and Flame, Vol. 102, P. 329-340, 1995.

R. S. Barlow, A. N. Karpetis, J. H. Frank, and J. Y. Chen, "Scalar profiles and NO formation in laminar opposed-flow partially premixed methane/air flames", Combustion and Flame, Vol. 127, P. 2102-2118, 2001.

B. Bedat and R. K. Cheng, "Effects of buoyancy on premixed flame stabilization", Combustion and Flame, Vol. 107, P. 13-26, 1996.

J. G. Blom, J. M. Sanz-Serna, and J. G. Verwer, "On simple moving grid methods for one-dimensional evolutionary partial differential equations", Journal of Computational Physics, Vol. 74, P. 191-213, 1988.

J. Buckmaster and G. Joulin, "Radial propagation of premixed flames and [illegible]behavior", Combustion and Flame, Vol. 78, P. 275-286, 1989.

J. Buckmaster, G. Joulin, and P. Ronney, "The structure and stability of nonadiabatic flame balls", Combustion and Flame, Vol. 79, P. 381-392, 1990.

J. Buckmaster, G. Joulin, and P. Ronney, "The structure and stability of nonadiabatic flame balls: II. Effects of far-field losses", Combustion and Flame, Vol. 84, P. 411-422, 1991.

B. G. Carlson, and K. D. Lathrop, "Transport theory-the method of discrete ordinates", in Computing Methods in Reactor Physics, eds. H. Greenspan, C. N. Kelber, and D. Okrent, Gordon & Breach, New York, 1968.

S. Chandrasekhar, "Radiative Transfer", Dover Publications, 1960.

P. Cheng, "Study of the flow of a radiating gas by a differential approximation", Ph.D. thesis, Standford University, Standford, CA, 1965.

P. Cheng, "Dynamics of a radiating as with application to flow over a wavy wall", AIAA Journal, Vol. 4, P. 238-245, 1966.

M. K. Chernovsky, "An experimental study of temperature and radiation characteristics of transient spherical diffusion flames in microgravity", Ph.D. thesis, the University of Michigan, Ann Arbor, MI, 2006.

M. K. Chernovsky, A. Atreya, and H. G. Im, "Effect of CO_2 diluent on fuel versus oxidizer side of spherical diffusion flames in microgravity", Proceedings of the Combustion Institute, Vol. 31, P. 1005-1013, 2007.

P. J. Coelho, "Detailed numerical simulation of radiative transfer in a nonluminous turbulent jet diffusion flame", Combustion and Flame, Vol. 136, P. 481-492, 2004.

T. P. Coffee and J. M. Heimerl, "Transport algorithms for premixed, laminar steady-state flames", Combustion and Flame, Vol. 43, P. 273-289, 1981.

B. Davison, "Neutron Transport Theory", Oxford University Press, London, 1958.

A. B. De Miranda and J. F. Sacadura, "An alternative formulation of the S-N discrete ordinates for predicting radiative transfer in nongray gases", Journal of Heat Transfer, Vol. 118, P. 650-653, 1996.

M. K. Denison and B. W. Webb, "A spectral line-based weighted-sum-of-gray-gases model for arbitrary RTE solvers", ASME Journal of Heat Transfer, Vol. 115, P. 1004-1012, 1993.

M. K. Denison and B. W. Webb, "The spectral line-based weighted-sum-of-gray-gases model in non-isothermal non-homogeneous media", ASME Journal of Heat Transfer, Vol. 117, P. 359-365, 1995.

D. K. Edwards, and W. A. Menard, "Comparison of models for correlation of total band absorption", Applied Optics, Vol. 3, P. 621-624, 1964.

D. K. Edwards, L. K. Glassen, W. C. Hauser, and J. S. Tuchscher, "Radiation heat transfer in nonisothermal nongray gases", ASME Journal of Heat Transfer, Vol. 89, P. 219-229, 1967.

D. K. Edwards, “Molecular gas band radiation”, in: Advances in theat transfer, Vol. 12, p. 115-193, Academic Press, New York, 1976.

O. A. Ezekoye and Z. Zhang, “Soot oxidation and agglomeration modeling in a microgravity diffusion flame”, Combustion and Flame, vol. 110, P. 127-139, 1997.

A. Fiterman, R. Ben-Zvi, and A. Kribus, “DOTS: Pseudo-time-stepping solution of the iscrete ordinate equations”, Numerical Heat Transfer, Part B, Vol. 35, P. 163-183, 1999.

W. A. Fiveland, “Discrete ordinate methods for radiative heat transfer in isotropically and anisotropically scattering media”, ASME Journal of Heat Transfer, Vol. 109, P. 809-812, 1987.

R. M. Goody, “A statistical model for water-vapour absorption”, Quarterly Journal of Royal Meteorological Society, Vol. 78, P. 165-169, 1952.

R. Goody, R. West, L. Chen, and D. Crisp, “The correlated-k method for radiation calculations in nonhomogeneous atmospheres”, Journal of Quantitative Spectroscopy and Radiative Transfer, Vol. 42, P. 539–550, 1989.

R. M. Goody and Y. L. Yung, “Atmospheric Radiation: Theoretical Basis”, New York : Oxford University Press, 2nd ed., 1989.

V. Gopalakrishnan and J. Abraham, “Effects of multicomponent diffusion on predicted ignition characteristics of an *n*-heptane diffusion flame”, Combustion and Flame, Vol. 136, P. 557-566, 2004.

J. F. Grcar, “The Twopnt program for boundary value problems”, Sandia National Laboratories Report SAND91-8230, 1992.

W. L. Grosshandler, “RADCAL. A Narrow-Band Model for Radiation Calculations in a Combustion Environment”, NIST Technical Note 1402, 1993.

H. Guo, Y. Ju, K. Maruta, T. Niioka, and F. Liu, “Radiation extinction limit of counterflow premixed lean methane-air flames”, Combustion and Flame, Vol. 109, P. 639-646, 1997.

J.-M. Hartmann, R. Levi Di Leon, and J. Taine, “Line-by-line and narrow-band statistical model calculations for H2O”, Journal of Quantitative Spectroscopy and Radiative Transfer, Vol. 32, No. 2, P. 119-127, 1984.

J. M. Heimerl and T. P. Coffee, “Transport algorithms for methane flames”, Combustion Science and Technology, Vol. 34, P. 31-43, 1983.

H. C. Hottel, A. F. Sarofim, L. B. Evans, and I. A. Vasalos, “Radiative transfer in anisotropically scattering media: Allowance for Fresnel reflection at the boundaries”, ASME Journal of Heat Transfer, Vol. 90, P. 56-62, 1968.

H. M. Hsia, and T. J. Love, “Radiative heat transfer between parallel plates separated by a nonisothermal medium with anisotropic scattering”, ASME Journal of Heat Transfer, Vol. 89, P. 197-204, 1967.

J. M. Hyman, S. Li, and L. R. Petzold, “An adaptive moving mesh method with static rezoning for partial differential equations”, Computers and Mathematics with Applications, Vol. 46, P. 1511-1524, 2003.

A. F. Ibarreta, C. J. Sung, T. Hirasawa, and H. Wang, “Burning velocity measurements of microgravity spherical sooting premixed flames using rainbow SCHLIEREN deflectometry”, Combustion and Flame, Vol. 140, P. 93-102, 2005.

J. H. Jeans, “The equations of radiative tansfer of energy”, Monthly Notices Royal Astronomical Society, Vol. 78, P. 28-36, 1917.

B. Konsur, C. M. Megaridis, and D. W. Griffin, “Soot aerosol properties in laminar soot-emitting microgravity nonpremixed flames”, Combustion and Flames, Vol. 118, P. 509-520, 1999.

Y. Ju, G. Masuya, P. D. Ronney, “Effects of radiative emission and absorption on the propagation and extinction of premixed gas flames”, 27th Symposium (International) on Combustion, P. 2619-2626, 1998.

Y. Ju, H. Matsumi, K. Takita, and G. Masuya, “Combined effects of radiation, flame curvature, and stretch on the extinction and bifurcations of cylindrical CH_4/air premixed flame”, Combustion and Flame, Vol. 116, P. 580-592, 1999.

V. R. Katta, F. Takahashi, and G. T. Linteris, “Suppression of cup-burner flames using carbon dioxide in microgravity”, Combustion and Flame, Vol. 137, Pl. 506-522, 2004.

V. R. Katta, F. Takahashi, and G. T. Linteris, “Fire-suppression characteristics of CF_3H in a cup burner”, Combustion and Flame, Vol. 144, P. 645-661, 2006.

R. J. Kee, J. A. Miller, and T. H. Jefferson, “Chemkin: A general-purpose, problem-independent, transportable, Fortran chemical kinetics code package”, Sandia National Laboratories Report SAND80-8003, 1980.

R. J. Kee, J. Warnatz, and J. A. Miller, “A Fortran computer code package for the evaluation of gas-phase viscosities, conductivities, and diffusion coefficients”, Sandia National Laboratories Report SAND83-8209, 1983.

R. J. Kee, F. M. Rupley, and J. A. Miller, “Chemkin-II: A Fortran chemical kinetics package for the analysis of gas-phase chemical kinetics”, Sandia National Laboratories Report SAND89-8009, 1990.

T. K. Kim, J. A. Menart, and H. S. Lee, “Nongray radiative gas analyses using the S-N discrete ordinates method”, Journal of Heat Transfer, Vol. 113, P. 946-952, 1991.

K. K. Kuo, “Principles of combustion”, 2nd ed., John Wiley & Sons, Inc., Hoboken, New Jersey, P. 285-327, 2005.

N. Lallemant and R. Weber, “A computationally efficient procedure for calculating gas radiative properties using the exponential wide band model”, International Journal of Heat and Mass Transfer, Vol. 39, P. 3273-3286, 1996.

K. D. Lathrop, “Use of discrete-ordinate methods for solution of photon transport problems”, Nuclear Science and Engineering, Vol. 24, P. 381-388, 1966.

C. K. Law, “Combustion physics”, Cambridge University Press, New York, NY, 2006.

C. E. Lee, “The discrete S_n approximation to transport theory”, Technical Information Series Report LA2595, Lawrence Livermore Laboratory, 1962.

C. E. Lee, S. R. Lee, J. W. Han, and J. Park, “Numerical study on effect of CO_2 addition in flame structure and NO_x formation of CH_4-air counterflow diffusion flames”, International Journal of Energy Research, Vol. 25, P. 343-354, 2001.

S. Li, L. Petzold, and Y. Ren, “Stability of Moving Mesh Systems of Partial Differential Equations”, SIAM Journal on Scientific Computing, Vol. 20, P. 719-738, 1998.

F. Liu, H. Guo, and G. J. Smallwood, “Effects of radiation model on the modeling of a laminar coflow methane/air diffusion flame”, Combustion and Flame, Vol. 138, P. 136-154, 2004.

F. Liu, H. Guo, G. J. Smallwood, and O. L. Gulder, “The chemical effects of carbon dioxide as an additive in an ethylene diffusion flame: Implications for soot and NOx formation”, Combustion and Flame, Vol. 125, P. 778-787, 2001.

F. Liu, O. L. Gulder, and G. J. Smallwood, “Non-grey gas radiative transfer analyses using the statistical narrow-band model”, International Journal of Heat and Mass Transfer, Vol. 41, P. 2227-2236, 1998.

J. Liu, H. M. Shang, Y. S. Chen, and T. S. Wang, “Analysis of discrete ordinates method with even parity formulation (in radiative heat transfer)”, AIAA 31st Thermophysics Conference, New Orleans, LA, 1996.

L. H. Liu, L. M. Ruan, H. P. Tan, “On the discrete ordinates method for radiative heat transfer in anisotropically scattering media”, International Journal of Heat and Mass Transfer, Vol. 45, P. 3259-3262, 2002.

S. Liu, B. H. Chao, and R. L. Axelbaum, “A theoretical study on soot inception in spherical burner-stabilized diffusion flames”, Combustion and Flame, Vol. 140, P. 1-23, 2005.

A. Lock, S. K. Aggarwal, I. K. Puri, and U. Hegde, “Suppression of fuel and air steram diluted methane-air partially premixed flames in normal and microgravity”, Fire Safety Journal, Vol. 43, P. 24-35, 2008.

F. C. Lockwood and N. G. Shah, “A new radiation solution method for incorporation in general combustion prediction procedures”, 18th Symposium (International) on Combustion, P. 1405-1414, 1981.

T. J. Love, and R. J. Grosh, “Radiative heat transfer in absorbing, emitting, and scattering media”, ASME Journal of Heat Transfer, Vol. 87, P. 161-166, 1965.

D. Lozinski, J. Buckmaster, and P. D. Ronney, “Absolute flammability limits and flame-balls”, Combustion and Flame, Vol. 97, P. 301-316, 1994.

W. Malkmus, “Random Lorentz band model with exponential-tailed S^{-1} line-intensity distribution function”, Journal of the Optical Society of America, Vol. 57, P. 323-329, 1967.

M. F. Modest, “Radiative Heat Transfer”, Academic Press, San Diego, CA, 2003 (2nd ed.).

R. L. Murray, “Nuclear Reactor Physics”, Prentice Hall, Englewood Cliffs, NJ, 1957.

K. Nakabe, K. B. McGrattan, T. Kashiwagi, H. R. Baum, H. Yamashita, and G. Kushida, “Ignition and transition to flame spread over a thermally thin cellulosic sheet in a microgravity environment”, Combustion and Flame, Vol. 98, P. 361-374, 1994.

J. Park, D-J Hwang, J-G Choi, K-M Lee, S-I Keel, and S-H Shim, “Chemical effects of CO_2 addition to oxidizer and fuel streams on flame strucrture in H_2-O_2 counterflow diffusion flames”, Internal Journal of Energy Research, Vol. 27, P. 1205-1220, 2003.

J. G. Parker, “Rotational and Vibrational Relaxation in Diatomic Gases”, Physics of Fluids, Vol. 2, P. 449-462, 1959.

S. S. Penner, “Quantitative Molecular Spectroscopy and Gas Emissivities”, Addison Wesley, Reading, MA, 1959.

L. R. Petzold, “A description of DASSL: A differential/algebraic system solver, in scientific computing”, Stepleman, R. S. *et al*. (Eds.), North-Holland, Amsterdam, P. 65-68, 1983.

Ph. Riviere, D. Scutaru, A. Soufiani, and J. Taine, “A new CK data base sitable from 300 K to 2500 K for spectrally correlated radiative transfer in CO_2-H_2O-transparent gas mixtures”, In Proceedings of the 10th International Heat Transfer Conference, RC 24, Bristol, USA, 1994.

P. D. Ronney, “Effect of gravity on laminar premixed gas combustion II: Ignition and extinction phenomena”, Combustion and Flame, Vol. 62, P. 121-133, 1985.

P. D. Ronney and H. Y. Wachman, “Effect of gravity on laminar premixed gas combustion I: Flammability limits and burning velocities”, Combustion and Flame, Vol. 62, P. 107-119, 1985.

P. D. Ronney, “Near-limit flame structures at low Lewis number”, Combustion and Flame, Vol. 80, P. 1-14, 1990.

P. D. Ronney, http://ronney.usc.edu/spreadsheets/, 2003.

L. S. Rothman, R. R. Gamache, R. H. Tipping, C. P. Rinsland, M. A. H. Smith, D. C. Benner, V. M. Devi, J.-M. Flaud, C. Camy-Peyret, A. Perrin, A. Goldman, S. T. Massie, L. R. Brown, and R. A. Toth: “The HITRAN molecular database: Editions of 1991 and 1992”, Journal of Quantitative Spectroscopy and Radiative Transfer, Vol. 48, No. 5/6, P. 469-507, 1992.

L. S. Rothman, C. P. Rinsland, A. Goldman, S. T. Massie, D. P. Edwards, J.-M. Flaud, A. Perrin, C. Camy-Peyret, V. Dana, J.-Y. Mandin, J. Schroeder, A. McCann, R. R. Gamache, R. B. Wattson, K. Yoshino, K. V. Chance, K. W. Jucks, L. R. Brown, V. Nemtchinov, and P. Varanasi: “The HITRAN molecular spectroscopic database and HAWKS (HITRAN atmospheric workstation) 1996 edition”, Journal of Quantitative Spectroscopy and Radiative Transfer, Vol. 60, P. 665-710, 1998.

J. Ruan, H. Kobayashi, T. Niioka, and Y. Ju, "Combined effects of nongray radiation and pressure on premixed $CH_4/O_2/CO_2$ flames", Combustion and Flame, Vol. 124, P. 225-230, 2001.

R. Sankaran, and H. G. Im, "Dynamic flammability limits of methane-air premixed flames with mixture composition fluctuations", Proceedings of the Combustion Institute, Vol. 29, P. 77-84, 2002.

K. J. Santa, B. H. Chao, P. B. Sunderland, D. L. Urban, D. P. Stocker, and R. L. Axelbaum, "Radiative extinctin of gaseous spherical diffusion flames in microgravity", 5th US Combustion Meeting, San Diego, CA, 2007.

K. J. Santa, B. H. Chao, P. B. Sunderland, D. L. Urban, D. P. Stocker, and R. L. Axelbaum, "Radiative extinctin of gaseous spherical diffusion flames in microgravity", Combustion and Flame, Vol. 151, P. 665-675, 2007.

J. M. Sanz-Serna and I. Christie, "A simple adaptive technique for nonlinear wave problems", Journal of Computational Physics, Vol. 67, P. 348-360, 1986.

R. Siegel and J. R. Howell, "Thermal Radiation Heat Transfer", 3rd ed., Hemisphere, Washington, 1992.

Y. Son, G. Zouein, S. Gokoglu, and P. D. Ronney, "Comparison of carbon dioxide and helium as fire extinguishing agents for spacecraft", Journal of ASTM International, Vol. 3, P. 1-6, 2006.

A. Soufiani and J. Taine, "High temperature gas radiative property parameters of statistical narrow-band model for H_2O, CO_2 and CO, and correlated-K model for H_2O and CO_2", International Journal of Heat and Mass Transfer, Vol. 40, P. 987-991, 1997.

P. B. Sunderland, R. L. Axelbaum, D. L. Urban, B. H. Chao, and S. Liu, "Effects of structure and hydrodynamics on the sooting behavior of spherical microgravity diffusion flames", Combustion and Flame, Vol. 132, P. 25-33, 2003.

P. B. Sunderland, J. L. Taylor, K. J. Santa, B. H. Chao, D. L. Urban, D. P. Stocker, and R. L. Axelbaum, "Extinction of normal and inverse spherical diffusion flames in microgravity", Proceedings of the Joint Meeting of the U.S. Sections of the Combustion Institute, Philadephia, 2005.

P. B. Sunderland, D. L. Urban, D. P. Stocker, B. H. Chao, and R. L. Axelbaum, "Sooting limits of microgravity spherical difusion flames in oxygen-enriched air and diluted fuel", Combustion Science and Technology, Vol. 176, P. 2143-2164, 2004.

A. Szoke, and E. D. Brooks III, "The transport equation in optically thick media", Journal of Quantitative Spectroscopy & Radiative Transfer, Vol. 91, P. 95-110, 2005.

J. Taine, "A line-by-line calculation of low-resolution radiative properties of CO2-CO-transparent nonisothermal gases mixtures up to 3000 K", Journal of Quantitative Spectroscopy and Radiative Transfer, Vol. 30, No. 4, P. 371-379, 1983.

C. L. Tien, "Thermal radiation properties of gases. In: Advances in heat transfer", Vol. 5, New York: Academic Press, P. 253-324, 1968.

J. S. Truelove, “Discrete-ordinate solutions of the radiation transport equation”, ASME Journal of Heat Transfer, Vol. 109, P. 1048-1051, 1987.

J. R. Tsai, M. N. Ozisik, and F. Santarelli, “Radiation in spherical symmetry with anisotropic scattering and variable properties”, Journal of Quantitative Spectroscopy and Radiative Transfer, Vol. 42, P. 187-199, 1989.

S. D. Tse, D. Zhu, C. J. Sung, Y. Ju, and C. K. Law, “Microgravity burner-generated spherical diffusion flames: experiment and computation”, Combustion and Flame, Vol. 125, P. 1265-1278, 2001.

M. M. Weiner, D. K. Edwards, “Non-isothermal gas radiation in superposed vibration-rotation bands”, Journal of Quantitative Spectroscopy and Radiative Transfer, Vol. 8, P. 1171-1183, 1968.

A. B. White, JR., “On the numerical solution of initial/boundary-value problems in one space dimension”, SIAM Journal on Numerical Analysis, Vol. 19, P. 683-697, 1982.

K. A. Winkler, D. Mihalas, and M. L. Norman, “Adaptive-grid methods with asymmetric time-filtering”, Computer Physics Communications, Vol. 36, P. 121-140, 1985.

M. Wu, P. D. Ronney, R. O. Colantonio, and D. M. VanZandt, “Detailed numerical simulation of flame ball structure and dynamics”, Combustion and Flame, Vol. 116, P. 387-397, 1999.

H. Zhang and M. F. Modest, “Evaluation of the Planck-mean absorption coefficients from HITRAN and HITEMP databases”, Journal of Quantitative Spectroscopy and Radiative Transfer, Vol. 73, P. 649-653, 2002.